

Thèse

**Etude expérimentale du préformage de renforts piqués
pour composites : conception et caractérisations**

**Experimental study of the preforming of tufted reinforcements for
composites: design and characterizations**

Présenté par :

Hao SHEN

Pour obtenir le grade de Docteur de l'Université de Lille

Discipline : Mécanique des solides, des matériaux, des structures et des surfaces

Soutenue le 29/09/2020 devant la commission d'examen

Membres du jury du comité:

M. Joël BREARD	Professeur, Université le Havre	Président/Rapporteur
M. Christophe BINETRUY	Professeur, Centrale Nantes	Rapporteur
M. Philippe BOISSE	Professeur, INSA Lyon	Examineur
Mme. Marie Ange BUENO	Professeur, Université Haute Alsace	Examinatrice
M. Xavier LEGRAND	Professeur, ENSAIT	Directeur
M. Peng WANG	Professeur, Université Haute Alsace	Co-directeur

Cette thèse fait partie du projet: Etude exPérimentale et numérique du thermoformAge de composites thermoplastiques avec des structures textiles COMéelées (PACO)

Ce projet de recherche a été soutenu financièrement par l'ENSAIT/GEMTEX et la **Région Hauts-de-France**

Loratoire d'accueil : GEMTEX

Etablissement d'inscription : USTLille

Durée, début : 01/10/2017, fin :30/09/2020

Acknowledgements

Thanks for the financial supports of the project PACO from the Rigion of Hauts-de-France and GEMTEX in the past three years.

I would like to express my deep and sincere gratitude to my research supervisor, Prof. Xavier LEGRAND and Prof. Peng WANG, for giving me the opportunity to do research and providing invaluable guidance throughout the whole research. Their dynamism, vision, sincerity and motivation have deeply inspired me. They have taught me the methodology to carry out the research and to present the research works as clearly as possible. It was a great privilege and honor to work and study under their guidance. I am extremely grateful for what they have offered me. I would also like to thank them for their friendship, empathy, and great sense of humour.

I am extremely grateful to my parents for their love, caring and sacrifices for my education. I am also very thankful to my girlfriend for her understanding and continuing support to complete my research work.

I also would like to say great thanks to the other professors, Damien SOULAT, François BOUSSU, and to my research colleagues, Shenglei XIAO, Chan HUI, Chen CHEN, Imen GNABA, Fatma OMRANI, Neda SHAH-HOSSEINI, Ezgi ISMAR and so on, for their constant encouragement and company during the last three years.

Finally, my thanks go to all the people who have supported me to complete the research work directly or indirectly.

Contents

Acknowledgements	II
List of figures.....	VI
List of tables	X
General introduction	1
1. State of art and background	4
1.1. Introduction	5
1.2. Composition of fiber-reinforced composite materials	5
1.3. Impregnated strategies for thermoplastic composites	8
1.4. Forming process for thermoplastic composites.....	10
1.5. Forming defects.....	12
1.6. 2D Laminated reinforcements	13
1.7. 3D tufted reinforcements.....	14
1.8. Outline.....	16
1.9. References	17
2. Design of a thermoforming machine	21
2.1 Introduction.....	22
2.2 Important parameters during thermoforming process.....	23
2.2.1 Thermal parameters	23
2.2.2 Pressure parameters	25
2.3 Thermoforming machine	26
2.3.1 Project objectives.....	26
2.3.2 Design overview	27
2.3.3 Structural frame	29
2.3.4 Heating system	30
2.3.5 Transferring system	31

2.3.6	Forming system	33
2.3.7	Assemblage of thermoforming machine.....	34
2.4	Conclusion	35
2.5	Reference	36
3.	Influence of the tufting pattern on the formability of tufted multi-layered preforms	38
3.1.	Introduction	39
3.2.	Methods and materials	40
3.2.1	Tufting process	40
3.2.2	Forming device	41
3.2.3	Materials	43
3.3.	Forming results.....	45
3.3.1	Material draw-in and punch load.....	46
3.3.2	Inter-layer sliding	49
3.3.3	Wrinkling.....	51
3.3.4	Out-of-plane defects	53
3.4.	Discussion	55
3.5.	Conclusion.....	59
3.6.	References	60
4.	Characterisation and optimisation of wrinkling during the forming of tufted three-dimensional composite preforms	62
4.1.	Introduction	63
4.2.	Materials and methods	64
4.2.1	Tufting process and tufted preforms.....	64
4.2.2	Forming process	66
4.2.3	Image-analysis of deformed preforms	66
4.2.4	Wrinkling characterization	68
4.3.	Results and discussion.....	72

4.3.1	Wrinkle patterns	74
4.3.2	Wrinkle ratio	78
4.3.3	Wrinkle-free height and maximum wrinkle amplitude	82
4.3.4	Evaluation of wrinkling	84
4.4.	Conclusion.....	87
4.5.	References	88
5.	Experimental analysis on the in-plane shear properties during the forming of the tufted carbon woven fabrics	89
5.1.	Introduction	90
5.2.	Materials and methods	91
5.2.1	Materials	91
5.2.2	Bias-extension test.....	91
5.2.3	Tufting process and test specimens	94
5.2.4	Optical measurement based on cross-correlation algorithm.....	97
5.3.	Results and discussion.....	99
5.3.1	The deformation mechanisms of the tufting yarns	99
5.3.2	Influence of in-plane tufting directions on shear deformation	105
5.3.3	Influence of tufting density on shear deformation.....	108
5.3.4	Influence of the tufting yarn's fineness on shear deformation	109
5.3.5	Comparison with the tufted two layers preforms	110
5.3.6	Mechanical analysis of tufting effect on shear deformation.....	111
5.4.	Conclusion.....	116
5.5.	Reference.....	117
	General conclusion	121
	Perspective.....	124
	Abstract.....	126
	Résumé	127

List of figures

CHAPTER 1

Figure 1.1 Weight fractions of materials processed in the Airbus A350 XWB[5]	6
Figure 1.2 Specific strength versus specific stiffness trends based on fiber lengths[3].....	7
Figure 1.3 Impregnation of fiber reinforced thermoplastics[11].....	8
Figure 1.4 Illustration of thermoforming process for thermoplastic composites [21]	11
Figure 1.5 Schematic of the thread arrangement in a tufted preform: (a) details the sequential steps of a full insertion, (b) illustrates the option of partial penetration while (c) shows angled insertion [47]	15

CHAPTER 2

Figure 2.1 Key stages in the thermoforming process for reinforced thermoplastic composites, including thermal history[6]	24
Figure 2.2 Influence of the distribution and number of springs [12]	26
Figure 2.3 Flow diagram of main systems (a), 3D model of thermoforming machine (b)	28
Figure 2.4 The structure frame	29
Figure 2.5 Heating system.....	30
Figure 2.6 Transferring system	32
Figure 2.7 The height variation of the material support frame	33
Figure 2.8 Forming system.....	34
Figure 2.9 Photo of thermoforming machine in GEMTEX laboratory	35

CHAPTER 3

Figure 3.1 Tufting device (a) and zoom of tufting head (b).....	41
Figure 3.2 The forming device	42

Figure 3.3 Schematic of forming device: (a) Hemispherical punch (b) Square-box punch.....	42
Figure 3.4 Schematic description of the different tufting patterns.....	43
Figure 3.5 Top of view of the tufted preforms with the different tufting pattern	44
Figure 3.6 Deformed tufted preforms after forming, (a) hemispherical forming using C10/10 sample and (b) square-box forming using C10/30 sample.....	45
Figure 3.7 Influence of tufting pattern and density on the maximum material draw-in in the hemispherical and square-box forming	47
Figure 3.8 Influence of tufting pattern and density on the maximum punch load in the hemispherical and square-box forming	48
Figure 3.9 Influence of tufting pattern and density on the maximum interlayer sliding in the hemispherical and square-box forming	50
Figure 3.10 Wrinkling phenomenon in (a) hemispherical and (b) square-box forming	51
Figure 3.11 Influence of tufting pattern and density on the wrinkling phenomenon in the hemispherical forming.....	52
Figure 3.12 Influence of tufting pattern and density on the wrinkling phenomenon in the square-box forming	53
Figure 3.13 Top view of the deformed preforms with the different tufting pattern.....	54
Figure 3.14 The comparison of two tufting patterns during hemispherical forming	56
Figure 3.15 The comparison of two tufting patterns during square-box forming.....	56
Figure 3.16 The comparison of wrinkling phenomenon between two tufting patterns	57
Figure 3.17 The out-of-plane defects during in the tufted preforms forming	58
CHAPTER 4	
Figure 4.1 Schematic of stacking sequence.	64
Figure 4.2 Example of modelling procedure, (a) photo of sample, (b) raw point-cloud, (c) processed point-cloud.....	68

Figure 4.3 Schematic of modelling, (a) position and feature of ground control point (GCP) used in this test, (b) method of distance measurement between two point clouds [15].	69
Figure 4.4 Example of wrinkle characterization methodology, showing the models from the top view of center in hemispherical forming and from the vertex extension line in square-box forming, the warp and weft directions of the top layer corresponding respectively the X and Y directions, (a) tufted sample model, (b) wrinkle-free sample model, (c) original wrinkle pattern, (d) wrinkle pattern without the tufting yarns, (e) wrinkle pattern after the threshold filtration, (f) binary wrinkle pattern.	71
Figure 4.5 The deformed preforms after the hemispherical forming.	73
Figure 4.6 The deformed preforms after the square-box forming.	74
Figure 4.7 Wrinkle patterns for the different test samples in hemispherical forming.	76
Figure 4.8 Wrinkle patterns for the different test samples in square-box forming.	77
Figure 4.9 Schematic of the measurement position for wrinkle-free height (Δh) and wrinkle amplitude, front section view of hemispherical forming (a), front section view of square-box forming (b), top section view of hemispherical forming (c), top section view of square-box forming(d)	83
Figure 4.10 Influence of tufting location on the measurements of wrinkle-free height and maximum wrinkle amplitude.	84
Figure 4.11 Summary of different wrinkling indicators, (a) hemispherical forming, (b) square-box forming	86
CHAPTER 5	
Figure 5.1 Schematic of bias extension test	Error! Bookmark not defined.
Figure 5.2 Normalized load and shear load on a rhomboid with unit side. ...	Error! Bookmark not defined.

Figure 5.3 Schematic of the H10 tufted specimen (a) and image of the H10 tufted specimen (b).	Error! Bookmark not defined.
Figure 5.4 Un-deformed specimen (a) and deformed specimen (b).	98
Figure 5.5 The two surfaces of a tufted specimen (a) and the influence of fabric deformation on the position of tufting nodes.	101
Figure 5.6 Theoretical/measured tufting space in different directions (a) and theoretical/measured shear angle for a non-tufted specimen (b) in a bias-extension test.	102
Figure 5.7 For vertical tufting, sliding behavior of tufting yarn at different fabric extension stages (a) and the comparison between the mean sliding distance of tufting yarn and the increase of tufting space (b).	103
Figure 5.8 Shear load curves for different tufting directions (a) and the applied force measured at a shear angle 55° (b).	106
Figure 5.9 Schematic of mechanical mechanisms in tufted fabrics.	108
Figure 5.10 Shear load curves for different tufting densities (a) and the applied force measured at a shear angle 55° (b).	109
Figure 5.11 The comparison of overall applied loads between H10D and H10 specimens with a single layer (a) and the applied force measured at a shear angle 55° (b).	110
Figure 5.12 The comparison of overall applied loads between H10D and H10 specimens with two layers (a) and the applied force measured at a shear angle 55° (b).	111
Figure 5.13 Schematic of tufted fabric composed with different elementary units (a); non-tufted elementary unit (b); single-tufted elementary unit (c); double-tufted elementary unit (d); distribution of shear force in elementary unit (e).	112

List of tables

Table 3.1 Main parameters of thermoforming process	43
Table 3.2 Main properties of the test specimens	45
Table 3.3 Main parameters of S20 and C20/15 samples.....	55
Table 4.1 Main properties of the test samples.....	65
Table 4.2 Statistical data of normal distribution.	72
Table 4.3 Binary wrinkle images with different thresholds in hemispherical forming (The threshold values are shown in the first row of the table)	79
Table 4.4 Binary wrinkle images with different thresholds in square-box forming (The threshold values are shown in the first row of the table)	81
Table 5.1 Main properties of the test specimens.....	94
Table 5.2 Deformation behavior of tufting yarn at different fabric extension stages for horizontal and vertical tufting cases.....	103

General introduction

Nowadays, the textile composite materials, as an advanced material, have been widely used in many industrial fields, such as aerospace, aeronautic, automobile and sports. The textile composite materials can replace the traditional metal materials, as they provide the similar strength and stiffness but the weight is much reduced. Considering the properties of the matrix used in the textile composite materials, the two most common manufacturing processes are listed: 1. Liquid Composite Moulding (LCM) is widely used for obtaining the thermoset composites, where the forming process of dry reinforcements is before the impregnation of the matrix; 2. Thermoforming is generally applied in the manufacture of the thermoplastic composites, in which the reinforcements and matrix are mixed closely to each other and synchronously shaped. However, both the manufacturing processes can experience the different defects during the deformation of textile reinforcement or the impregnation of resin or the crystallization process. These defects, such as cracks, resin-rich zone, wrinkling and so on, can considerably degrade the mechanical performances of the final composite parts.

The forming of textile reinforcements is needed in both LCM process for thermoset composites and thermoforming process for thermoplastic composites, in order to obtain the desired shape of composite parts with high automation. However, as the deformation of textile reinforcements is complicated during forming, especially in the case of the double-curved shape forming, several forming defects can be easily introduced due to the inappropriate forming operations or parameters. Wrinkling, buckling and slippage of yarn network are considered to be the most common forming defects. At the same time, these forming defects are almost impossible to be removed in the following process and can be maintained in the final composite part, which is unacceptable. It should try to eliminate these forming defects from the beginning to improve the product quality. Therefore, my research works in the past three years can be briefly divided into three principal aspects:

First, in order to investigate the properties of commingled thermoplastic composites, the conception of an experimental thermoforming machine is carried out with the help of CAD software. A complete 3D prototype is established and tested in a virtual environment to reduce the costs of trial and error. Then, an assemblage of the thermoforming machine based on this design is executed in the GEMTEX laboratory. The thermal and pressure parameters can be adjusted by this machine according to the requirements to study their influences on the formability behaviours of the commingled preregs. The detailed introductions of this experimental thermoforming machine are presented in Chapter 2.

Second, a set of experimental investigations concerning the forming behaviours of the tufted multi-layered reinforcements have been conducted at the dry fabric scale and described in Chapter 3-4. In particular, the influence of tufting density, tufting pattern and tufting position on the formability behaviours or the forming defects is mainly discussed. According to experimental results, an optimization of the tufted multi-layered reinforcements can be achieved. In addition, to better characterize the wrinkling phenomenon emerging on the deformed fabric, a numerical method based on Structure from Motion (SFM) technique is proposed.

Third, in Chapter 5, the influence of tufting on the shear property of woven fabrics has been further investigated through the bias-extension tests. Computer vision is applied to track the moving markers on the surface of fabric for calculating the actual shear angle during the bias-extension test.

1. State of art and background

1.1. Introduction

The word ‘composite’, in terms of composite material, signifies that two or more materials are combined on a macroscopic scale to form a new useful material[1]. These constituent materials normally should have significantly different physical or chemical properties and the characteristics of the final composite part are different from the individual components.

Advanced fiber-reinforced polymer (FRP) composite materials have been widely used in many industries, from sporting goods to aircraft, owing to their lightweight, high strength and perfect structural durability[2]. In this chapter, the current state of art and background of the FRP composite is reviewed.

Firstly, the definition, applications and advantages of FRP composite materials are introduced. According to the subject of this thesis, some specific aspects of thermoplastic composite materials are selected out and described in detail, such as resin impregnated strategies and manufacturing methods.

Secondly, the difference between the two-dimensional (2D) and three-dimensional (3D) fiber reinforced composites is presented briefly. Tufting, as one of the various textile technologies for obtaining 3D composites, is mainly focused, because the academic studies in this thesis are mainly based on this technique.

1.2. Composition of fiber-reinforced composite materials

Fiber-reinforced polymer composites, as one of the most common composite materials, have gained more and more attention. Compared to the traditional metal materials, the FRP composite materials present a large number of advantages, such as high strength-to-weight and stiffness-to-weight ratios, the excellent durability, fatigue resistance, design flexibility,

corrosion resistance and reduced production/maintenance cost[3]. FRP composites were invented at the beginning of 20th century and then obtained an outstanding success in industrial manufacture. Nowadays, these FRP composite materials have been widely applied to various sectors, such as aerospace, aeronautics, sporting products, marine, automotive and transportation. In aeronautical engineering, until the year 2000, the overall weight fraction of FRP composite materials in commercial aircraft has reached 15%[4]. In some special aircraft models, such as Airbus A350 XWB (Figure 1.1), this weight fraction has even passed over 50%[5].



Figure 1.1 Weight fractions of materials processed in the Airbus A350 XWB[5]

FRP is a composite material composed of fiber reinforcement and polymer matrix. The main function of fiber reinforcement is to provide resistance to mechanical stress. On the other hand, the solidified polymer matrix accounts for fixing the position of the inside fibers, so that to maintain stable geometrical characteristics of the product. It also permits loads to be transferred to the reinforcing components by the shear adhesion forces and protects fiber reinforcement from the damage of the external environment[6]. Many high-performance fibers are commonly used as reinforcements for structural thermoplastics, such as E-/S-/R-glass, carbon (AS-4, T-300), aramid (Kevlar-49, Twaron)[7].

On the other hand, based on the type of polymer matrix, FRP composites can be classified as thermoset and thermoplastic. Thermoset polymers, such as epoxy, phenolic, polyester and

vinyl ester resins, are fully cross-linked to form irreversible chemical bonds during the curing process and cannot be melted after consolidation. On the contrary, thermoplastic polymers, such as polyphenylene sulfide (PPS), polyamide (PA), polypropylene (PP) and polyethylene (PE), can be converted back to a viscous liquid in the high temperature. Compared to thermoset composites, the main benefits of thermoplastic composites contains recyclability, enhanced mechanical properties, short production cycle, low toxicity, better corrosion resistance, higher moisture and improved assembly/joining flexibility[3].

Thermoplastic composites can be then further classified as discontinuous fiber (short fiber, long fiber) and continuous fiber composites according to the length of fiber reinforcement. A review[3] in terms of thermoplastic composite materials reveals that continuous fiber presents a higher specific stiffness and strength compared to the discontinuous fiber, as shown in Figure 1.2. Continuous fiber reinforced thermoplastic (CFRTP) composite materials permit to exhibit the full potential of the reinforcement in mechanical properties.

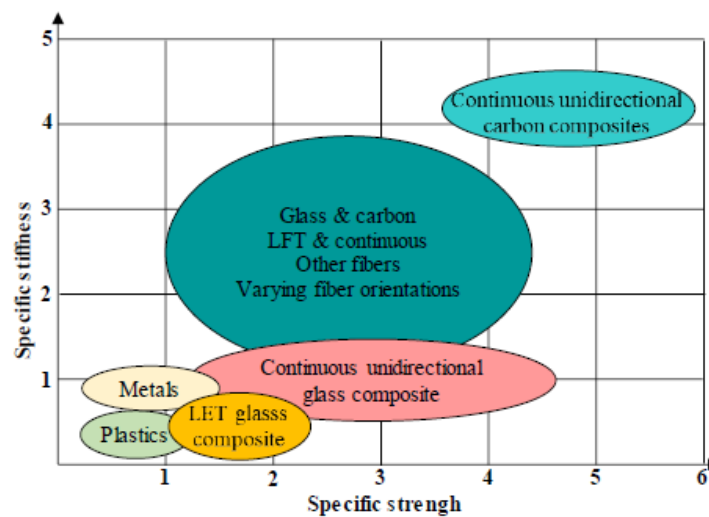


Figure 1.2 Specific strength versus specific stiffness trends based on fiber lengths[3]

1.3. Impregnated strategies for thermoplastic composites

The thermoplastic composites have many advantages, but the most important problem is the requirement for high processing temperature and pressure, owing to the high viscosity of thermoplastic polymers[8]. Inappropriate impregnation methods will lead to poor dispersion of fibers and a poor quality of the final composite part. In other words, only when all individual filaments of the fiber bundle are fully covered with matrix, high-performance characteristics can be presented.

Generally, thermoplastic composites are manufactured based on preregs, which is a semi-finished product used to separate the impregnation step from the forming step[9]. Various concepts of these intermediates have been developed[10] and can be broadly classified into two categories[3], i.e. pre-impregnated form and semi-impregnated form.

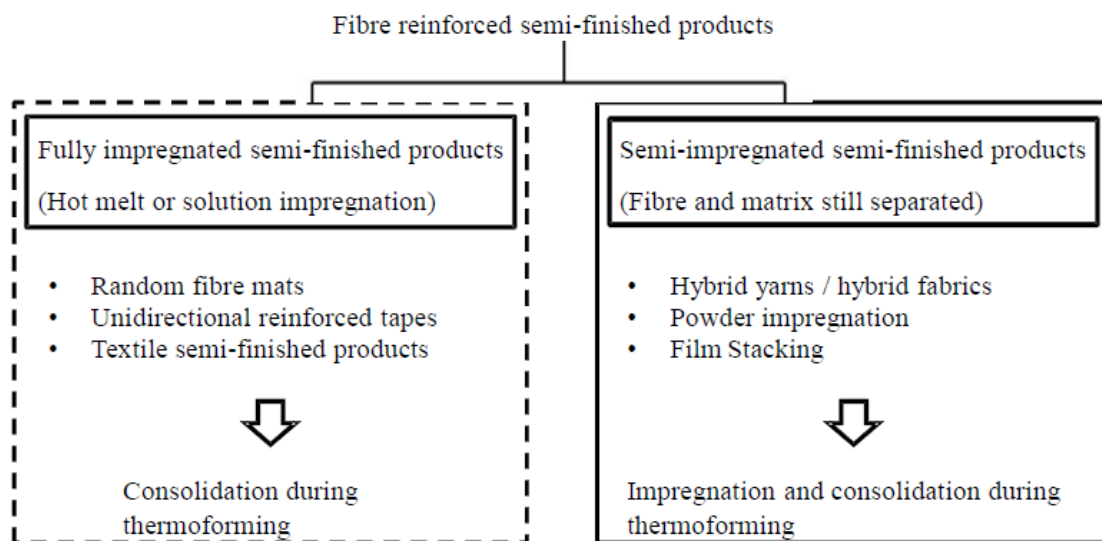


Figure 1.3 Impregnation of fiber reinforced thermoplastics[11]

For the pre-impregnation, the melted or liquid polymers have been infused into the fibers to form the fully impregnated preregs. Only the material's surface is necessary to be melted and consolidated to other layers in the subsequent forming process[12]. For the semi-impregnation, the polymers in the form of film, filament or powder are intermingled closely

with the fiber reinforcement to reduce the required flow length of the polymer matrix. The fibers and matrices in the semi-impregnated preregs are still separated. Figure 1.3 shows the different impregnation approaches for thermoplastic polymers.

However, most impregnation approaches are limited to a dense fiber network, due to the high melt viscosity of thermoplastic polymers. To overcome this problem, the preregs based on commingled yarns are considered to be a good selection to minimize the flow distance for impregnation[3,13]. The fibers of thermoplastic polymers are mixed with reinforcing fibers on the scale of filaments. Commingling yarns are thought to have a homogeneous structure over the yarn cross-section. The fiber to matrix ratio and hybrid yarn fineness can be controlled by adjusting the number or fineness of the constituent filaments[14,15]. Compared to other types of preregs (pre-impregnated forms or powder/film impregnated forms), another advantage of the commingled preregs is their high flexibility of interlacement, which is considered to be a critical requirement for the complex shape processing[3]. Many published literatures have investigated the commingled preregs concerning the yarn manufacturing technique, modelling of impregnation/consolidation process, and mechanical properties of commingled composites[14–16]. At the same time, these studies reveal that various parameters have an influence on the properties of commingled composites including volume fraction of matrix, degree of interlacing, the number of filaments in yarn bundle, filament fineness and so on.

Although most thermoplastic polymers can be submitted to remolding process numerous times, several high-performance of these polymers still can be degraded owing to the cross-linking effect at a high temperature state[17]. Any thermoplastic composite made by preregs needs to undergo melting process, which can generate some cross-links in the matrix and reduce the properties of the final part. An alternative method to the preregs is the reactive process. After impregnating the fibers with a low viscosity mono- or oligomeric precursor, polymerization of the thermoplastic matrix is conducted in situ[8]. Therefore, with the help of

reactive process, textile fiber-reinforced thermoplastic composites can be even manufactured through resin transfer molding (RTM) process[18]. K Van Rijswijk et al. have given a review about the engineering and high-performance thermoplastic polymers suitable for reactive process, and identified the differences between the reactive processing of thermoplastic and thermoset resin[8].

1.4. Forming process for thermoplastic composites

There are a number of methods for manufacturing the thermoplastic composite parts, such as pultrusion, filament winding, automated tow placement, thermoforming and compression molding[3]. Pultrusion and filament winding can provide a larger volume production with low cost, but they are limited to the requirement of product shape. In the automated tow placement, the consolidation of thermoplastic polymers occurs in situ under heat and pressure, in order to avoid costly post-operations, such as autoclave or hot press consolidation[19,20]. However, the speed of tow placement is restricted by the consolidation of thermoplastic polymers. Compression molding and thermoforming process can be used to produce large size plastic components in a short time and form complex or undevelopable shapes more easily. These two methods are similar with some critical steps, which can be divided briefly into preheating, transferring, stamping/consolidation and demolding process. The principle difference between compression molding and thermoforming is the requirement of trimming process[3]. For the compression molding, the prepregs are placed in a sealed mold to produce a part with essentially no final trimming required. On the contrary, for thermoforming, the edges of prepregs may be pushed out from the useful zone and needed to be cut off after demolding. A non-completely sealed forming condition permits to use low molding pressures (<0.35 Mpa) to produce large size parts.

For thermoforming process, as illustrated in Figure 1.4, generally, a blank is cut from a pre-consolidated laminate with a stack of textile fiber reinforced plies. The blank is held by a gripping frame and placed into a heating device, such as an infra-red oven, to melt the matrix. After achieving a sufficiently high temperature above the polymer melting point, the viscous blank is transported to the stamping tool, which normally includes a positive male and a negative female mold. Various configurations of the stamping tool are used in practice, such as matched-metal and rubber-metal[21]. The blank is deformed after the closure of tooling and constant pressure is applied during the whole consolidation process. At least one of the molds is needed to be preheated to control this cooling process. When the deformed blank is completely solidified, the forming tools reopen to demold the composite part. Finally, a trimming operation is carried out to remove the excess materials. Through the thermoforming process, not only simple geometric parts with single curvature, such as clips and brackets[22], but also some complex parts with double-curved shape, such as stringers and ribs, can be produced.

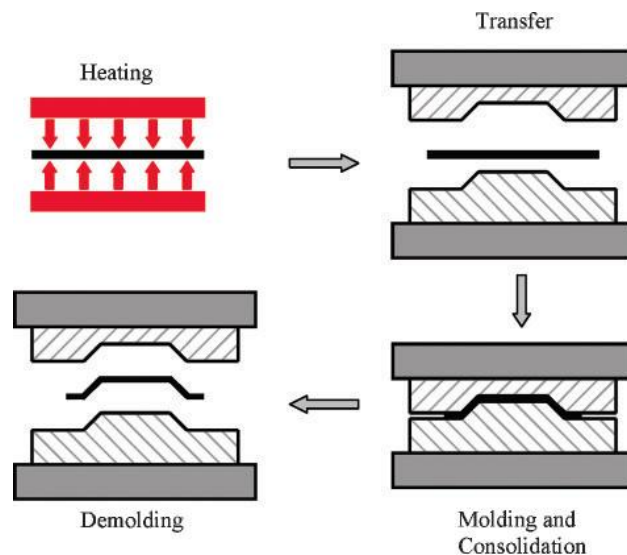


Figure 1.4 Illustration of thermoforming process for thermoplastic composites [21]

1.5. Forming defects

The textile reinforced composite structures can be manufactured by forming process from an initial flat fabric to a complex shape efficiently. Most common composite materials, such as glass, carbon and aramid, are hard to be elongated in tow longitude direction. Therefore, in order to adapt to the required forming shape, angular variations between the constitutive yarns cannot be avoided during the fabric deformation. The undulation variation of these fabric yarns will probably cause unexpected forming defects, such as misalignment, gap, sliding of yarn network, wrinkling, buckling and so on[23–26], which can bring many negative impacts on the performance of final composite parts. The generation of forming defects is complicated and considered to be related to the fabric properties (materials, density, interlacing patterns...), reinforcement structures (lay-up orientation, stacking sequence...), resin properties (viscosity, melting temperature...) and processing parameters (forming pressure, speed, tool temperature...).

A large number of studies have been done to develop basic knowledge in forming defects. Hallander et al. [27] evaluated the effect of lay-up sequence, in-plane pre-tension, layer thickness on the appearance of wrinkles in the forming of a quasi-isotropic laminate composed of unidirectional (UD) layers. Hou et al. [28] have illustrated that the forming pressure applied to the material during molding can significantly increase the wall thickness distribution of the composite part. De Luca et al. [29] observed the inherent difference between the deformation behavior of woven and UD composites during forming. McCool et al. [30] have done an extensive study to identify some of the key parameters of the thermoforming process as well as their influences on some properties of the woven composite part. Chen et al. [31] have investigated the crystallization kinetics of CF/PEEK composites at 61% fiber volume content, through both the isothermal and the non-isothermal crystallization

approaches. As a result, it is important to characterize the level of various forming defects, so as to optimize the design and manufacturing process of composite parts.

1.6. 2D Laminated reinforcements

In the fiber-reinforced composite materials, fiber reinforcements have a significant effect on the final mechanical properties of composite part. In order to obtain different forms of fiber reinforcements meeting the requirements of composite manufacturing, several conventional textile technologies, such as weaving, knitting, braiding and stitching, have been widely applied to produce fiber-reinforcements.

Based on the alignment direction of the constitutive fiber bundles, the fiber reinforcement can be classified into three groups[2]: unidirectional (1D/UD) fiber reinforcement where all the fibers are aligned in the same direction; two-directional (2D) fiber reinforcement where the fibers are aligned on the XY plane; three-directional (3D) fiber reinforcement where a set of fibers are added along the orthogonal axis (Z axis) corresponding to through-thickness axis of the structure[32].

In the industrial manufacture, the 2D laminated fiber reinforced composites have been used successfully over 60 years in aerospace, aeronautic, marine and automobiles[33]. For a 2D laminated structure, the fiber reinforcement is generally achieved by stacking various plies in specific sequence or orientation. Each constitutive fabric ply in 2D laminated composites can be the UD fiber reinforcement possessing only one reinforcing direction or conventional interlaced reinforcement such as woven or braided fabrics owning two or more than two fiber alignment directions in the plane. The orientation of each layer is distinguished by the longitudinal axis of the fibers in the case of unidirectional fabric. For the 2D woven fabric, it refers to the orientation of the longitudinal axis of warp yarns[2]. According to lay-up

stacking sequence, the final 2D laminated composite can be classified as quasi-isotropic laminates where the reinforcing directions are symmetric in the structure, and anisotropic laminates where the reinforcing fibers are only aligned along the load-bearing directions. Although 2D laminates have been used in many products, there are still some restrictions for the application of 2D laminated composites in the critical areas, where high inter-laminar shear stresses are needed to be subjected[33,34]. It reveals that 2D laminated composites have a poor delamination resistance and impact damage tolerance, due to the lack of reinforcement through-thickness.

1.7. 3D tufted reinforcements

In order to improve the mechanical properties through-thickness of composite parts, the conventional 2D laminated composites should be reinforced in Z-axis direction, which is perpendicular to X/Y plane. In an attempt to achieve this purpose, several textile techniques have been developed to manufacture 3D composites, such as 3D weaving[35–38], stitching[39–41], z-pinning[42–44] and tufting[2,45,46]. Tufting techniques, as a relatively novel approach, recently have become commercially available for obtaining the through-thickness reinforcement (TTR).

In a tufting process shown in Figure 1.5a [47], a hollow needle accounts for carrying the additional tufting yarn to penetrate the laminated fabric through-the-thickness. When the needle retracts from the fabric, the embedded tufting yarn will still be maintained in the fabric due to the fictional effect caused by the fabric itself and the underlying support (generally these supports could be plastic/silicone foam or wooden board). At the same time, the tufting yarn can form a free loop on the opposite side of fabric at each tufting node. Only one side of the fabric is necessary to be accessed for accomplishing the tufting process, increasing the flexibility in practical use. Moreover, full insertion and partial insertion method can be

selected according to the different requirements (Figure 1.5b). Full insertion can present total potential in the improvement of mechanical properties through-thickness but the partial insertion can conceal the loops to avoid the creation of resin pocket on the reverse side. The embedding angle of the tufting needle also can be adjusted from orthogonal to angled, relative to the fabric surface, as illustrated in Figure 1.5c. A good selection of tufting yarn, tufting needle, material of support and tufting speed is so important and can much reduce the risk of yarn breakage.

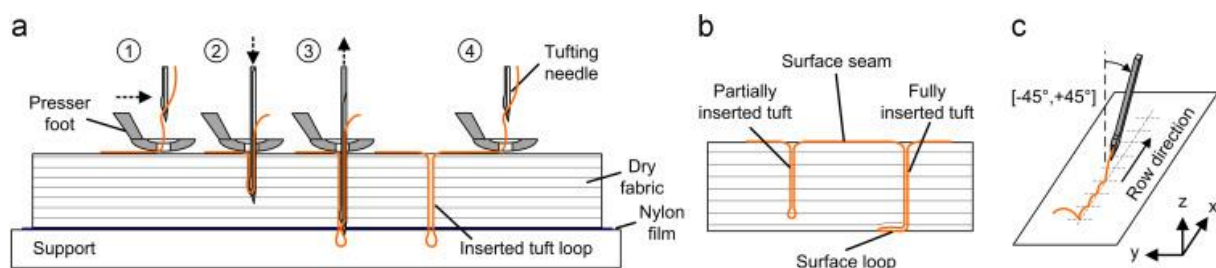


Figure 1.5 Schematic of the thread arrangement in a tufted preform: (a) details the sequential steps of a full insertion, (b) illustrates the option of partial penetration while (c) shows angled insertion [47]

Different from the traditional duel-thread stitching technique, tufting only needs a single-thread operation with tension-free system leading to a low damage to the fabric[48–50]. Some studies have demonstrated that the tufting process can significantly enhance the mechanical properties through-thickness, such as compression after impact strength and delamination resistance. On the contrary, the in-plane mechanical properties, such as tensile and compressive strength can be reduced to some extent owing to the insertion of tufting yarns.

Tufting technique not only can be applied on the multilayered reinforcement, but also can be applied on the sandwich composite structures with different cores. Due to the tufting yarns, the external layer and the core can be bound more closely. This truss-like structure among layers can improve mechanical performance in the final part[48,51]. Tufting technique has been used in some practical applications, such as the patented products of NidaCore® (France) and Acrosoma® (Belgium).

1.8. Outline

The use of fiber reinforced polymer composites is growing rapidly. Thermoplastic-matrix composites provide a number of advantages compared to thermoset-matrix composites, including recyclability, higher fracture toughness, short production cycle, low toxicity, more convenient storage, and improved assembly/joining flexibility. However, the high viscosities of molten thermoplastic polymers bring a serious restriction in actual production. Bad dispersion of fibers and low quality of impregnation may be caused. Therefore, intermediate materials, also called prepregs, are used to reduce the flow distance of thermoplastic polymers. The thermoplastic polymer can be mixed with fiber reinforcement in different forms, such as film stacking, powder-impregnated fiber bundles, and commingled yarns. Commingled yarns are thought to have the most homogeneous distribution of matrix and the closest contact to the fiber bundles, in comparison to others.

In order to investigate the formability behaviors of a thermoplastic composite made by commingled yarns, one main purpose of this thesis is to design and assemble an experimental thermoforming machine. Chapter 2 gives a detailed description of the conception and functionality of this experimental thermoforming machine developed in GEMTEX laboratory. The machine permits to preheat the thermoplastic materials over a melting temperature, transfer the viscous materials from the oven to the forming tool automatically and accomplish the forming process with predefined pressures.

At the same time, because the manufacture of the thermoforming machine consumes a large amount of time and the tests in terms of the thermoplastic composites cannot be executed without the thermoforming machine, some investigations mainly concerning the formability behaviors and forming defects of tufted fabrics have been done to improve the understanding of forming process and tufting technique.

In Chapter 3, based on the study of Liu[46], the influence of the tufting density on the formability of multi-layered preforms has been further investigated. Especially the consistency between the tufting pattern and punch shape are discussed.

In Chapter 4, a new method based on the image analysis methodology is proposed to characterize the wrinkling phenomenon during the forming of tufted composite preforms. Wrinkles are identified as the deviation of the wrinkled shape from a reference shape. Several indicators are used to give a global description of wrinkling severity.

In Chapter 5, the influence of tufting yarns on the shear properties of a carbon woven fabric has been studied. Depending on the optical measurement, the in-plane shear characterization via the bias-extension test is carried out to estimate the effects of tufting direction, tufting density and tufting yarn fineness.

1.9. References

- [1] Jones RM. Mechanics of composite materials. CRC press; 1998.
- [2] Liu L. Development and optimization of the tufting process for textile composite reinforcement 2017.
- [3] Vaidya UK, Chawla KK. Processing of fibre reinforced thermoplastic composites. *Int Mater Rev* 2008;53:185–218.
- [4] Reinhart G, Ehinger C. Novel robot-based end-effector design for an automated preforming of limb carbon fiber textiles. *Futur. trends Prod. Eng.*, Springer; 2013, p. 131–42.
- [5] Marsh G. Airbus A350 XWB update. *Reinf Plast* 2010;54:20–4.
- [6] Peters ST. Handbook of composites. Springer Science & Business Media; 2013.
- [7] Chawla KK. Composite materials: science and engineering. Springer Science & Business Media; 2012.
- [8] Van Rijswijk K, Bersee HEN. Reactive processing of textile fiber-reinforced thermoplastic composites—An overview. *Compos Part A Appl Sci Manuf* 2007;38:666–81.

- [9] Flemming M, Ziegmann G, Roth S. Bauweisen. Faserverbundbauweisen, Springer; 1996, p. 197–294.
- [10] Talreja R. Polymer matrix composites. Elsevier; 2001.
- [11] Henninger FH. Beitrag zur Entwicklung neuartiger Fertigungsverfahren zur Herstellung von Bauteilen aus kontinuierlich faserverstärkten Thermoplasten 2005.
- [12] Köhler T, Röding T, Gries T, Seide G. An Overview of Impregnation Methods for Carbon Fibre Reinforced Thermoplastics. Key Eng. Mater., vol. 742, Trans Tech Publ; 2017, p. 473–81.
- [13] Svensson N, Shishoo R, Gilchrist M. Manufacturing of thermoplastic composites from commingled yarns-A review. J Thermoplast Compos Mater 1998;11:22–56.
- [14] Choi BD, Diestel O, Offermann P, Hübner T, Mäder E. Advancement for Commingling Hybrid Yarns for Fiber Reinforced Thermoplastics. Textil-Symposium, April, 2001, p. 23–6.
- [15] Wakeman MD, Zingraff L, Bourban P-E, Månson J-A, Blanchard P. Stamp forming of carbon fibre/PA12 composites–A comparison of a reactive impregnation process and a commingled yarn system. Compos Sci Technol 2006;66:19–35.
- [16] Zhu B, Yu TX, Zhang H, Tao XM. Experimental investigation of formability of commingled woven composite preform in stamping operation. Compos Part B Eng 2011;42:289–95.
- [17] Bulakh N, Jog JP, Nadkarni VM. Structure development in curing of poly (phenylene sulfide). J Macromol Sci Part B Phys 1993;32:275–93.
- [18] Rudd CD. Resin transfer molding and structural reaction injection molding. ASM Handb Vol 21 Compos 2001.
- [19] Ahrens M, Mallick V, Parfrey K. Robotic based thermoplastic fibre placement process. Proceedings. 1998 IEEE Int. Conf. Robot. Autom. (Cat. No. 98CH36146), vol. 2, IEEE; 1998, p. 1148–53.
- [20] Heider D, Piovoso MJ, Gillespie Jr JW. Application of a neural network to improve an automated thermoplastic tow-placement process. J Process Control 2002;12:101–11.
- [21] Haanappel SP. Forming of UD fibre reinforced thermoplastics. University of Twente; 2013.
- [22] Deterts A, Miaris A, Soehner G. Serial production of thermoplastic CFRP parts for the Airbus A350 XWB. Int. Conf. Exhib. Thermoplast. Compos., 2012, p. 60–3.
- [23] Potter K, Khan B, Wisnom M, Bell T, Stevens J. Variability, fibre waviness and misalignment in the determination of the properties of composite materials and structures. Compos Part A Appl Sci Manuf 2008;39:1343–54.
- [24] Boisse P, Hamila N, Vidal-Sallé E, Dumont F. Simulation of wrinkling during textile composite reinforcement forming. Influence of tensile, in-plane shear and bending

- stiffnesses. *Compos Sci Technol* 2011;71:683–92.
- [25] Capelle E, Ouagne P, Soulat D, Duriatti D. Complex shape forming of flax woven fabrics: Design of specific blank-holder shapes to prevent defects. *Compos Part B Eng* 2014;62:29–36.
- [26] Schug A, Winkelbauer J, Hinterhölzl R, Drechsler K. Thermoforming of glass fibre reinforced polypropylene: A study on the influence of different process parameters. *AIP Conf Proc* 2017;1896. doi:10.1063/1.5007997.
- [27] Hallander P, Akermo M, Mattei C, Petersson M, Nyman T. An experimental study of mechanisms behind wrinkle development during forming of composite laminates. *Compos Part A Appl Sci Manuf* 2013;50:54–64.
- [28] Hou M. *Stam Forming of Continuous Glass Fibre Reinforced Polypropylene* 1997;28A:695–702.
- [29] de Luca P, Lefébure P, Pickett AK. Numerical and experimental investigation of some press forming parameters of two fibre reinforced thermoplastics: APC2-AS4 and PEI-CETEX. *Compos Part A Appl Sci Manuf* 1998;29:101–10. doi:10.1016/S1359-835X(97)00060-2.
- [30] McCool R, Murphy A, Wilson R, Jiang Z, Price M, Butterfield J, et al. Thermoforming carbon fibre-reinforced thermoplastic composites. *Proc Inst Mech Eng Part L J Mater Des Appl* 2012;226:91–102. doi:10.1177/1464420712437318.
- [31] Chen M, Chung C. Crystallinity of isothermally and nonisothermally crystallized poly(ether ether ketone) composites. *Polym Compos* 1998;19:689–97.
- [32] Labanieh AR, Legrand X, Koncar V, Soulat D. Development of the 3D multiaxis weaving technology and geometrical characterization of the produced performs n.d.
- [33] Mouritz AP, Bannister MK, Falzon PJ, Leong KH. Review of applications for advanced three-dimensional fibre textile composites. *Compos Part A Appl Sci Manuf* 1999;30:1445–61.
- [34] Mouritz AP. Tensile fatigue properties of 3D composites with through-thickness reinforcement. *Compos Sci Technol* 2008;68:2503–10.
- [35] Ansar M, Xinwei W, Chouwei Z. Modeling strategies of 3D woven composites: a review. *Compos Struct* 2011;93:1947–63.
- [36] De Luycker E, Morestin F, Boisse P, Marsal D. Simulation of 3D interlock composite preforming. *Compos Struct* 2009;88:615–23.
- [37] Dufour C, Wang P, Boussu F, Soulat D. Experimental Investigation About Stamping Behaviour of 3D Warp Interlock Composite Preforms. *Appl Compos Mater* 2014;21:725–38. doi:10.1007/s10443-013-9369-9.
- [38] Baucom JN and, Zikry MA. Low-velocity impact damage progression in woven E-glass composite systems. *Compos Part A Appl Sci Manuf* 2005;36:658–64.

- [39] Dransfield K, Baillie C, Mai Y-W. Improving the delamination resistance of CFRP by stitching—a review. *Compos Sci Technol* 1994;50:305–17.
- [40] Dransfield K, Baillie C, Mai Y-W. On stitching as a method for improving the delamination resistance of CFRPs. Minerals, Metals and Materials Society, Warrendale, PA (United States); 1993.
- [41] Bannister M, Herszberg I. Research activities in textile preforms at the Cooperative Research Centre for Aerospace Structures. *Int. Aerosp. Congr. 1995 Proceedings; Second Pacific Int. Conf. Aerosp. Technol. Sixth Aust. Aeronaut. Conf.*, Institution of Engineers, Australia; 1995, p. 619.
- [42] Mouritz AP. Review of z-pinned composite laminates. *Compos Part A Appl Sci Manuf* 2007;38:2383–97.
- [43] Partridge IK, Cartié DDR. Delamination resistant laminates by Z-Fiber® pinning: Part I manufacture and fracture performance. *Compos Part A Appl Sci Manuf* 2005;36:55–64.
- [44] Freitas G, Fusco T, Campbell T, Harris J, Rosenberg S. Z-fiber technology and products for enhancing composite design. *AGARD Conf. Proc. AGARD CP*, 1997, p. 17.
- [45] Shen H, Wang P, Legrand X, Liu L, Soulat D. Influence of the tufting pattern on the formability of tufted multi-layered preforms. *Compos Struct* 2019;228:111356.
- [46] Liu LS, Zhang T, Wang P, Legrand X, Soulat D. Influence of the tufting yarns on formability of tufted 3-Dimensional composite reinforcement. *Compos Part A Appl Sci Manuf* 2015;78:403–11. doi:10.1016/j.compositesa.2015.07.014.
- [47] Dell’Anno G, Treiber JWG, Partridge IK. Manufacturing of composite parts reinforced through-thickness by tufting. *Robot Comput Integr Manuf* 2016;37:262–72.
- [48] Henao A, Carrera M, Miravete A, Castejón L. Mechanical performance of through-thickness tufted sandwich structures. *Compos Struct* 2010;92:2052–9. doi:10.1016/j.compstruct.2009.11.005.
- [49] Sickinger C, Herrmann A. Structural stitching as a method to design high-performance composites in future. *Proc. TechTextil Symp.*, vol. 2001, 2001.
- [50] Pérès P, Desmars B, Léard JP. Composite behavior of assemblies with AEROTISS® 03S technology. 16th Int. Conf. Compos. Mater., 2007.
- [51] Potluri P and, Kusak E, Reddy TY. Novel stitch-bonded sandwich composite structures. *Compos Struct* 2003;59:251–9.

2. Design of a thermoforming machine

2.1 Introduction

Fibre reinforced polymer composite (FRP) materials have been widely used in aerospace and automotive industries, sports products and medical equipment owing to their low density but high stiffness and strength[1]. According to the type of polymer matrix, the thermoplastic composites generally present higher toughness and better damage resistance compared to the thermoset composites. Moreover, different from the cross-linkable thermoset polymers, which have chemical polymerization reactions in the consolidation stage, the manufacturing of thermoplastic composite significantly reduces the processing time due to the lack of chemistry. Therefore, the thermoplastic composite is only submitted to a simple physical process including heat transfer and shaping, leading to a potential for mass production. The thermoforming technique[2-5], which is developed from the traditional sheet-metal forming technology, provides an automated and fast option for mass production of the continuous fibre reinforced thermoplastic composites (CFRTP) with high performance properties and complex geometry.

In order to carry out the investigations concerning the thermoforming process of CFRTPs, experimental thermoforming equipment has been designed using the Solidworks® software and manufactured in GEMTEX laboratory. This equipment can be divided briefly into three relatively individual systems: heating system, transferring system and punch/open-die forming system. The heating system is an industrial oven used for heating the thermoplastic materials over their melting temperature. Then, the transferring system permits to move the melted prepregs from the oven to the forming system automatically. In the end, the open-die forming system containing a punch and correspondent hollow blank-holders can accomplish a rapid forming process under the control of several pneumatic cylinders with pre-defined pressure. With this equipment, many thermoforming parameters such as pre-heating

temperature, pre-heating time, blank-holder pressure, punch pressure and consolidation time can be adjusted according to the requirement.

2.2 Important parameters during thermoforming process

In the industrial thermoforming process, a rapid transformation from the blank into the required designed shape is implemented by the combination of heat and pressure effects. Both the physical shape change and thermal history of the blank during the complete process are necessary to be focused.

2.2.1 Thermal parameters

As shown in Figure 2.1[6], it can be seen that the first stage is to preheat the consolidated laminates containing the thermoplastic polymers to a temperature over the melting temperature. The thermoplastic matrix in the laminated materials is melted in the heating phase, leading to a release of the stored elastic energy due to residual stress[7]. In the melt phase, the melted thermoplastic polymers permit the intra-ply and inter-ply slippage occurs in the laminated structures. The sliding between each individual ply becomes the dominant mode of deformation[4]. Therefore, the determination of processing temperature is significantly important, as in-sufficient melting of the thermoplastic matrix can provoke considerable matrix cracking, fibre buckling, fibre misalignment and wrinkling in some sharp areas of complex geometries during forming process. Thermoplastic matrix is also sensitive to temperature history, which can affect the induced residual stress, crystallinity and mechanical performance of the final part[6]. Furthermore, when the thermoplastic matrix is heated above the melting temperature, chemical reactions (cross-linking of molecular chains) can occur to some extent, which also can degrade the in-service performance and repeatability.

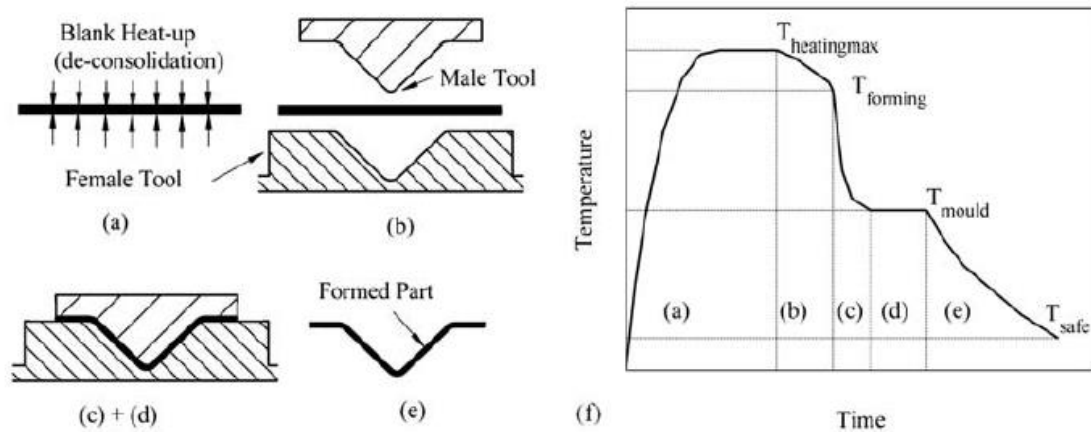


Figure 2.1 Key stages in the thermoforming process for reinforced thermoplastic composites, including thermal history[6]

In the second stage, the blank material is transferred to the forming station (Figure 2.1) with a pre-defined temperature, normally just above the forming temperature considering the thermal heat losses during transmission[6]. The closure of the matched moulds makes the blank material formed to the target shape. These moulds have two main functions: first is to give the materials the final shape, thickness and surface finish; second is to control the cooling process by adjusting the pre-defined mould temperature. The composite part will be extracted from the mould only after its full consolidation. The thickness of the final composite part is affected by several factors such as mould tool geometry, fabric structure, matrix chemical reactions, forming pressure and shrinkage.

In addition, another important processing parameter is the cooling rate after forming, which can be affected by the blank temperature, mould tool temperature, transferring time and press closure time, as the cooling rate is capable to influence the matrix crystallinity and residual stress[8]. For semi-crystalline thermoplastics, a higher cooling rate can lead to a lower peak crystallization temperature and lower crystallinity levels and less matrix shrinkage[8]. The levels of chemical resistance and static strength mechanical properties can be enhanced by a high level of crystallinity, but at the same time the matrix fracture toughness

properties are reduced. On the other hand, the cooling rate also influences significantly the production cycle time of the entire process, because the final parts can be only extracted from the mould when they are completely consolidated and can be handled safely. As a result, the preheating temperature, mould tool temperature and cooling rate should be well considered to optimize the matrix crystallinity and the production cycle time.

2.2.2 Pressure parameters

The critical step of the forming phase is to give a specific normal pressure on the edges of pre-heated laminate panel by the blank-holders[9,10] and to allow the moulds to be closed with sufficiently high pressure. As the 3D forming process leads to a reduced surface area of the laminate and the continuous fibres cannot be lengthened or shortened, the principal mode of deformation is compression[10]. Therefore, this compressive force generated during forming results in a prominent wrinkling phenomenon on the deformed laminate. The principal effects of blank-holder are to give a frictional force to oppose the flow of laminate into the cavity and also to provide stretching and shearing forces, leading to the shear deformation in the plane of fabric. Hou[10] has investigated the effect of blank-holder pressure on the thermoplastic composite part shape and observed that the high pressure can minimize the wrinkling in the flange area. However, this study also demonstrated that the excessive pressure can damage the border between the formed cap and the flat flange. As a result, the pressure of blank-holder should be as high as possible in a limited range during the forming process.

In addition, in the forming process, it is difficult to understand clearly the tribology of molten thermoplastic composite material, as the sliding behaviour contains both static and dynamic frictions depending on temperature, rate and pressure factors[11]. Therefore, the accurate modelling based on the frictional condition of the blank-holder is hard to be achieved.

An alternative way to the blank-holder system is to apply tension by springs and clips on the material, so that the complexity of the friction condition can be avoided. Schug et al.[12] have investigated the influence of the distribution and number of springs, as shown in Figure 2.2. The experimental results illustrated that fewer springs can provoke more wrinkles, worse surface roughness and sag of the specimen.

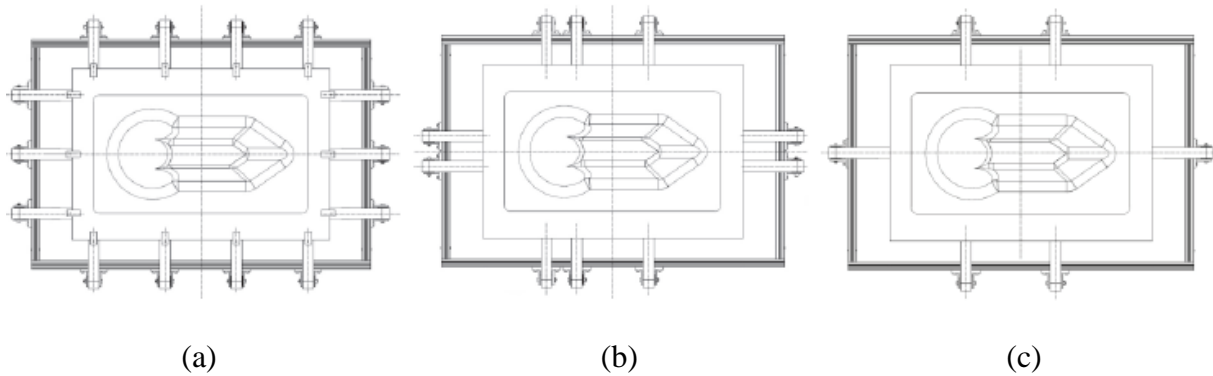


Figure 2.2 Influence of the distribution and number of springs [12]

In a word, the forming pressure provided by either the blank-holder system or springs system can strongly influence the forming behaviour of the composite part. Appropriate tensioning pressure is necessary to be applied to eliminate the wrinkles and increase the final part quality.

2.3 Thermoforming machine

2.3.1 Project objectives

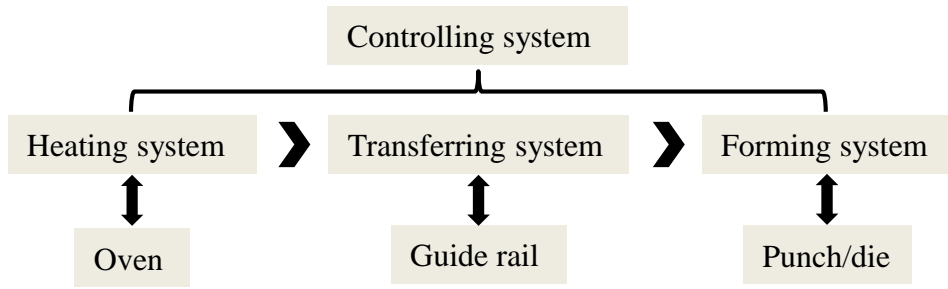
In this section, a detailed introduction concerning the functions and components of the thermoforming machine developed by GEMTEX is demonstrated. With the help of the CAD software ‘Solidworks’, the dimensions and structures of each constitutive part can be accurately pre-estimated by establishing the 3D models in the compute, resulting in a significant reduce in the cost of trial and error. Considering the fundamental thermal and

pressure parameters in the common researches of thermoforming process and the safety of operations, the developed equipment is necessary to follow the following principles:

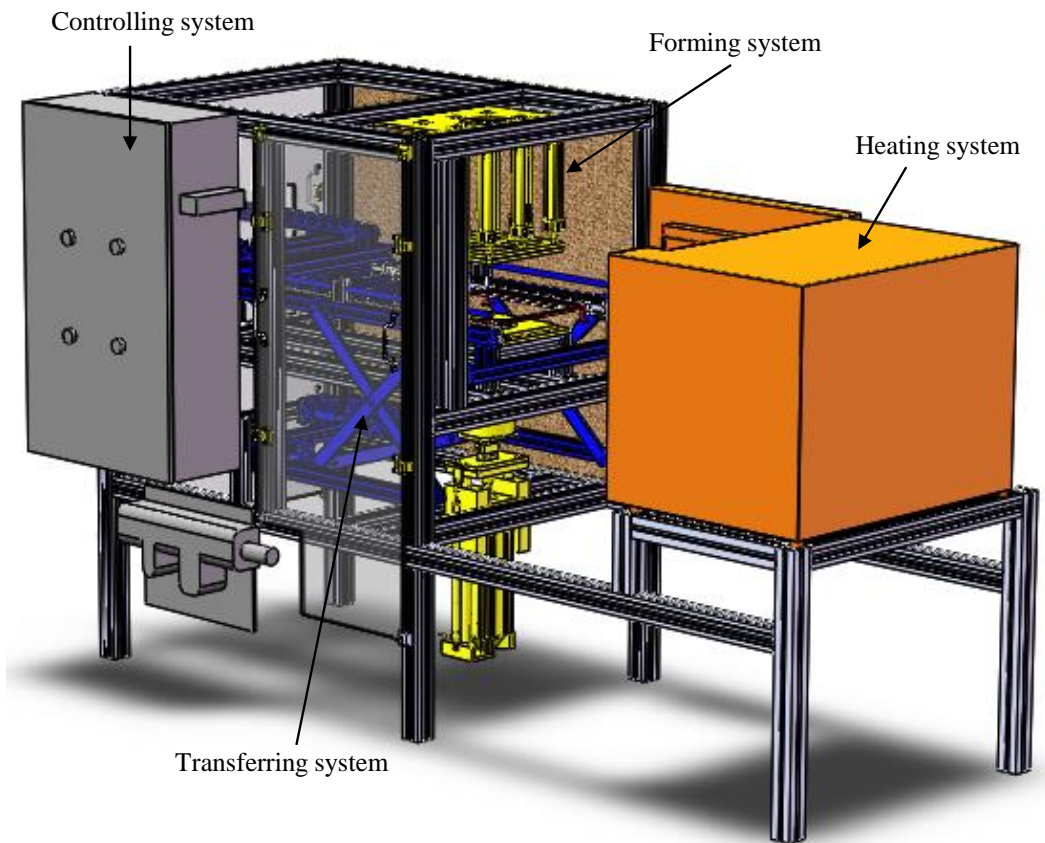
- ❖ An adjustable preheating temperature
- ❖ An adjustable blank-holder and punch pressure
- ❖ An automated transferring system to ensure the melted thermoplastic material can be moved from the heating system to the forming system safely and rapidly
- ❖ A simple operation system
- ❖ A relatively low manufacturing cost
- ❖ A relatively open but safe forming system to increase the observability during the process

2.3.2 Design overview

The overall schematic diagram of the thermoforming machine is illustrated in Figure.2.3. This experimental device can be briefly divided into four main systems, i.e. heating system, transferring system, forming system and controlling system. Figure.2.3a demonstrates their relationship by a flow chart, in which the materials will be processed in a determined order. At the same time, these systems are also indicated in 3D model shown in Figure.2.3b and distinguished by different colours to understand their actual structure and positions. A good cooperation between these systems permits to accomplish the entire thermoforming process successfully. This experimental thermoforming machine is driven by a set of pneumatic devices supported by SMC ® Company. In the following sections, several important parts are selected out and demonstrated in detail.



(a)



(b)

Figure 2.3 Flow diagram of main systems (a), 3D model of thermoforming machine (b)

2.3.3 Structural frame

The proposed thermoforming machine consists of a basic metal support structure on which the other modular systems are mounted, as illustrated in Figure 2.4. This frame structure was designed not only to accommodate all the modular systems, but also to leave sufficient space for the operations of the device. Commercial hollow structural sections (HSS), a type of aluminium profile with a hollow cross-section, are used to construct this structural frame, as the assemblage of these profiles is rapid, flexible and stable. According to the load requirements in different zones, the constitutive profiles have a cross-sectional dimension of either 40×40 mm or 60×60 mm. The dimensions of the entire structural frame are 2620 mm in length, 1650 mm in height and 970 mm in width. In order to guarantee the stability of the overall equipment, a centre-symmetrical structure is adopted in the machine design.

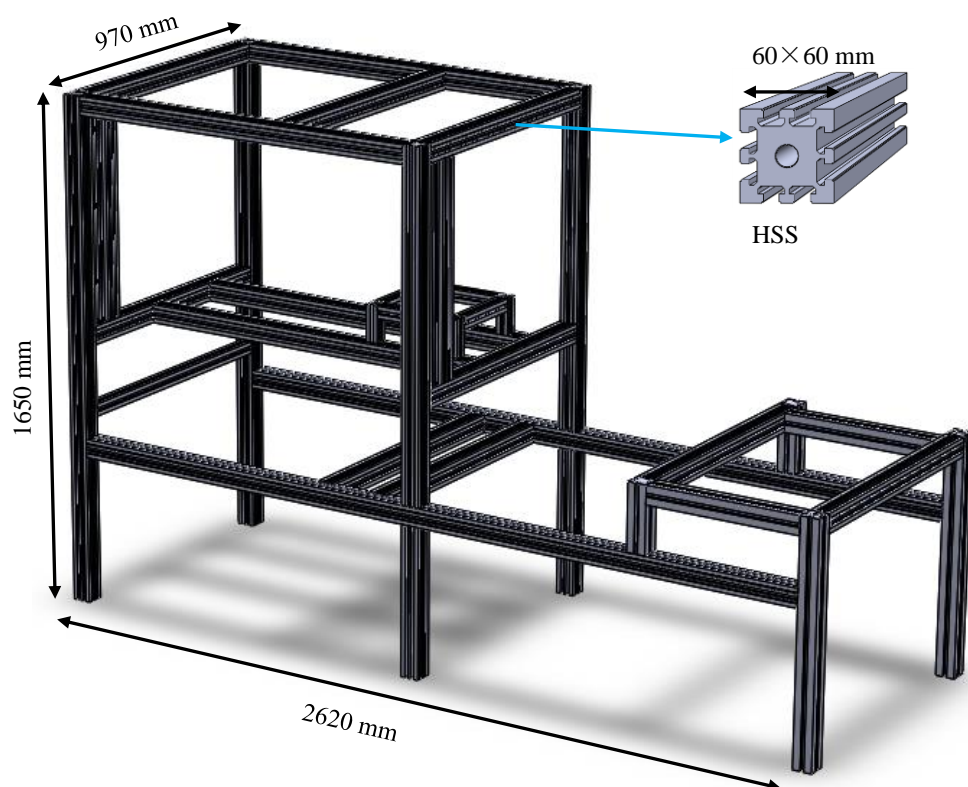


Figure 2.4 The structure frame

2.3.4 Heating system

In Figure.2.5, an industrial oven with a dimension of 850×650×650 mm is placed at one end of the frame accounting for the preheating process. When the oven is turned on, the inside confined space permits the uniform heating on the materials leading to a complete melt of the thermoplastic polymers. The oven temperature can be predefined easily on the screen, in order to meet the various experimental requirements. As the heating temperature is a significant parameter in the investigation of thermoforming process, which even can influence the quality of the final composite part, the heating accuracy of the oven cannot be neglected. Thanks to a monitoring system, the actual oven temperature is tracked and displayed during the whole heating process. Considering the length of the oven door (700 mm), a sufficient distance between the oven and the forming device is necessary to be left.

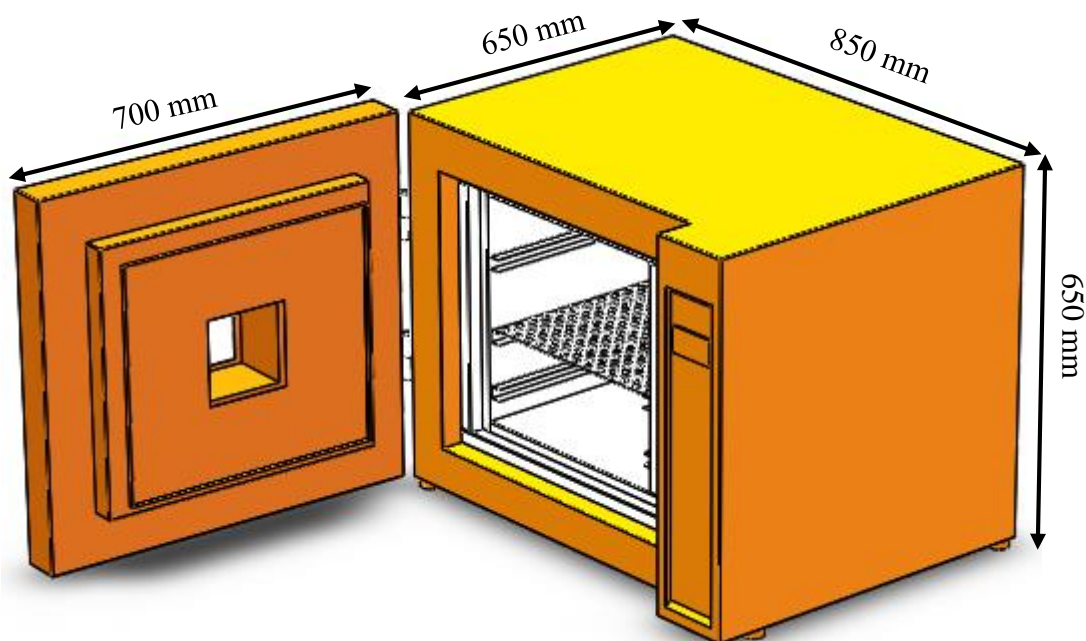


Figure 2.5 Heating system

2.3.5 Transferring system

After being well heated, the melted thermoplastic composite material is needed to be transferred from the oven to the forming tool for the subsequent procedure. However, once the heated composite material leaves the oven cave, the temperature drops rapidly owing to the convection of the cold air. Therefore, not only the composite material should be heated above the melting temperature to compensate the energy loss, but also a fast transferring system is necessary to reduce the energy loss. At the same time, this transferring system also needs to guarantee a precise positioning during the entire process, so that the composite material can be placed accurately in the centre of the stamping platform. Thus, a transferring system driven by seven pneumatic cylinders with different configurations is designed to achieve the movement in two axes (X/Z), as shown in Figure.2.6.

In the X-axis direction, a material support frame (marked in red in the Figure.2.6) is mounted on a pair of parallel guide rails for carrying the experimental samples during the test. As this forming equipment has a large transferring distance, the extension and retraction of the guide rails are necessary to be controlled by a cooperation of three pneumatic cylinders. A cylinder with 150 mm stroke has an opposite direction of movement compared to the other two cylinders with 400 mm stroke, increasing the relative displacement. Then, using a set of rhombic frames, like a horizontal scissor lift, the final overall stroke of the guide rails can reach 1090 mm.

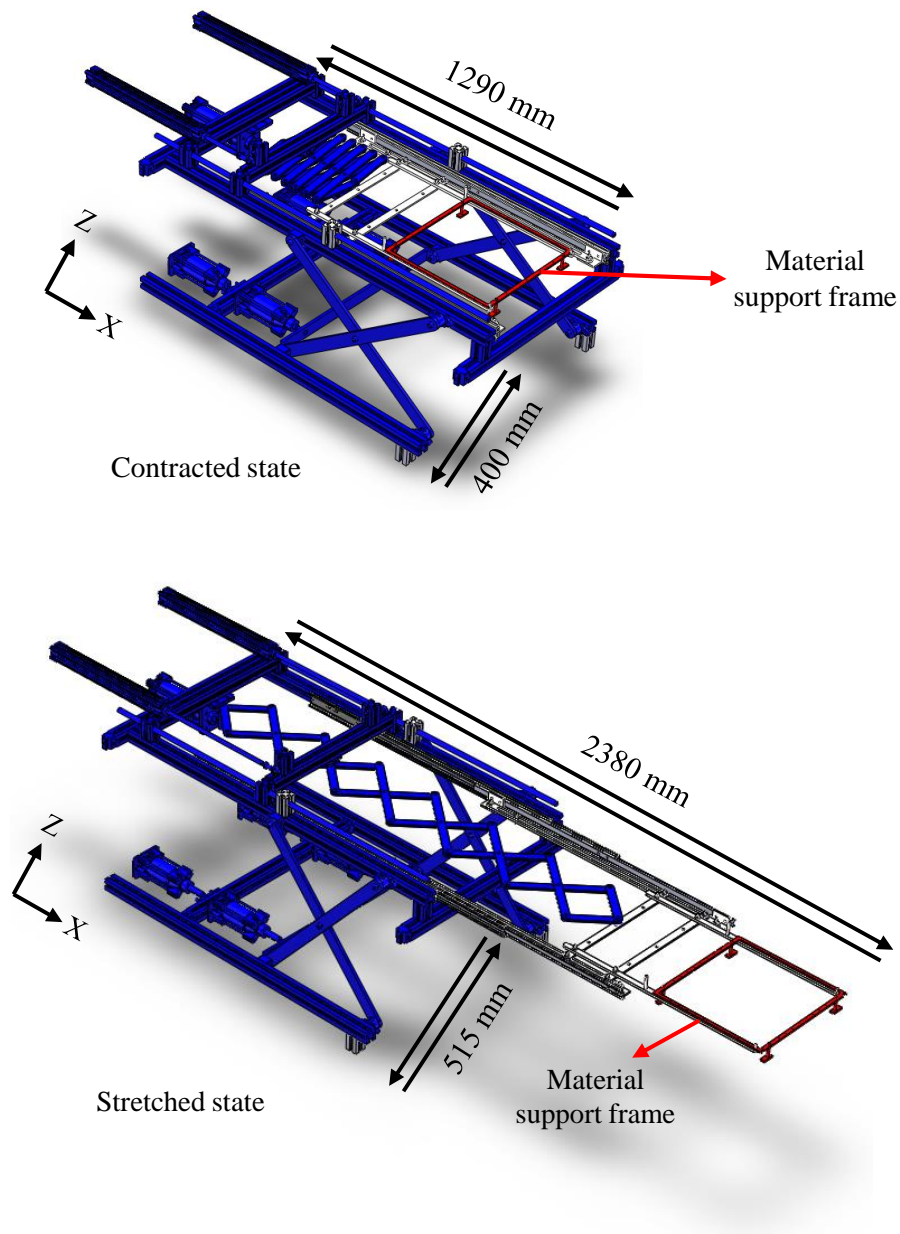


Figure 2.6 Transferring system

The material support frame is a hollow square frame with many small needles on the borders, so that it can give certain tension on the fabric sample during the transmission and avoid the fabric drop from the middle hole. When the support frame is delivered to the forming system, the fabric sample is necessary to be placed on the forming platform to execute the following stamping process. In Figure 2.7, as the support frame goes down and passes through the forming platform, the test sample can be separated from the support frame

by contacting the surface of the blank-holder. This height reduction is attributed to the regulation of the transferring system along Z-axis direction. Four cylinders below (Figure 2.6) owning the same configuration of 50 mm stroke are divided into two groups, so that the height of the guide rails or the support frame can be adjusted twice. Although these cylinders are placed and elongated in horizontal direction, a group of crossed iron bars successfully changes the movement to the vertical direction and obtains a total stroke of 115 mm in height.

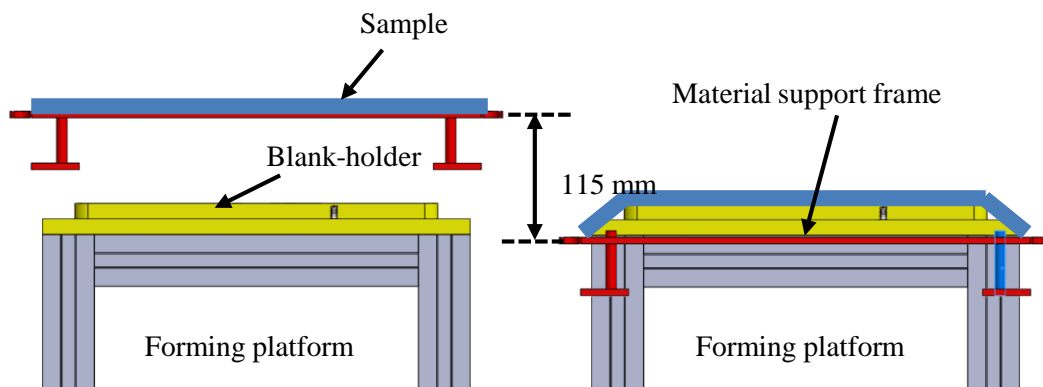


Figure 2.7 The height variation of the material support frame

2.3.6 Forming system

Figure 2.8 shows the detailed structure of the forming system used in the thermoforming equipment. Different from the traditional compression forming system with two matched moulds, a punch/open-die forming system is applied in this design to observe and analyse the behaviour of the prepreg during the whole forming process. It can be seen that in Figure 2.8 the die is movable and driven by 8 cylinders with a stroke of 200 mm. The punch is mounted on a jack with a stroke of 250 mm to reach its target location with a given speed. A load sensor between the punch and the jack permits to record the variation of load during the forming process.

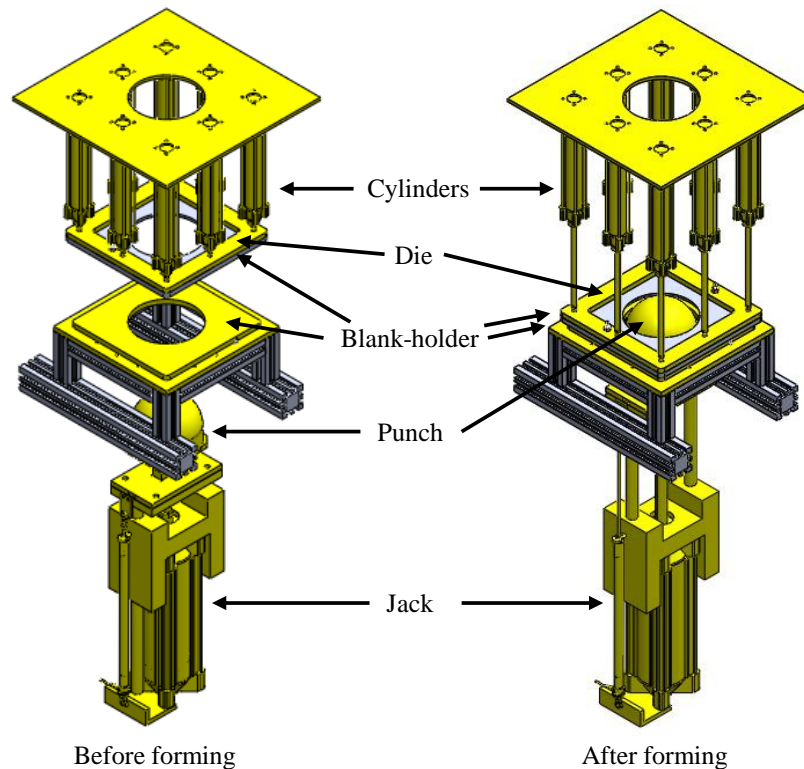


Figure 2.8 Forming system

In order to avoid forming defects, such as wrinkling, a pair of metal blank-holders is used to provide normal pressures on the prepreg surface, so that sufficient tensions can be introduced in the prepreg. The upper blank-holder is connected to the movable die and the lower one is fixed on the forming platform by the positioning bolts. All the pressures offered by pneumatic cylinders can be adjusted based on test requirements. The punches with different double-curved shapes (e.g. hemisphere, square-box, prism and tetrahedron) have been manufactured to investigate the different deformation behaviours.

2.3.7 Assemblage of thermoforming machine

The components of the thermoforming machine have been manufactured in different ways. Some common parts, such as profiles, Plexiglas, pneumatic cylinders and industrial oven, are the existing finished products, which can be bought easily from the commercial market with

good qualities. Some special parts (e.g. punch, blank-holder, material support frame...), which need to be submitted to high temperature or high strain, are made by metal and manufactured by machine tools. At last, some small parts with complex shapes used in the unimportant areas are fabricated through 3D printer. The Figure.2.9 shows the thermoforming machine installed in the GEMTEX laboratory.



Figure 2.9 Photo of thermoforming machine in GEMTEX laboratory

2.4 Conclusion

In this chapter, a detailed introduction of an experimental thermoforming machine used for investigating the formability behaviour of thermoplastic composites has been described. During the thermoforming process, several important heating and pressure parameters, such as preheating temperature, forming pressure and blank-holder pressure, need to be taken into account, as they have a significant influence on the final quality of the composite parts. The designed machine should have the ability to modify these parameters conveniently to meet the different test requirements. For achieving these purposes, this experimental thermoforming machine consists of three main systems, i.e. the heating system, the transferring system and

the forming system. First, the prepreg is preheated over the melting temperature in the oven. Second, contributed to a transferring device driven by a set of pneumatic cylinders, the melted prepreg supported by a metal square frame can be rapidly moved to the forming tool. As last, an appropriate tension in the prepreg is provided by a couple of blank-holders during the forming process in order to minimize the forming defects. A number of punches with different double-curved shapes have been fabricated to investigate the different deformation behaviours.

During the whole assembly process of the thermoforming machine, it always takes a lot of time to purchase or to fabricate the various parts, leading to a long manufacturing cycle eventually. Furthermore, to prevent the considerable temperature drop of the heated materials during its transmission from oven to stamping tool, the original sealed oven has been decided to be replaced by an open infrared oven. Therefore, the thermoforming machine has not been officially put into operation. In order to make full use of the time interval of the machine assembly and further understand the forming mechanism, a set of academic investigations concerning the effect of tufting technique on formability behaviours of multi-layered reinforcements have been carried out simultaneously. The detailed research works will be presented in the following chapters.

2.5 Reference

- [1] Hsiao S-W, Kikuchi N. Numerical analysis and optimal design of composite thermoforming process. *Comput Methods Appl Mech Eng* 1999;177:1–34.
- [2] Offringa AR. Thermoplastic composites—rapid processing applications. *Compos Part A Appl Sci Manuf* 1996;27:329–36.
- [3] Scherer R, Friedrich K. Inter-and intraply-slip flow processes during thermoforming of CF/PP-laminates. *Compos Manuf* 1991;2:92–6.
- [4] Schuster J, Friedrich K. Modeling of the mechanical properties of discontinuous-aligned-fiber composites after thermoforming. *Compos Sci Technol* 1997;4:405–13.
- [5] Walczyk DF, Yoo S. Design and fabrication of a laminated thermoforming tool with

- enhanced features. *J Manuf Process* 2009;11:8–18.
- [6] McCool R, Murphy A, Wilson R, Jiang Z, Price M, Butterfield J, et al. Thermoforming carbon fibre-reinforced thermoplastic composites. *Proc Inst Mech Eng Part L J Mater Des Appl* 2012;226:91–102. doi:10.1177/1464420712437318.
- [7] Gutowski TG. Resin flow/fiber deformation model for composites. *SAMPE Q* 1985;16:58–64.
- [8] Parlevliet PP, Bersee HEN, Beukers A. Residual stresses in thermoplastic composites-A study of the literature-Part I: Experimental techniques. *Compos Part A Appl Sci Manuf* 2007;38:651–65. doi:10.1016/j.compositesa.2006.07.002.
- [9] Khan MA, Mabrouki T, Vidal-Sallé E, Boisse P. Numerical and experimental analyses of woven composite reinforcement forming using a hypoelastic behaviour. Application to the double dome benchmark. *J Mater Process Technol* 2010;210:378–88. doi:10.1016/j.jmatprotec.2009.09.027.
- [10] Hou M. Stam Forming of Continuous Glass Fibre Reinforced Polypropylene 1997;28A:695–702.
- [11] Ten Thije RHW, Akkerman R, Ubbink M, Van Der Meer L. A lubrication approach to friction in thermoplastic composites forming processes. *Compos Part A Appl Sci Manuf* 2011;42:950–60. doi:10.1016/j.compositesa.2011.03.023.
- [12] Schug A, Winkelbauer J, Hinterhölzl R, Drechsler K. Thermoforming of glass fibre reinforced polypropylene: A study on the influence of different process parameters. *AIP Conf Proc* 2017;1896. doi:10.1063/1.5007997.

3. Influence of the tufting pattern on the formability of tufted multi- layered preforms

3.1. Introduction

For obtaining a deep understanding of the forming mechanism during the interval of the machine assembly, the formability of tufted multi-layered preforms has been investigated. As presented in “General introduction”, Liquid Composite Molding (LCM) is one of the main manufacturing processes for the thermoset composites[1,2]. The first step of LCM process is to form dry fabric reinforcements to the desired shape, which can probably induce a complex variation of physical behaviours at the yarn level and influence significantly the next manufacturing stage (resin infusion stage). Therefore, the current and subsequent studies in this thesis concerning the tufted multi-layered preforms have been done on a dry fabric scale.

Tufting, identified as one of the popular textile methods (3D woven, stitching, Z-pinning...[3–9]) for achieving the through-thickness reinforcement (TTR), recently have attracted much attention. Compared to the traditional 2D reinforcement, TTR can present higher delamination resistance. However, due to the through-the-thickness insertion of fibrous structures, the formability behaviours of the original fabric preforms must be significantly modified. Therefore, it is important to understand how the inserted tufting yarns influence the forming behaviours of the fabrics, to find out the effective way to optimize the quality of final composite parts.

Some experimental studies [8,10] have been carried out to investigate the deformability and mechanical properties of 3D woven interlock preform. Some works [11,12] about the effect of stitching patterns on the simple forming behaviours have proved that high stitch density can reduce the material draw-in measurement value and fabric shearing. However, few works are dedicated to the tufted preforms, especially to the investigation of the effect of tufting parameters on forming behaviours.

Liu et al.[13] found that tufting can modify the formability behaviours of the multi-layered preforms. However, their research work is limited to one tufting pattern and one punch shape. Thus, this study aims to further investigate the effect of tufting on the formability behaviours of multi-layered preforms. The influences of tufting density are systematically analysed through two selected tufting patterns (circle and square spiral) in both hemispherical and square-box forming cases. Furthermore, the consistency between the tufting pattern and the punch shape is also discussed.

3.2. Methods and materials

3.2.1 Tufting process

Tufting technology based on the conventional stitching process was invented originally for the manufacture of carpet and recognized recently as an important way to develop the through-the-thickness reinforcement of composites [14,15]. Several industrial devices were designed to automate the tufting process and to achieve the trajectory tracking with the help of a robotic manipulator [14–17]. Equipment shown in Fig.3.1 was developed by GEMTEX laboratory to carry out the tufting process. As the main part of the equipment, tufting head is assembled with a tufting needle linked with a pneumatic jack to control the needle stroke. Thread feeding device ensures a smooth supply of the tufting thread with a certain length and tension. Presser foot device is installed next to the needle to apply a pressure on the preform, the needle starts penetrating it under a guarantee of synchronization. The presser foot is released only when the tufting needle retracts fully from the preform. The framework provides all movements of tufting head along the X and Y axes. The tufting routines and the tufting parameters, such as tufting deepness, tufting pattern and tufting density can be controlled by the computer.

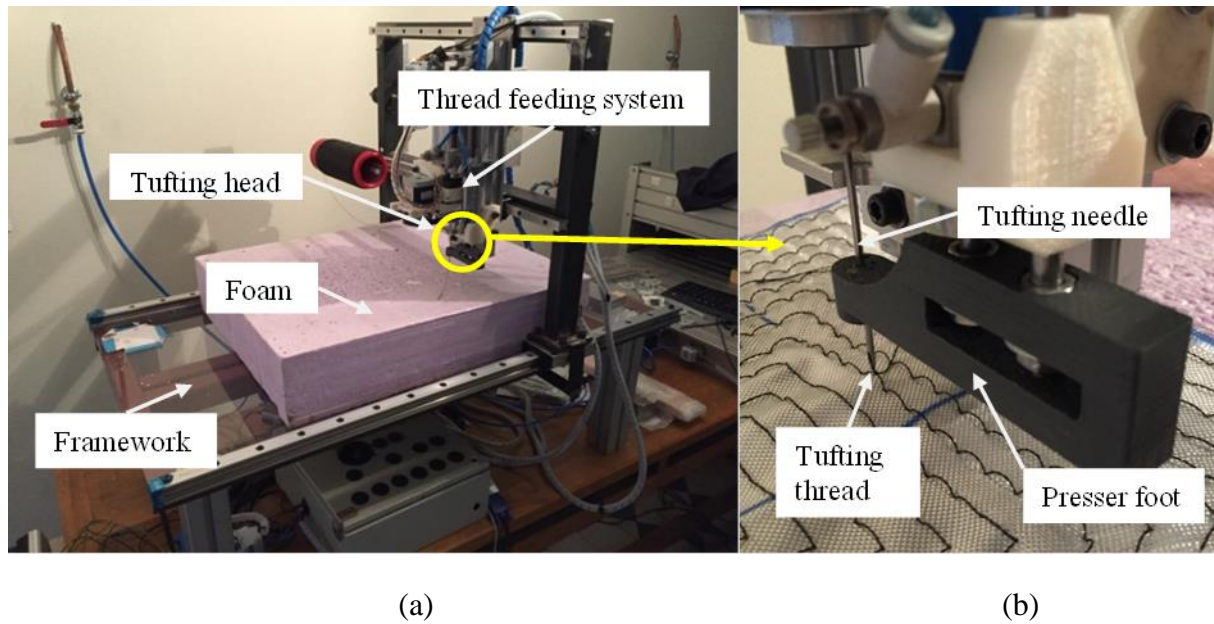


Figure 3.1 Tufting device (a) and zoom of tufting head (b)

3.2.2 Forming device

Fig.3.2 shows the forming device used in the present study to characterize the textile reinforcements formability [10,13,18]. The punch/open-die system can be easily changed to obtain different double curvature shapes. The punch is controlled by an electric jack to reach its target location at a given speed. A load sensor ($500\text{N} \pm 0.3\%$) records the variation of the punch force during the preforming. A continuous video to record the forming process is shot by a digital camera installed just above the specimen. The maximum material draw-in and maximum inter-layer sliding can be measured by the image extracted from this video using imageJ. The pre-tensioning system consists of four pneumatic jacks and two transparent blank-holders. This system permits to apply an adjustable pressure on the fabric. The geometry of the blank-holders can be changed easily according to the punch shape.

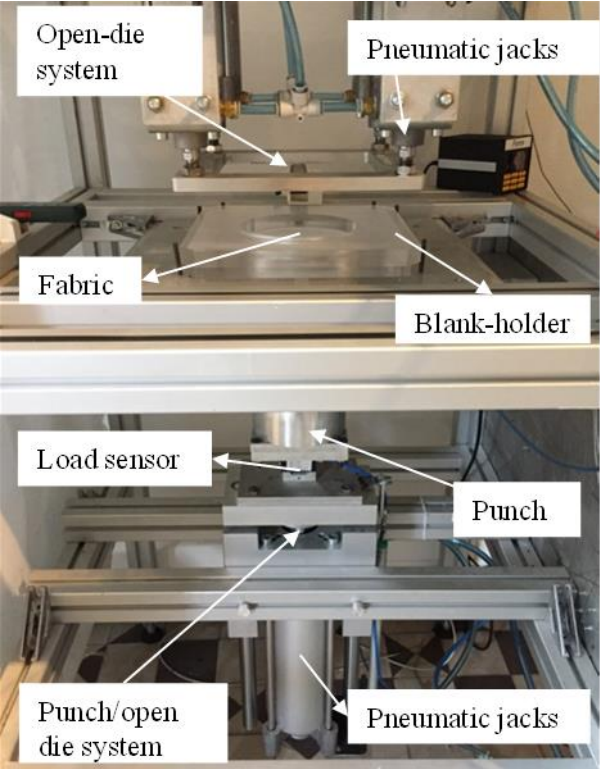


Figure 3.2 The forming device

A hemispherical punch and a square-box punch were chosen in the present study to investigate the influence of different tufting patterns on the formability of tufted preforms. The punch displacement is a constant value which only depends on the punch shape and the stamping speed can be controlled by the punch pressure. The main dimensions and forming parameters are noted in Fig. 3.3 and Table.3.1, respectively.

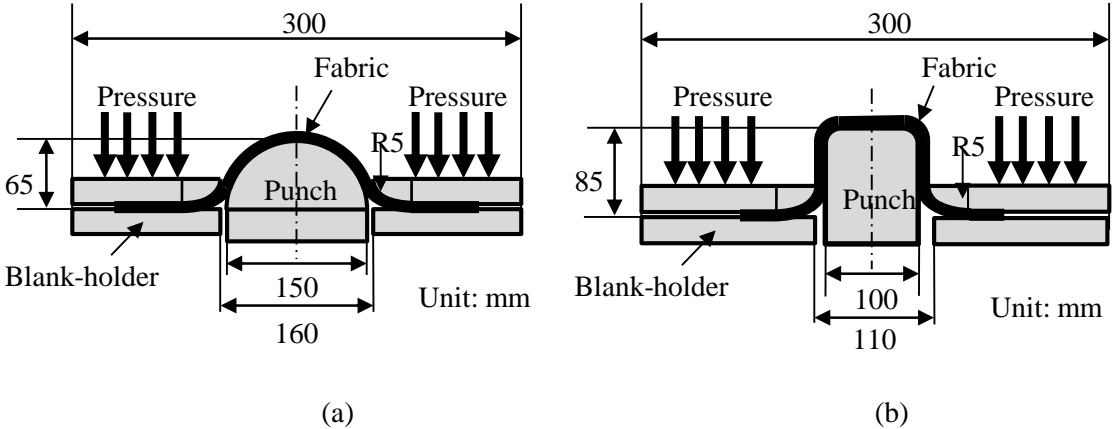


Figure 3.3 Schematic of forming device: (a) Hemispherical punch (b) Square-box punch

Table 3.1 Main parameters of thermoforming process

Parameter	Value
Stamping speed	45 mm/s
Blank-holder pressure	0.05 MPa
Punch pressure	0.2 MPa

3.2.3 Materials

E-glass plain woven fabric with an areal density $157 \pm 5 \text{ g/m}^2$ was used in the forming tests. The preform with a stacking sequence of $[0^\circ/90^\circ, \pm 45^\circ]_2$ is used in the present study. The dimensions of the tested preforms are $280 \times 280 \text{ mm}^2$, with a thickness of $1.1 \pm 0.1 \text{ mm}$. All the samples were tufted with TENAX® carbon thread (2 x 67 tex) via a hollow needle of 2 mm diameter. The tufting patterns are illustrated in Figs.3.4a and b: square spiral and circle spiral. As the important tufting parameters, the tufting space and tufting angle are defined in the different tufting patterns in Fig.3.4. Tufting starts from the centre of the preform to assure that only one tufting thread is used to insert continuously in both warp and weft directions.

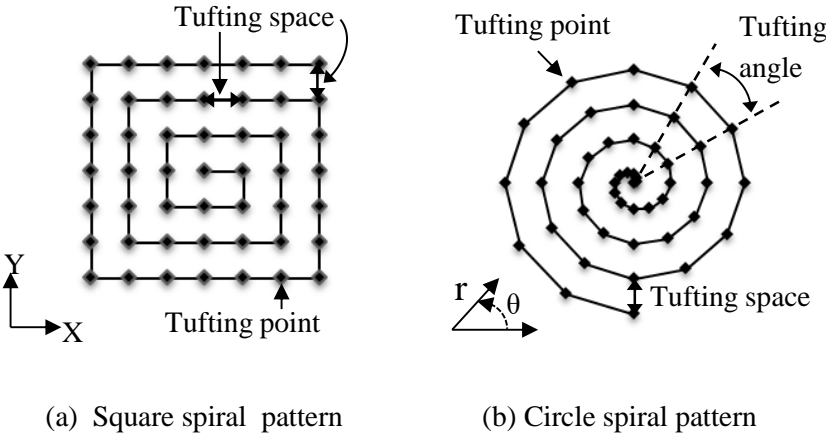
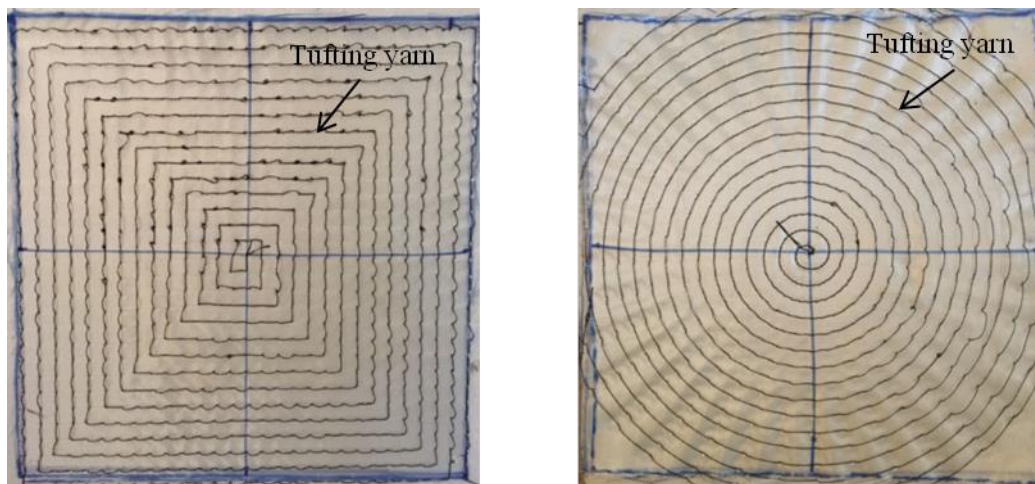


Figure 3.4 Schematic description of the different tufting patterns

Cartesian coordinate system (Fig.3.4a) is chosen for tufting in the square spiral to specify the tufting point, which keeps a constant tufting space in X and Y axes. The circle spiral (Fig.3.4b) is known as the Archimedean spiral, described by the equation (3-1) in polar coordinates (r, θ).

$$r(\theta) = d/2\pi \times (n-1) \times \theta \quad (3-1)$$

Where d is the tufting space between successive turnings; n is the serial number of tufting point on the spiral lattice; θ is the tufting angle between successive tufting points. The top views of samples with the square spiral and circle spiral tufting patterns are shown in Fig. 3.5.



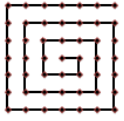
(a) square spiral tufted sample

(b) circle spiral tufted sample

Figure 3.5 Top of view of the tufted preforms with the different tufting pattern

Table 3.2 lists the main properties of tufted preforms used in the present study. The samples of square spiral pattern with the variation of tufting space and of circle spiral pattern with the variation of tufting space and tufting angle were prepared for the forming tests. As the length of the inserted thread is a constant, the areal density depends on the number of tufting points.

Table 3.2 Main properties of the test specimens

Tufting pattern	Ref. of samples	Tufting space (mm)	Tufting angle (°)	Total of tufting points	Areal density (g/m ²)
 Square spiral	S5	5	-	3025	802.3±9.0
	S10	10	-	729	684.9±7.0
	S20	20	-	169	649.2±7.0
 Circle spiral	C10/10	10	10	535	672.2±7.0
	C10/20	10	20	256	659.9±6.0
	C10/30	10	30	182	659.4±5.0
	C20/15	20	15	169	651.8±5.0

3.3. Forming results

Fig.3.6 shows examples of the deformed tufted preforms in hemispherical and square-box forming cases. Since all the specimens were quasi-isotropic and stacked in the same sequence, the way of the sample deformation was symmetric and similar to each other. To quantify the formability, the maximum material draw-in and the maximum inter-layer sliding were used to be the indicators of the extent of global deformation. All the measurement data was obtained as the mean values at the centre of four sides in the Fig.3.6. The measurement data with a good reproducibility was achieved by repeating the preforming tests 3 times.

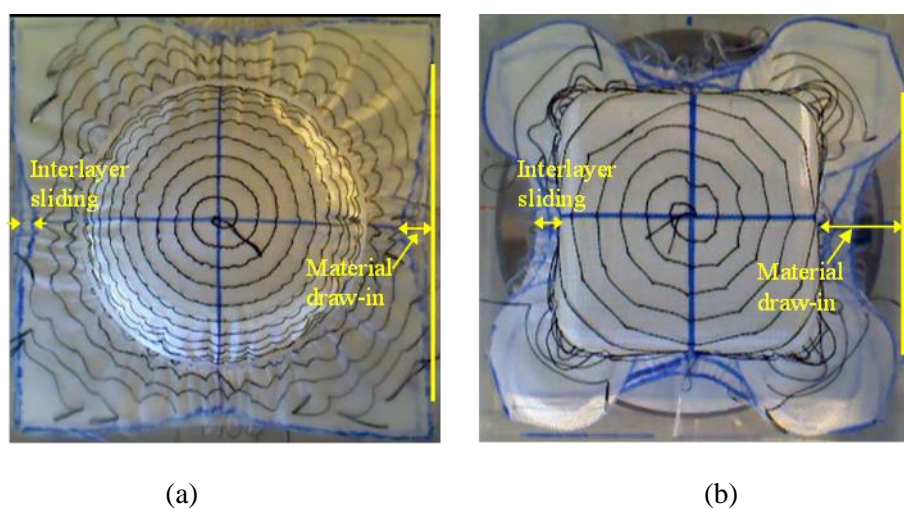
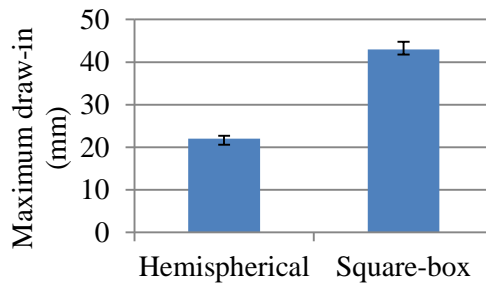
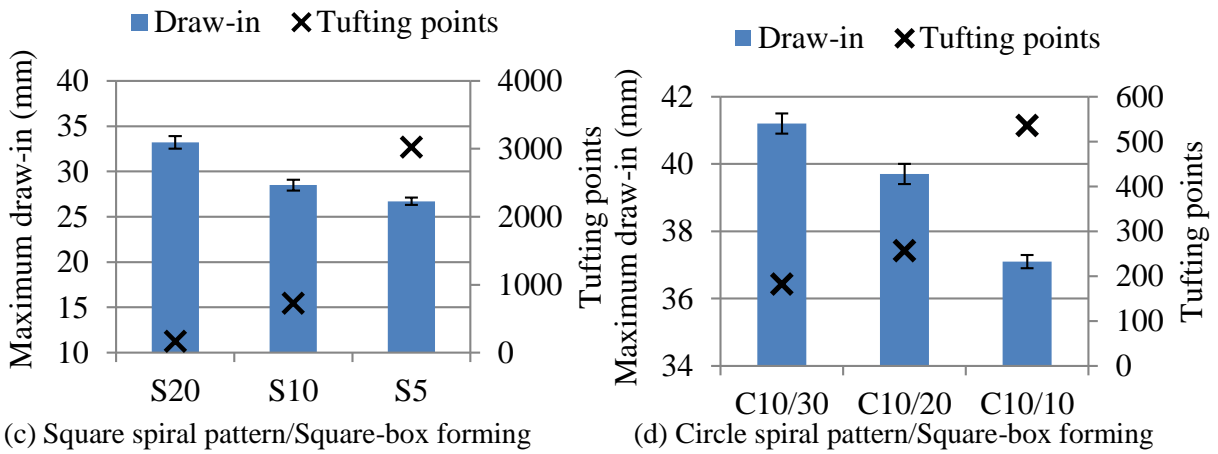
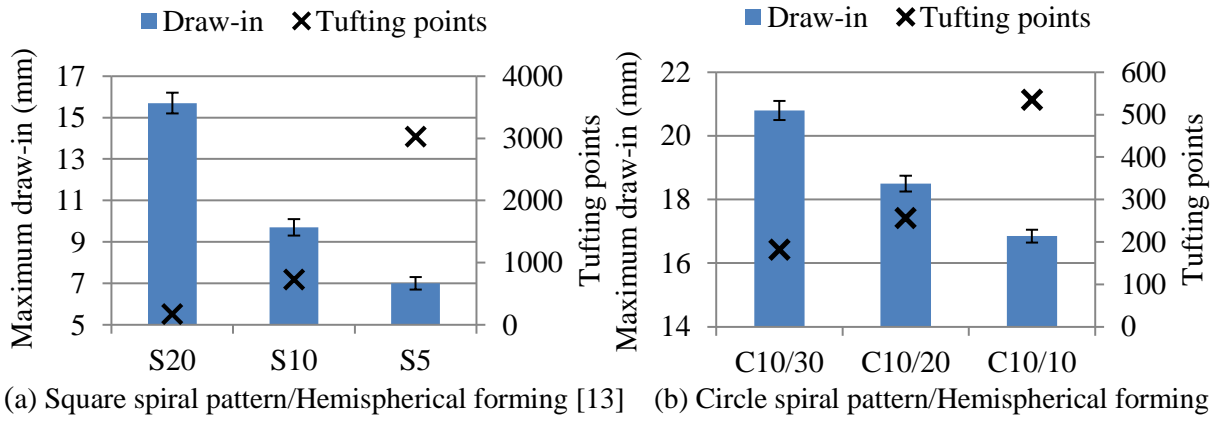


Figure 3.6 Deformed tufted preforms after forming, (a) hemispherical forming using C10/10 sample and (b) square-box forming using C10/30 sample

3.3.1 Material draw-in and punch load

The tufted preforms with different tufting patterns were tested in hemispherical and square-box forming processes. The bar graph and the cross symbol graph shown in Figs.3.7 (a)-(d) are the representation of the maximum material draw-in and the number of tufting points, respectively. Impact of tufting points can be noted clearly in the figures. The material draw-in decreases with the increasing of tufting points. The inserted tufting threads strengthen the reinforcement through-the-thickness and bring in stronger linkage among the layers. The preforms become more rigid and are more difficult to be deformed along with the increase of tufting points, which also can be confirmed by the observation of the required punch load demonstrated in Figs.3.8 (a)-(d). On the other hand, for the non-tufted samples (Fig.3.7e and Fig.3.8e), a larger material draw-in and a lower punch load compared to the tufted samples further reflect this tufting effect.

For the square spiral pattern, compared to the S20 sample, the maximum draw-in of S5 sample decreases 56% and 19% in the hemispherical and square-box forming respectively. In the same way, for circle spiral pattern, compared to the C10/30 sample, the maximum draw-in of C10/10 reduces 19% and 9% after the hemispherical and square-box forming, respectively. It can be concluded that the influence of tufting density on the maximum material draw-in in hemispherical forming is more prominent than in square-box forming.



(e) Non-tufted sample in both forming

Figure 3.7 Influence of tufting pattern and density on the maximum material draw-in in the hemispherical and square-box forming

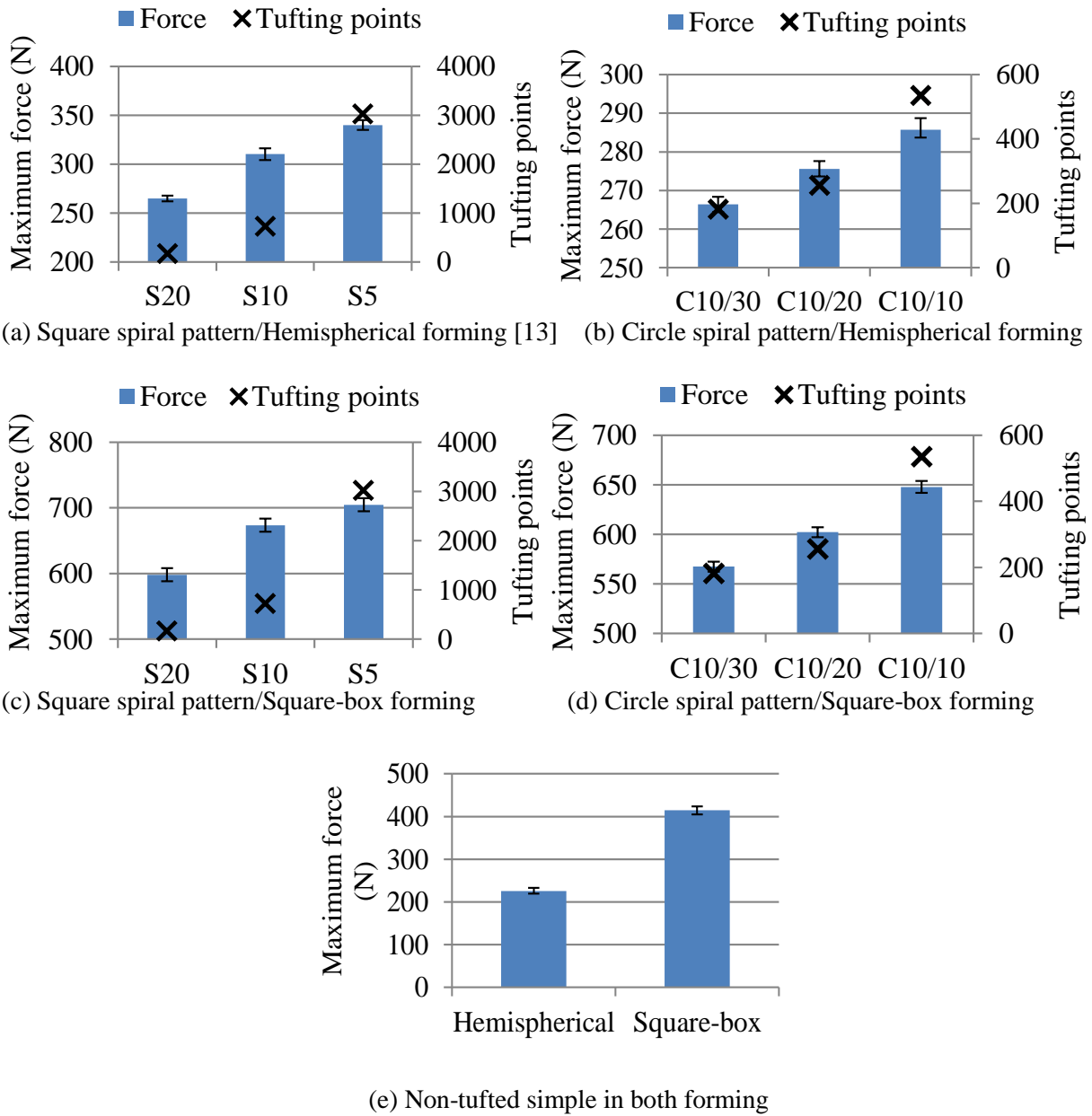
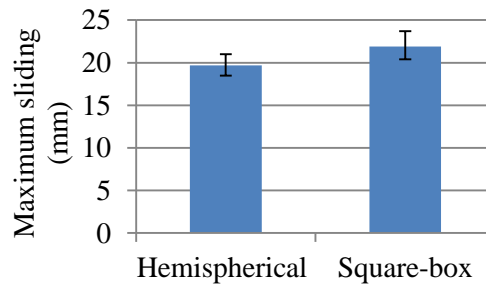
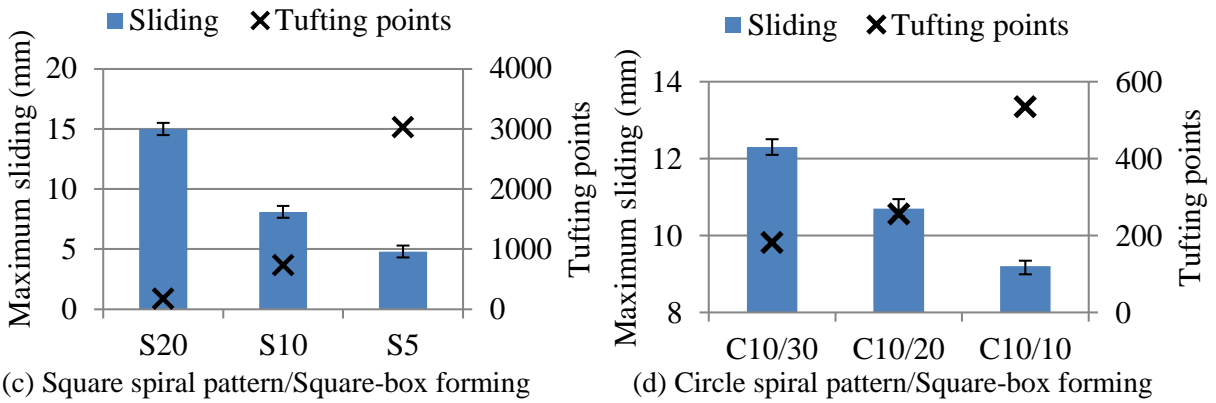
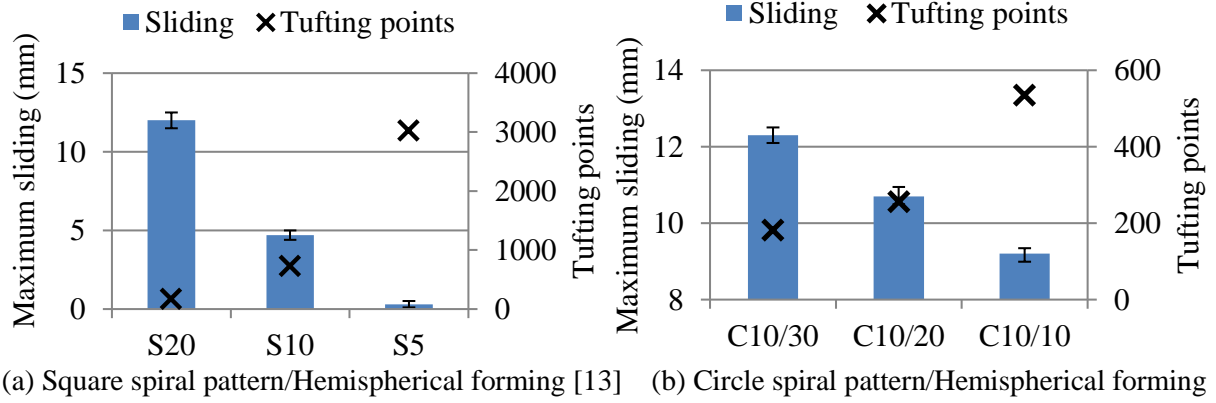


Figure 3.8 Influence of tufting pattern and density on the maximum punch load in the hemispherical and square-box forming

3.3.2 Inter-layer sliding

As one of the important behaviour in the multi-layered forming, inter-layer sliding is mainly caused by the different deformation of each ply and slightly influenced by the changed curvature, considering the ply thickness. In this study, the maximum measurement value is used to represent the severity of inter-layer sliding for each sample. Figs.3.9 show the maximum inter-layer sliding of preforms measured in hemispherical and square-box forming. When no tufting yarns are inserted into the multi-layered fabric (Fig.3.9e), a large interlayer sliding can be achieved in both forming cases. On the contrary, in Fig.3.9a-d, it can be observed that the inter-layer sliding can be much reduced owing to the increase of tufting points (tufting density) in both hemispherical and square-box forming. In the case of S5 sample tested in hemispherical forming, the tufted multi-layered preforms even can be regarded as a whole, as the interlayer sliding is able to be ignored.



(e) Non-tufted simple in both forming

Figure 3.9 Influence of tufting pattern and density on the maximum interlayer sliding in the hemispherical and square-box forming

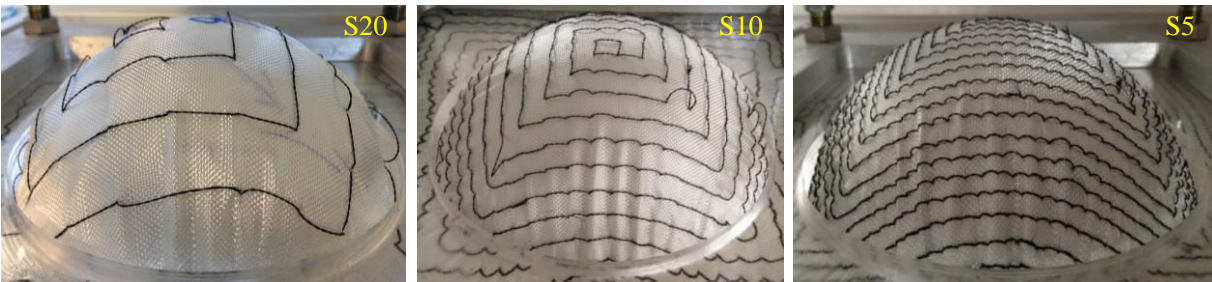
3.3.3 Wrinkling

Wrinkling is one of the common defects experienced in the textile composite reinforcements forming. It has a trend to degrade the performance of the final product. Wrinkles occur as the energy needed for an out-of-plane deformation is less than that for an in-plane deformation[19]. The out-of-plane deformation depends on the bending stiffness, which is normally weak due to the probable relative motion of fibres. The size of the wrinkles increases along with the bending stiffness[20,21]. Several other parameters can also affect the wrinkling phenomenon during forming process, such as the variations of boundary condition and laminate sequences. Fig.3.10 shows the forming results of non-tufted samples in the hemispherical and square-box forming cases. Some large wrinkles with a non-regular shape can be observed in these cases. Previous test[13] in regard to the square spiral pattern working on the hemispherical punch has revealed that wrinkling phenomenon can be modified by tufting (Figs.3.11a). Wrinkles are more regularly distributed and the size of wrinkle can be reduced due to the increase of tufting density. This result has been further confirmed by using circle spiral pattern and square-box punch shape.

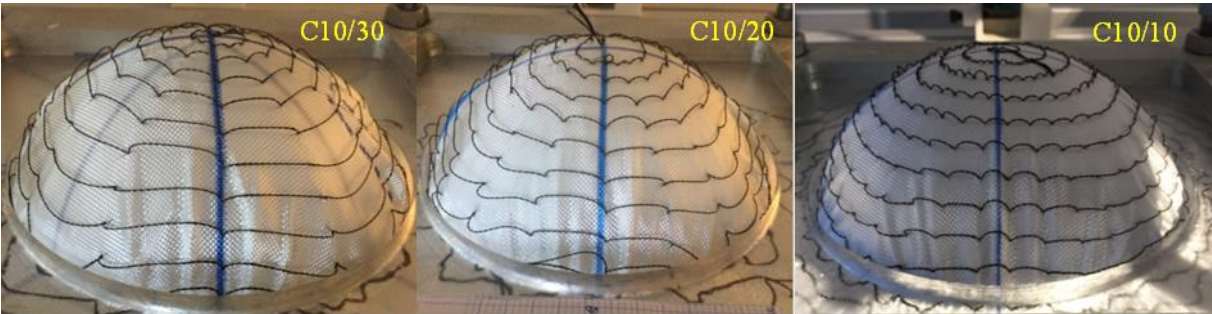


Figure 3.10 Wrinkling phenomenon in (a) hemispherical and (b) square-box forming

Figs.3.11b shows the wrinkling phenomenon magnified in the punch zone and obtained from the preforms tufted in circle spiral pattern during the hemispherical forming. It can be observed that the sizes of wrinkles can be apparently reduced as the decreasing of the tufting angle (increasing of the tufting density). Since the tufting yarn can enhance the combination between layers, the voids inside the fabric are able to be eliminated at the location of tufting points, leading to the wrinkles normally appearing between these tufting points. Consequently, the width of wrinkles can be effectively reduced owing to the increase of tufting density.



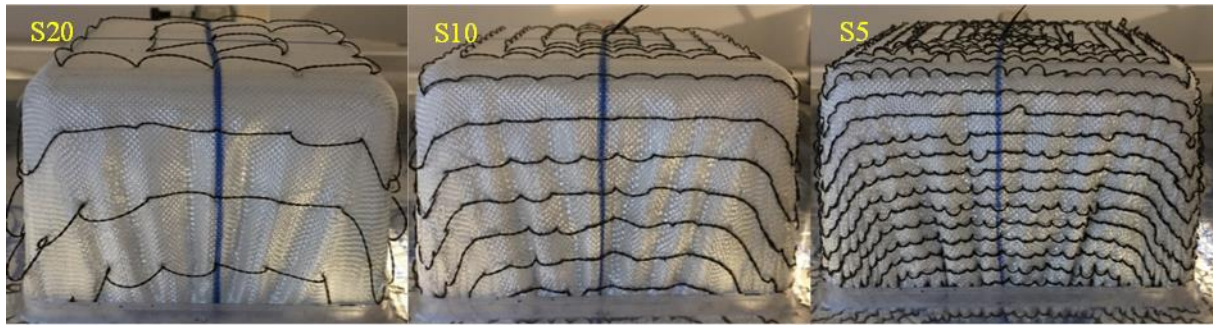
(a) Forming of the tufted preforms with the square spiral pattern [13]



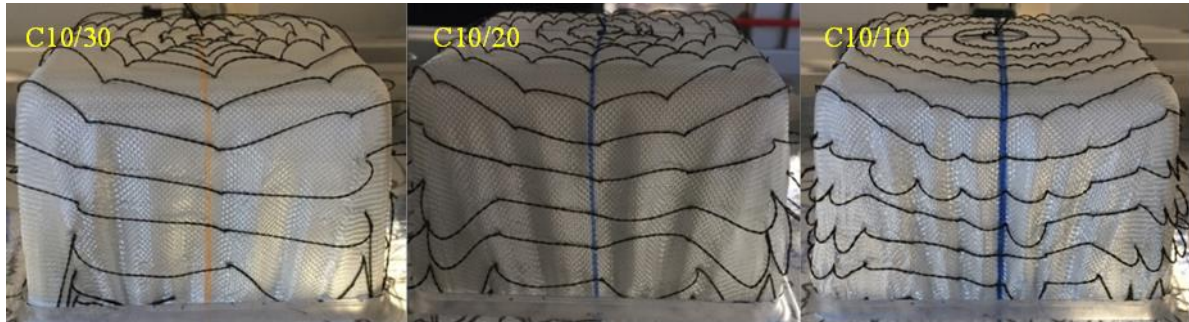
(b) Forming of the tufted preforms with the circle spiral pattern

Figure 3.11 Influence of tufting pattern and density on the wrinkling phenomenon in the hemispherical forming

In the square-box forming, the wrinkles are distributed on the four lateral surfaces. No matter what kind of tufting pattern (circle spiral/ square spiral) is used, it is always observed that the width of wrinkles can be reduced along with the increase of tufting density. However, this tufting effect seems to have a limit, as the wrinkles can only be weakened but not able to be removed completely.



(a) Forming of the tufted preforms with the square spiral pattern



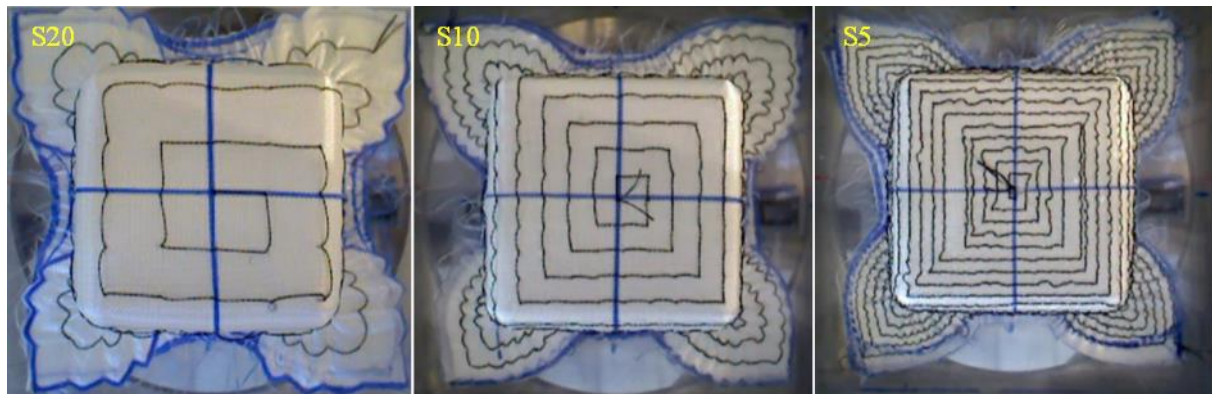
(b) Forming of the tufted preforms with the circle spiral pattern

Figure 3.12 Influence of tufting pattern and density on the wrinkling phenomenon in the square-box forming

3.3.4 *Out-of-plane defects*

Out-of-plane defects identified as the buckles at the scale of tufting yarn can be observed at the four corners in the square-box forming. As noted in Figs.3.12b and 3.13b, these buckles are noted only for the preforms tufted with the circle spiral pattern. The tufting yarns between two tufting nodes at the corner become curved when the preform accommodates the change of punch geometry. Since the fabric is submitted to a high level of shear deformation at the four corners, this high shear deformed state conducts to a decrease of the distance of the adjacent tufting points. As a result, in these zones, the buckles of tufting yarn appear. In addition, the buckling phenomenon is less important when the tufting angle is small. It can be considered that following the decrease of tufting angle, more tufting points are distributed at the corner of the preform. The initial big buckle can be divided into some small buckles due to the increase of tufting points. On the contrary, when the square spiral pattern is used, no distinct buckling

phenomenon is observed (Figs.3.12a and 3.13a). As for the square spiral pattern, the tufting yarn is embedded along the weft or warp direction. When the shear deformation takes place at the corner, the distance between two tufting points is not changed due to its synchronous deformation along with the yarn network.



(a) With the square spiral pattern



(b) With the circle spiral pattern

Figure 3.13 Top view of the deformed preforms with the different tufting pattern

3.4. Discussion

In order to analyse the consistency between tufting pattern and punch shape, two types of sample are chosen (S20 and C20/15). Their main parameters are listed in Table.3.3. Although the samples are tufted with different tufting patterns, the areal density and the total tufting points are the same. Furthermore, the tufting points located in the specific zone are also different in these two selected samples.

Table 3.3 Main parameters of S20 and C20/15 samples.

Forming	Ref. of samples	Areal density (g/m ²)	Tufting points		
			Total points	Tufting points in punch zone	Tufting points in the zone underlying the blank holder
Hemispherical forming	S20	649.2±7.0	169	97	72
	C20/15	651.8±5.0	169	133	36
Square-box forming	S20	649.2±7.0	169	129	40
	C20/15	651.8±5.0	169	141	28

Figs.3.14 and 3.15 present the comparison results between S20 and C20/15 samples in the hemispherical and square-box forming cases. It can observe that S20 sample have smaller material draw-in/interlayer sliding and higher the forming load compared to C20/15 sample. Considering the distribution of tufting points in S20 and C20/15 samples, it hints that the tufts in the zone underlying the blank holder can bring more limitation between the layers during the forming. Consequently, the tufting points in the zone underlying the blank holder have a more significant influence on the formability behaviours compared to the influence of consistency between the tufting pattern and the punch shape.

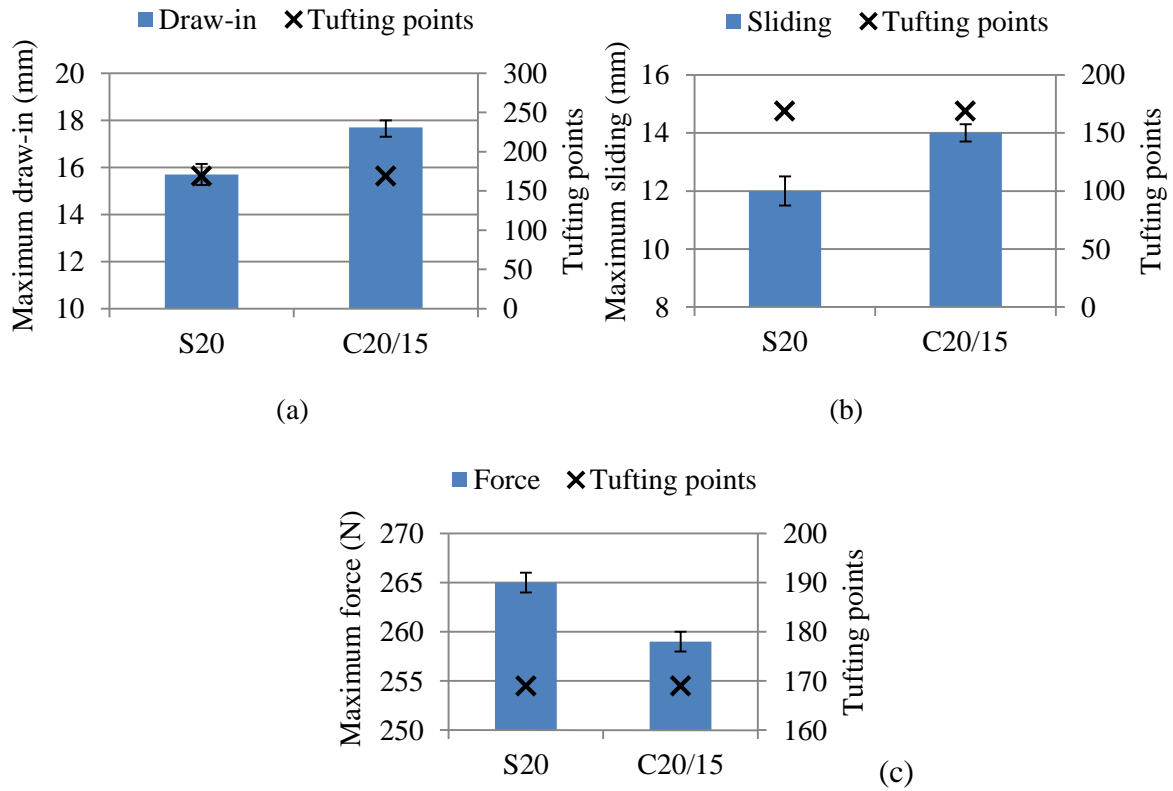


Figure 3.14 The comparison of two tufting patterns during hemispherical forming

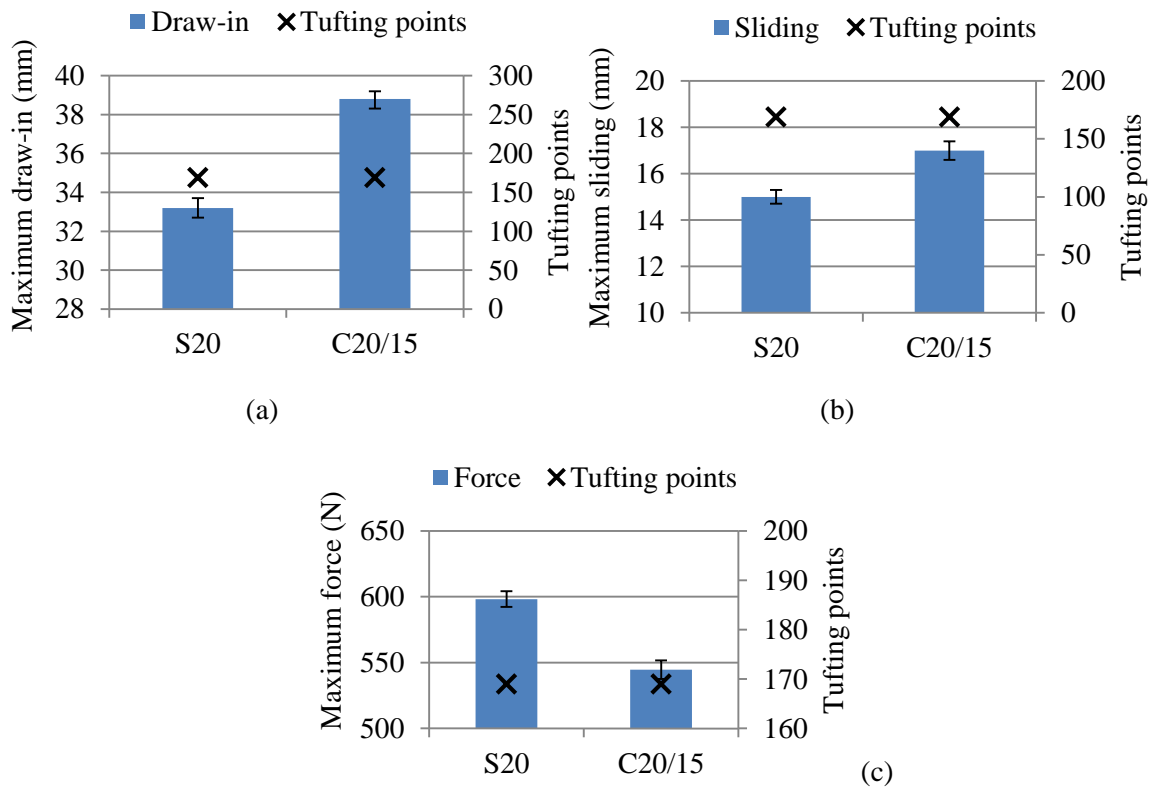
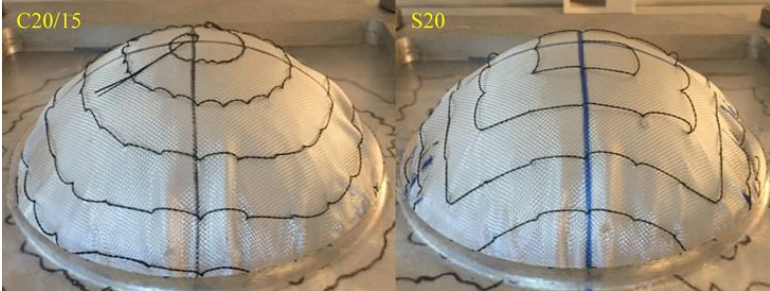
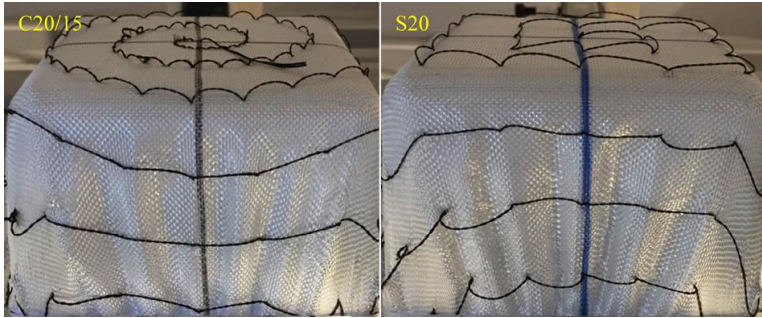


Figure 3.15 The comparison of two tufting patterns during square-box forming

For the wrinkling phenomenon, it seems that no apparent difference of the number and the position of the wrinkles can be observed by using different tufting patterns in both forming cases (Fig.3.16). However, the width of wrinkles in S20 sample seems to be slightly smaller compared to C20/15 sample. It is probably caused by the different tufting distribution in these two patterns, as more tufting points located in the zone underlying the blank-holder in S20 sample can generate higher frictions between the blank-holders and the fabric leading to a higher tension in the fabric during forming process. Consequently, the wrinkling phenomenon depends on the number of the tufting points in the zone underlying the blank-holder to some extent.



(a) Hemispherical forming



(b) Square-box forming

Figure 3.16 The comparison of wrinkling phenomenon between two tufting patterns

The out-of-plane defects as the buckles of tufting yarn can be always observed in the circle spiral tufted preforms forming (Fig.3.17). Therefore, using the square spiral pattern can avoid the generation of this out-of-plane defects located in the high shear deformation zone. In addition, if the preform is not submitted to a high shear deformation, both two patterns can be applied for tufting. The out-of-plane phenomenon can be also mitigated by the increase of tufting density in the use of the circle spiral pattern.

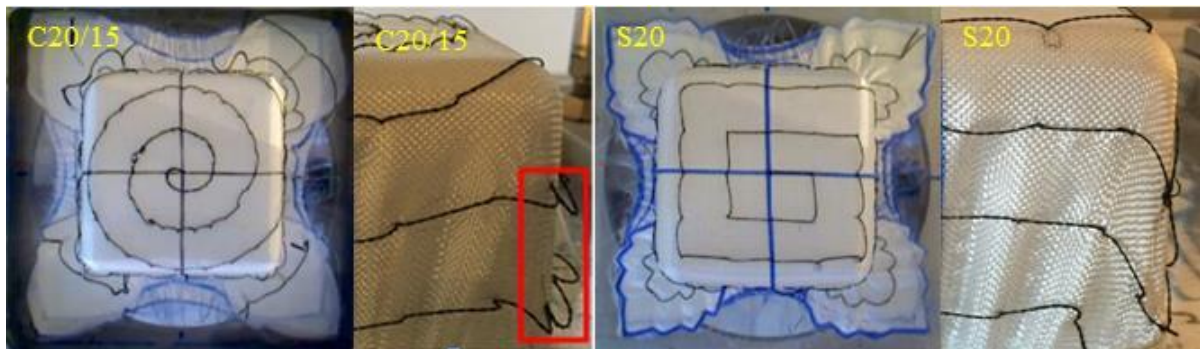


Figure 3.17 The out-of-plane defects during in the tufted preforms forming

3.5. Conclusion

The present study is mainly focused on the formability behaviours of tufted multi-layered preforms in both hemispherical and square-box forming cases. A high tufting density can significantly reduce the interlayer slippage and material draw-in, making the fabrics deform more uniformly. At the same time, the wrinkling phenomenon can be also modified due to the presence of tufting yarns. The original big wrinkles are divided into some small pieces at the location of tufts, which hints that the tufts can effectively eliminate the void inside the fabric by providing a stronger combination between layers. However, this effect will be prominently weakened when the tufting density exceed a limit. The discussion about the consistency between tufting pattern and punch shape shows that there is no significant importance to use the similar tufting pattern to the punch shape. But the circle spiral pattern is not suitable for the square box forming, as the out-of-plane defects, defined as the buckles of tufting yarns, can be induced at the corners even if a high tufting density is employed. Moreover, the experimental results suggest that the forming behaviour depends on the number of tufting points, in particular in the zone underlying the blank holder.

A further optimization of tufting patterns in some specific zone to minimize the forming defects will be implemented in the next chapter. On the other hand, based on the observation of wrinkling in this study, it is important to establish an effective evaluation system to characterize the wrinkling phenomenon, which will be another main subject presented in the following part.

3.6. References

- [1] Rudd CD, Long AC. *Liquid Molding Technologies*, Cambridge: Woodhead Pub 1997.
- [2] Šimáček P, Advani SG. Desirable features in mold filling simulations for liquid composite molding processes. *Polym Compos* 2004;25:355–67. doi:10.1002/pc.20029.
- [3] Gnaba I, Legrand X, Wang P, Soulat D. Literature review of tufted reinforcement for composite structures. *IOP Conf Ser Mater Sci Eng* 2017;254. doi:10.1088/1757-899X/254/4/042011.
- [4] Mouritz AP. Review of z-pinned composite laminates. *Compos Part A Appl Sci Manuf* 2007;38:2383–97.
- [5] Mouritz AP, Bannister MK, Falzon PJ, Leong KH. Review of applications for advanced three-dimensional fibre textile composites. *Compos Part A Appl Sci Manuf* 1999;30:1445–61.
- [6] Mouritz AP, Cox BN. A mechanistic interpretation of the comparative in-plane mechanical properties of 3D woven, stitched and pinned composites. *Compos Part A Appl Sci Manuf* 2010;41:709–28.
- [7] M'membe B, Gannon S, Yasae M, Hallett SR, Partridge IK. Mode II delamination resistance of composites reinforced with inclined Z-pins. *Mater Des* 2016;94:565–72. doi:10.1016/j.matdes.2016.01.051.
- [8] Zhang Y, Sun F, Wang Y, Chen L, Pan N. Study on intra/inter-ply shear deformation of three dimensional woven preforms for composite materials. *Mater Des* 2013;49:151–9.
- [9] Gereke T, Cherif C. A review of numerical models for 3D woven composite reinforcements. *Compos Struct* 2018.
- [10] Dufour C, Wang P, Boussu F, Soulat D. Experimental Investigation About Stamping Behaviour of 3D Warp Interlock Composite Preforms. *Appl Compos Mater* 2014;21:725–38. doi:10.1007/s10443-013-9369-9.
- [11] Molnar P, Ogale A, Lahr R, Mitschang P. Influence of drapability by using stitching technology to reduce fabric deformation and shear during thermoforming. *Compos Sci Technol* 2007;67:3386–93.
- [12] Abteu MA, Boussu F, Bruniaux P, Loghin C, Cristian I, Chen Y, et al. Forming characteristics and surface damages of stitched multi-layered para-aramid fabrics with various stitching parameters for soft body armour design. *Compos Part A Appl Sci Manuf* 2018;109:517–37.
- [13] Liu LS, Zhang T, Wang P, Legrand X, Soulat D. Influence of the tufting yarns on formability of tufted 3-Dimensional composite reinforcement. *Compos Part A Appl Sci Manuf* 2015;78:403–11. doi:10.1016/j.compositesa.2015.07.014.

- [14] Cartié DDR, Dell'Anno G, Poulin E, Partridge IK. 3D reinforcement of stiffener-to-skin T-joints by Z-pinning and tufting. *Eng Fract Mech* 2006;73:2532–40. doi:10.1016/j.engfracmech.2006.06.012.
- [15] Dell'Anno G, Treiber JWG, Partridge IK. Manufacturing of composite parts reinforced through-thickness by tufting. *Robot Comput Integr Manuf* 2016;37:262–72. doi:10.1016/j.rcim.2015.04.004.
- [16] Chehura E, Dell'Anno G, Huet T, Staines S, James SW, Partridge IK, et al. On-line monitoring of multi-component strain development in a tufting needle using optical fibre Bragg grating sensors. *Smart Mater Struct* 2014;23. doi:10.1088/0964-1726/23/7/075001.
- [17] Henao A, Carrera M, Miravete A, Castejón L. Mechanical performance of through-thickness tufted sandwich structures. *Compos Struct* 2010;92:2052–9. doi:10.1016/j.compstruct.2009.11.005.
- [18] Labanieh AR, Garnier C, Ouagne P, Dalverny O, Soulat D. Intra-ply yarn sliding defect in hemisphere preforming of a woven preform. *Compos Part A Appl Sci Manuf* 2018;107:432–46. doi:10.1016/j.compositesa.2018.01.018.
- [19] Allaoui S, Cellard C, Hivet G. Effect of inter-ply sliding on the quality of multilayer interlock dry fabric preforms. *Compos Part A Appl Sci Manuf* 2015;68:336–45. doi:10.1016/j.compositesa.2014.10.017.
- [20] Liang B, Hamila N, Peillon M, Boisse P. Analysis of thermoplastic prepreg bending stiffness during manufacturing and of its influence on wrinkling simulations. *Compos Part A Appl Sci Manuf* 2014;67:111–22. doi:10.1016/j.compositesa.2014.08.020.
- [21] Boisse P, Hamila N, Vidal-Sallé E, Dumont F. Simulation of wrinkling during textile composite reinforcement forming. Influence of tensile, in-plane shear and bending stiffnesses. *Compos Sci Technol* 2011;71:683–92. doi:10.1016/j.compscitech.2011.01.011.

4. Characterisation and optimisation of wrinkling during the forming of tufted three-dimensional composite preforms

4.1. Introduction

In Chapter 3, the effects of tufting density on wrinkling phenomenon have been confirmed using a set of tufting patterns and a couple of punch shapes. It has been found that the tufting points in the peripheral zone (underlying the blank-holders after forming) have a significant impact on the global wrinkling phenomenon. Therefore, the tufting effect in some local areas will be revealed in this chapter. At the same time, an accurate assessment of these wrinkles is quite necessary to be established.

In the published literatures, some image analysis methods have been applied to achieve wrinkling evaluation. Lee et al. [1] have quantitatively characterized the wrinkling level of a non-crimp fabric preform via the effect of the wrinkled surface on the scattering of laser light. Domskiene et al. [2] investigated the deformation behavior of woven fabric and detected the onset of wrinkling, again relied on the scattering of light from the specific direction. More recently, three-dimensional (3D) shape reconstruction becomes a more popular technology which has been used to characterize the textile deformation. Christ et al. [3] measured the draping effects (gaps, loops, wrinkles, and fiber misalignment) using a laser triangulation sensor with a Textecho commercial system. Arnold et al.[4] analyzed wrinkle formation during draping of non-crimp fabrics by the distance computation among a group of z-stack images. Although there is a range of techniques which can adequately measure wrinkles, most of these methods are limited to the wrinkling observation from a constant/restricted direction or to a necessary requirement of expensive equipment.

Therefore, in this study, a simple and cheap numerical method based on the Structure from Motion technique (SFM) is developed to characterize the wrinkles on the surface of the multi-layered woven preforms reinforced by tufting from diverse views. The image analysis and different wrinkling indicators provide a general assessment to identify which kind of tufting

patterns would be the most appropriate one for a given punch shape. Moreover, these assessment data would be some critical features needed in the future simulation work.

4.2. Materials and methods

4.2.1 Tufting process and tufted preforms

The tufting technology as a relatively novel method in the manufacture of through-thickness composites was described in Chapter 3. All the test samples in this study were fabricated by the automated tufting machine developed in GEMTEX laboratory with a tufting deepness of 30 mm. Commercial E-glass plain woven fabric with an areal density of 157 ± 5 g/m² was used in this study. The four-layer samples were stacked in a sequence of $[0^\circ/90^\circ, \pm 45^\circ]_2$ (Fig.4.1). The surface dimension of individual preform was 280×280 mm² in hemispherical forming. This size was increased to 300×300 mm² in square-box forming, as more fabric was used to accommodate the punch shape. After being simply piled up, a 67 tex twisted carbon thread (TENAX®) was tufted into the fabrics through a hollow needle of 2 mm diameter.

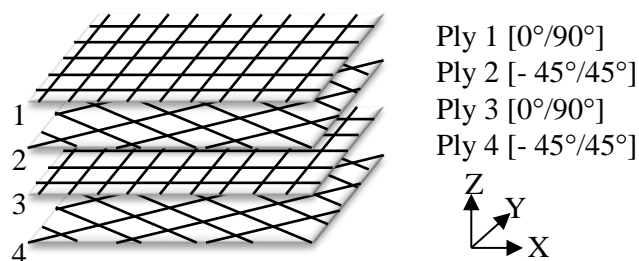


Figure 4.1 Schematic of stacking sequence.

The original square preforms will be divided into two investigation zones after forming, since the centre zone of the preforms will be deformed to the punch shape (hemispherical or square-box) and the peripheral zone will still remain between the blank-holders. The effects

of tufting in the centre zone and the peripheral zone on forming defect are studied respectively. The tufting contours and some important parameters of fabrics are shown in Table 4.1. In hemispherical forming, the first three tufting patterns including Circle-Axis zone Tufting (CAT), Circle-Complete zone tufting (CCT) and Circle-Diagonal zone Tufting (CDT) have similar tufting points in peripheral zone. For the other two remaining, non-tufting (NT) and Circle-Punch zone Tufting (CPT) are used as a reference for examining the effects of tufting. All the samples in hemispherical forming are tufted in a circle spiral pattern with same trajectory in center zone to avoid the experimental results from extra interference and to match the punch shape. Furthermore, as the quasi-isotropic preforms are composed of $0^\circ/90^\circ$ and $\pm 45^\circ$ layers, the tufting yarns in peripheral zone are deliberately distributed along $0^\circ/90^\circ$ or $\pm 45^\circ$ directions. The similar tufting locations are also investigated in square-box forming and circle spiral pattern is switched to square spiral pattern in the centre to correspond to the punch shape, leading to the change of initial of the sample abbreviations from C to S.

Table 4.1 Main properties of the test samples.

Ref. of samples	Tufting pattern	Tufting points in center zone	Tufting points in peripheral zone	Sample area (mm)	Areal density (g/m ²)
CAT		324	512	280×280	693.8±7.0
CCT		324	504	280×280	689.8±6.0
CDT		324	512	280×280	694.4±7.0
CPT		324	0	280×280	663.2±6.0
NT		0	0	280×280	628.3±5.0
SAT		441	288	300×300	684.9±8.0
SCT		441	288	300×300	678.4±6.0
SDT		441	288	300×300	685.8±8.0
SPT		441	0	300×300	671.3±6.0
NT		0	0	300×300	627.7±6.0

4.2.2 Forming process

The forming device used in this investigation is also described in Chapter 3. Again, the hemispherical and square-box punches have been chosen for observing different deformations. The main dimensions of the forming device with different punch shapes are illustrated in Figs.3.4. The pressure of blank-holder is always set to 0.05 MPa, which is the value of one of the four pneumatic jacks. The punch is actuated by an independent pneumatic jack under a pressure of 0.2 MPa with a constant velocity of 45 mm/s during the entire movement.

4.2.3 Image-analysis of deformed preforms

Structure from Motion (SFM) [5–7], a measurement method originating from computer vision techniques, is proposed to characterize the wrinkling phenomenon on the shaped fabric in this study. The key point of SFM processing is to find out the 3D location of matching features in multiple photographs, taken from different angles. For solving this problem, the Scale Invariant Feature Transform (SIFT) object recognition system has been widely used[8]. Contributed to this algorithm, the identified features in each image are invariant to the image scaling and rotation and partially invariant to the changes in illumination conditions and 3D camera viewpoint [9]. Meanwhile, the accuracy of the method depends on the image details, including the surface texture of the target object, the density, sharpness and resolution of the photoset.

The SFM method has been applied successfully in many geomorphic studies[9–11], as the geometry of the scene, camera orientations and positions are solved automatically with no need to specify the priority. The ground control point (GCP) data extracted from GPS surveying can be entered directly into the software in order to scale and orient the point cloud. Furthermore, some unreachable nature landscapes can also be characterized precisely with the help of the remote-controlled drone equipped with a high resolution camera. This image-

based modelling technology plays also a fundamental role in the protection of cultural heritage, where the photogrammetric survey of complex geometries is needed[12]. Actually, the size of the generated point-clouds via SFM algorithms is relative and must be calibrated to real dimensions. The GCPs based on GPS surveying can be derived to some candidate features clearly visible in both the scene and the resulting point cloud, proofed by [10]. In practice, it is easier to deploy complementary physical features with high contrast and clearly defined centroid around the target object.

During the image processing in this study, the light was sufficient and evenly illuminated on the surface of sample without causing reflections. Some regions close to or on the specimens were painted to textured surface in order to increase the recognition rate of common points between different images. A full-range image stream including more than 70 images from all angles of the specimen was used to establish one 3D point-cloud to ensure the accuracy. As the original point-cloud exported by SFM method is a mass point set with quite amounts of noise points, post-processing in CloudCompare is unavoidable to increase the quality of modelling. The workflow developed in this test as mentioned below was applied to all the point-clouds needed in the subsequent analyses. A noise filtration was carried out to remove the isolated points from the raw point-clouds and a transform from a relative size to real dimensions was undertaken on the basis of GCPs. The Poisson Surface Reconstruction algorithm proposed by Mish Kazhdan et al. [13] was applied to achieve new point-clouds with a specific point density and the original features of its source cloud (scalar fields, colors, normals, etc.). Fig.4.2 illustrates the evolution of this basic processing for the tufted preform in hemispherical forming. The processed point-cloud (Fig.4.2c) could reproduce the essential features of the sample (Fig.4.2a) and the noises (isolated points on the surface) in the raw point-cloud (Fig.4.2b) were effectively eliminated.

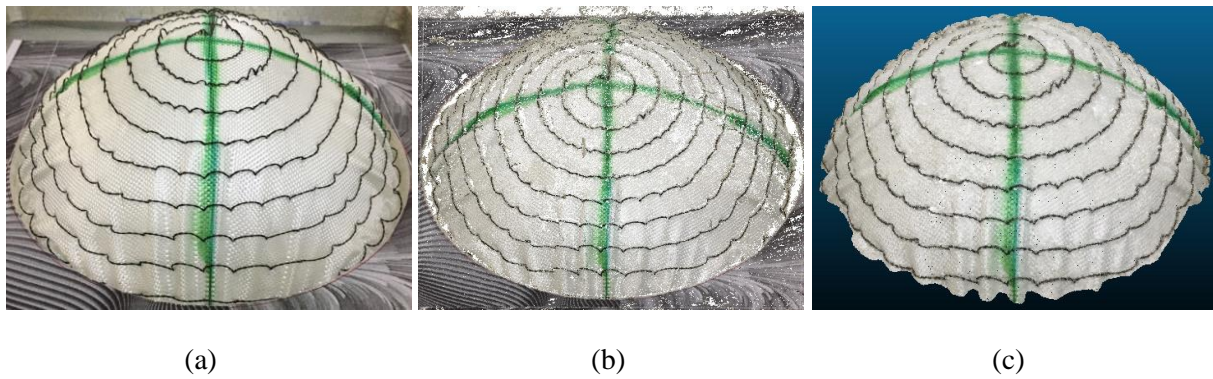


Figure 4.2 Example of modelling procedure, (a) photo of sample, (b) raw point-cloud, (c) processed point-cloud.

4.2.4 Wrinkling characterization

The idea of the examination of amplitude and position of wrinkles is to compute the deviation of the deformed fabric from an idealized shape. A textured fabric which is elastic and has almost the same thickness as the four-layer non-tufted sample ($0.5 \pm 0.02\text{mm}$) is selected to serve as the wrinkle-free benchmark. As every 3D reconstruction point-cloud has an independent coordinate system, it restricts a direct computation between the two different point clouds. Therefore, six GCPs attached to the forming device and maintaining in the same position during all the tests are used to match the two independent coordinate systems. The schematic (Fig.4.3a) illustrates the positions of the GCPs highlighted by the yellow circle. The intersection composed of two white lines with 0.5 mm thickness has been magnified on the right side of Fig.4.3a. Then, CloudCompare permits to compute the differences between two point-clouds on the basis of Hausdorff distance[14]. As illustrated in Fig.4.3b, to determine the nearest point in the reference cloud, it will locally model the reference cloud surface by fitting a mathematical model on the nearest existing point and several of its neighbours. Afterward, the distance from each point of the compared cloud to its nearest point in the reference cloud is transformed to the distance to this local model[15].

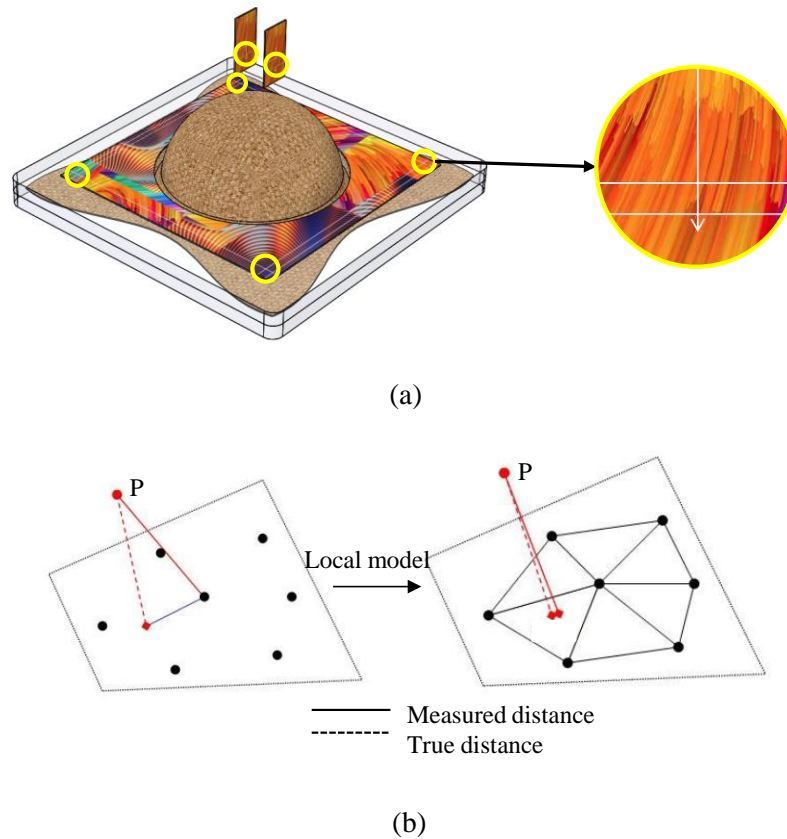


Figure 4.3 Schematic of modelling, (a) position and feature of ground control point (GCP) used in this test, (b) method of distance measurement between two point clouds [15].

The projection plot of wrinkling is then given through this method from the top view of the center which is the best degree of focus for hemispherical forming. The procedure is further illustrated in Fig.4.4 for the CDT sample, comparing the tufted model in (a), the wrinkle-free model in (b) and the resulting cloud-cloud distance model in (c). The location and height of the wrinkles are clearly highlighted in the cloud-cloud distance model with an active scalar field (Fig.4.4c). The regions in red correspond to the parts of tufted fabric further away from the reference fabric, and the regions in blue are closer to the reference fabric. The maximum value at the top of the colour scale is the maximum distance between two compared models. The warp and weft directions of the top layer correspond respectively to X and Y directions marked in the plots. As illustrated in Fig.4.4c, the spiral circles in the cloud-cloud distance model caused by the inserted tufting yarns could be mistakenly treated as some small-scale wrinkle features in statistical analysis. To reduce the influence of the tufting yarns,

a smoothed model retaining the original wrinkle features is regenerated by the Poisson Surface Reconstruction algorithm, showed in Fig.4.4d. Since the fluctuation on the model surface caused by the tufting yarns cannot be totally eliminated, a threshold procedure is implemented to further optimize the cloud-cloud distance model. It is a way to separate the point-cloud by turning all points whose height values are below a threshold to saturated blue, representing the wrinkle-free area, and converting all points whose values above another threshold to saturated red, representing the severe-wrinkle area. The determination of the threshold values is the major issue in the procedure. In this study, the lower threshold value is set to 1mm due to the technical accuracy limit. This threshold value can eliminate most small fluctuation and reproduce the essential features seen in the raw model. Furthermore, since the structure of the plain woven glass fabric used in this test is compact, the yarn bending defect should be small and rare. Few bending yarns appearing on the surface would not have an important effect on the statistical analysis of wrinkle ratio. As a result, the areas over 1 mm thickness could be considered to be wrinkles. The upper threshold value for the severe-wrinkle area in hemispherical forming is set to 4 mm. As the severe-wrinkle area identified by the 4 mm threshold value has been already quite small and almost equals to zero for certain samples, there is no need to discuss the threshold value higher than 4 mm. At the same time, 4 mm equals approximately to 0.6 times the maximum wrinkle height (about 7.3 mm) of all the samples in hemispherical forming. This upper threshold value has been changed to 3 mm in square-box forming, since the maximum wrinkle height is decreased to 5.7mm (about 0.6 times the maximum wrinkle height of 5.7 mm). The cloud-cloud distance model after the threshold procedure is showed in Fig.4.4e, with minor perturbations and noise on the surface. The color scales for the cloud-cloud distance have been modified to the same value in all subsequence plots, allowing a convenient comparison of these wrinkle patterns.

The severity of wrinkling can be then quantified by wrinkle ratio, which equals to the wrinkle area divided by the total sample area in the projection image. In order to increase the accuracy of measurement, the colorful wrinkle pattern images with a gradient from saturated red to saturated blue (Fig.4.4e) should be converted to binary images (Fig.4.4f). The grey and blue areas in the binary images represent respectively the wrinkle and wrinkle-free areas. All the measurements are taken in the binary images with a resolution of 400×400 pixels by ImageJ software. The same procedure is applied for the samples tested in square-box forming.

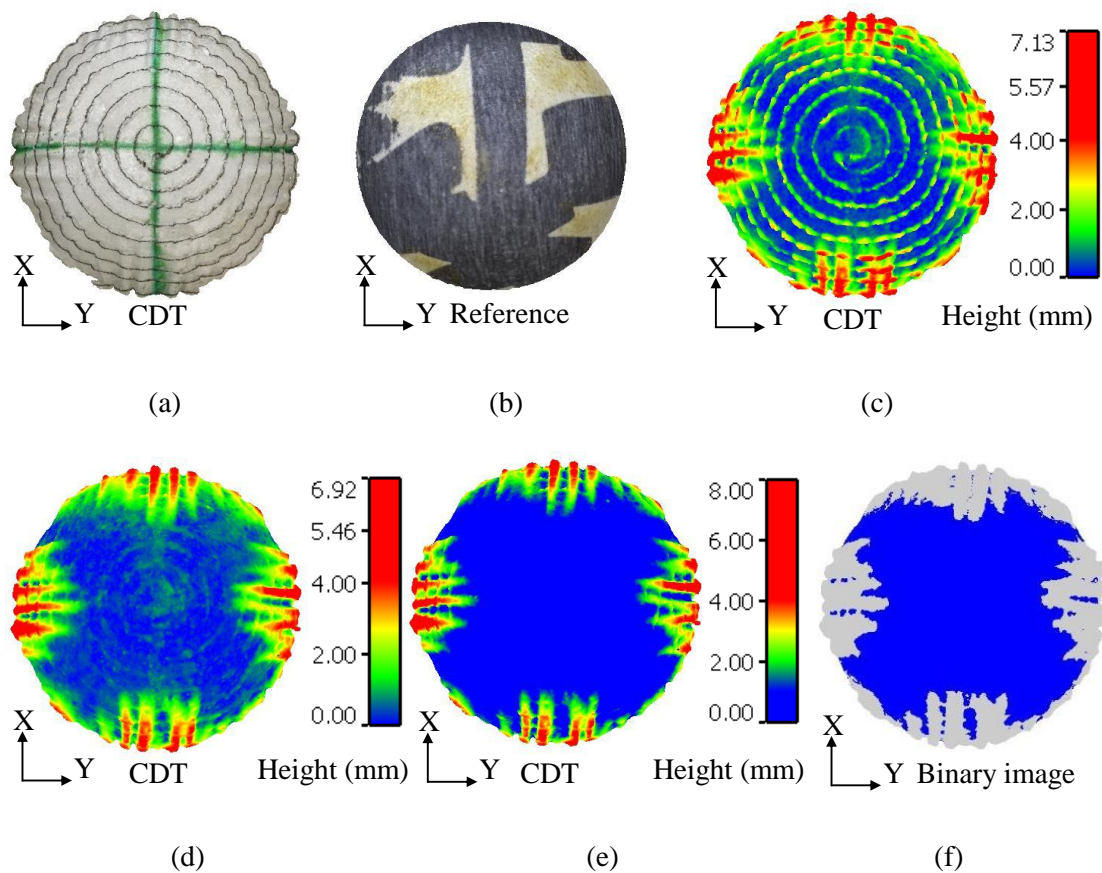


Figure 4.4 Example of wrinkle characterization methodology, showing the models from the top view of center in hemispherical forming and from the vertex extension line in square-box forming, the warp and weft directions of the top layer corresponding respectively the X and Y directions, (a) tufted sample model, (b) wrinkle-free sample model, (c) original wrinkle pattern, (d) wrinkle pattern without the tufting yarns, (e) wrinkle pattern after the threshold filtration, (f) binary wrinkle pattern.

The accuracy of this approach in such a composite forming process has been validated by comparing the 3D reconstruction model of the forming punch to its original CAD model. Cloudcompare can automatically fit the statistical distribution of point-clouds on the active scalar filed values by Normal distribution. Table 4.2 demonstrates the statistical data for both hemispherical and square-box shape. The mean distance between two compared models is only 0.10 mm and 0.14 mm for hemispherical and square-box shape respectively. According to the three-sigma rule, 99.7% of the values lie within 0-0.34 mm for hemispherical shape and 0-0.41 mm for square-box shape. Thus, a good agreement is considered to be achieved in these two cases. Furthermore, Fig.4.3c can confirm that the established fabric model reflects an appropriate set of wrinkling features observed in the photo (Fig. 4.3a).

Table 4.2 Statistical data of normal distribution.

	Mean	Standard deviation	Coverage	Maximum deviation
Hemispherical	0.10 mm	0.08 mm	0-0.34 mm	0.84 mm
Square-box	0.14 mm	0.09 mm	0-0.41 mm	0.91 mm

4.3. Results and discussion

The deformed preforms after the hemispherical and square-box forming processes are shown in Figs.4.5 and 4.6. It can be noted that the shapes of tufted preforms depend strongly on the tufting patterns. The different layer orientation and the effect of the tufting yarns in the different zone is the main reason for the occurrence of the different material draw-in, inter-layer sliding and wrinkling phenomena. In particular, wrinkling, as the most common forming defects experienced frequently in the textile composites forming, needs to be well quantified.

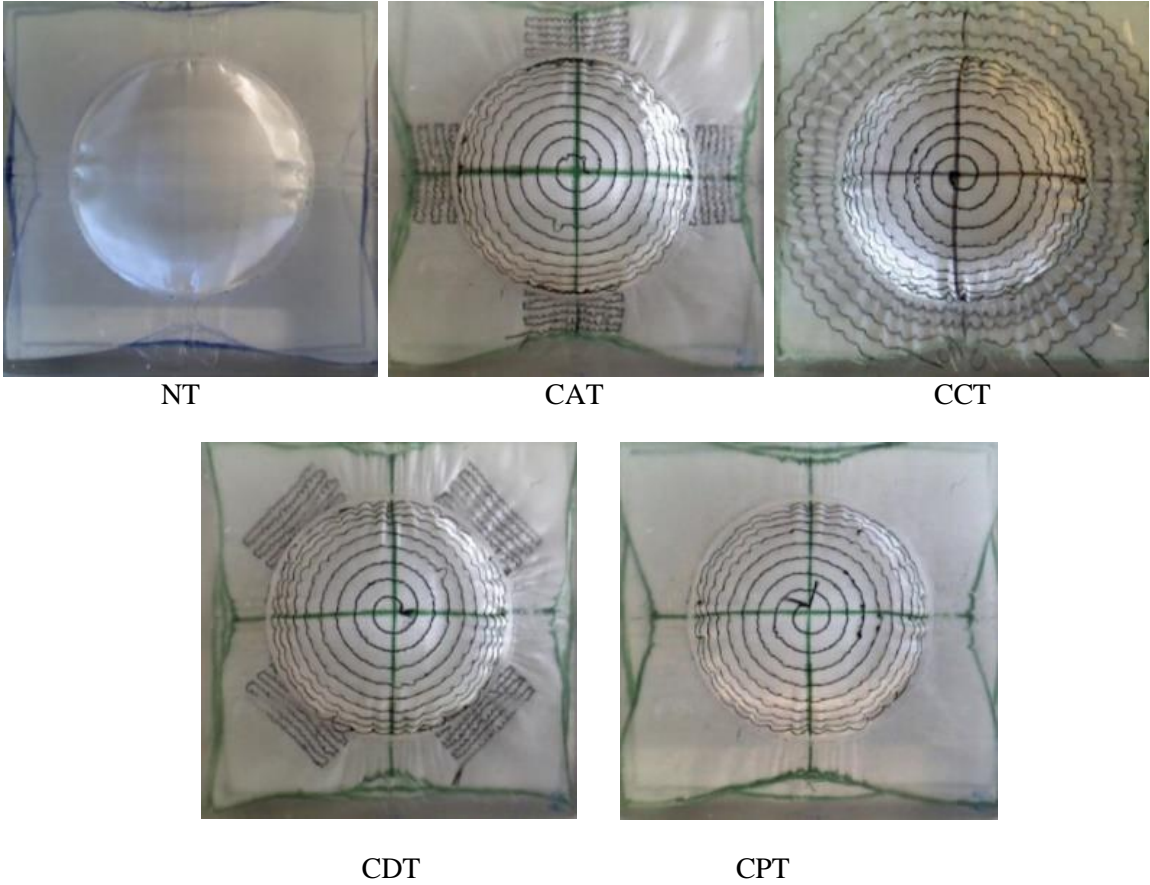


Figure 4.5 The deformed preforms after the hemispherical forming.

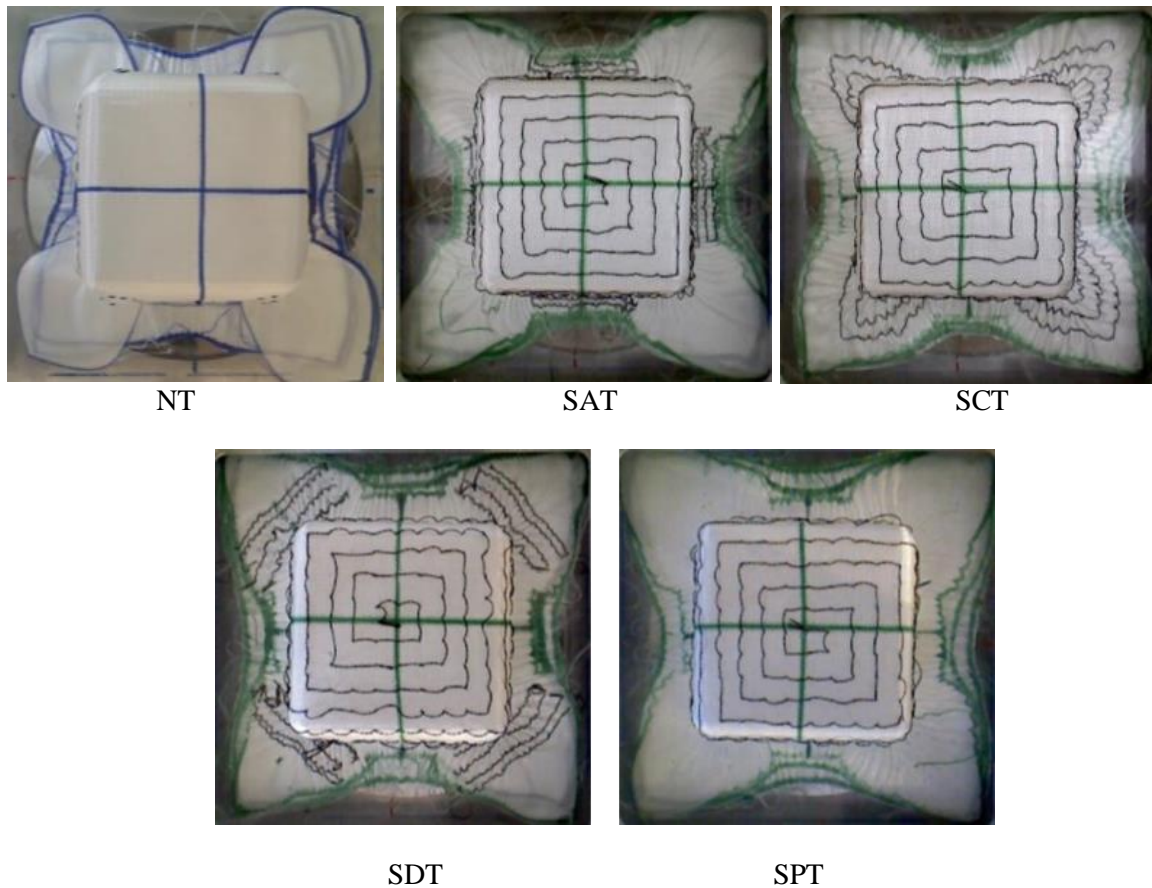


Figure 4.6 The deformed preforms after the square-box forming.

4.3.1 *Wrinkle patterns*

The wrinkling patterns provide useful information for validation studies and helpful clues to find the strategies to avoid this defect. Figs.4.7a-4.7e show the contour plots, for the five samples, of the wrinkling patterns from the top view during hemispherical forming. Recall that the X/Y directions correspond respectively to the weft and warp directions of the top layer of the samples. The color scales for wrinkles height keep the same in all the plots to allow the comparison between different samples. The examination of measurement error associated with the subsequent results is given by three repeatability tests.

A general trend for the distribution of wrinkles in all cases is that most significant wrinkles appear at the circumferential edges and no wrinkles can be observed in the center areas. The relatively small changes in the shape of the preforms can be accommodated by

shear deformation in these center areas. However, the resistance to the deformation of each fabric layer in the preform caused by tufting or interlayer friction limits such shearing effect at the circumferential edge, leading to the appearance of wrinkles. Moreover, the wrinkle severity in horizontal and vertical directions is normally higher than that in diagonal directions for the cases of CCT, CDT, CPT and NT, Figs.4.7b-4.7e. The exception to this is the result of CAT, where the wrinkle severity in horizontal and vertical directions is lower than diagonal directions, showed in Fig.4.7a. For $0^\circ/90^\circ$ layers of samples, the horizontal and vertical directions are the locations where the tows run in the radial directions so that the fabric cannot accommodate the required reduction in the peripheral length and wrinkles appear in these locations. For $\pm 45^\circ$ layers, the shear deformation leads to elongation of fabric in these horizontal and vertical directions, therefore the draw-in of tows and wrinkling area is rotated to diagonal directions. However, it seems that the $0^\circ/90^\circ$ layers play a predominant role in most wrinkling forming results compared with $\pm 45^\circ$ layers, even if in the homogeneous tufting (Figs.4.7b and 4.7d) and non-tufting (Fig. 4.7e) cases. It might be caused by the relative longer tow length of the $0^\circ/90^\circ$ layers on the circumference. By the comparison of the first three samples (Figs.4.7 a, b and c), it can be concluded that wrinkling can be effectively weakened in the directions where the tufting yarns occur and obviously be reinforced in the remaining directions. Specifically, when the all direction tufting pattern is applied (Fig.4.9b), the wrinkles can be weakened in all directions and distributed more evenly.

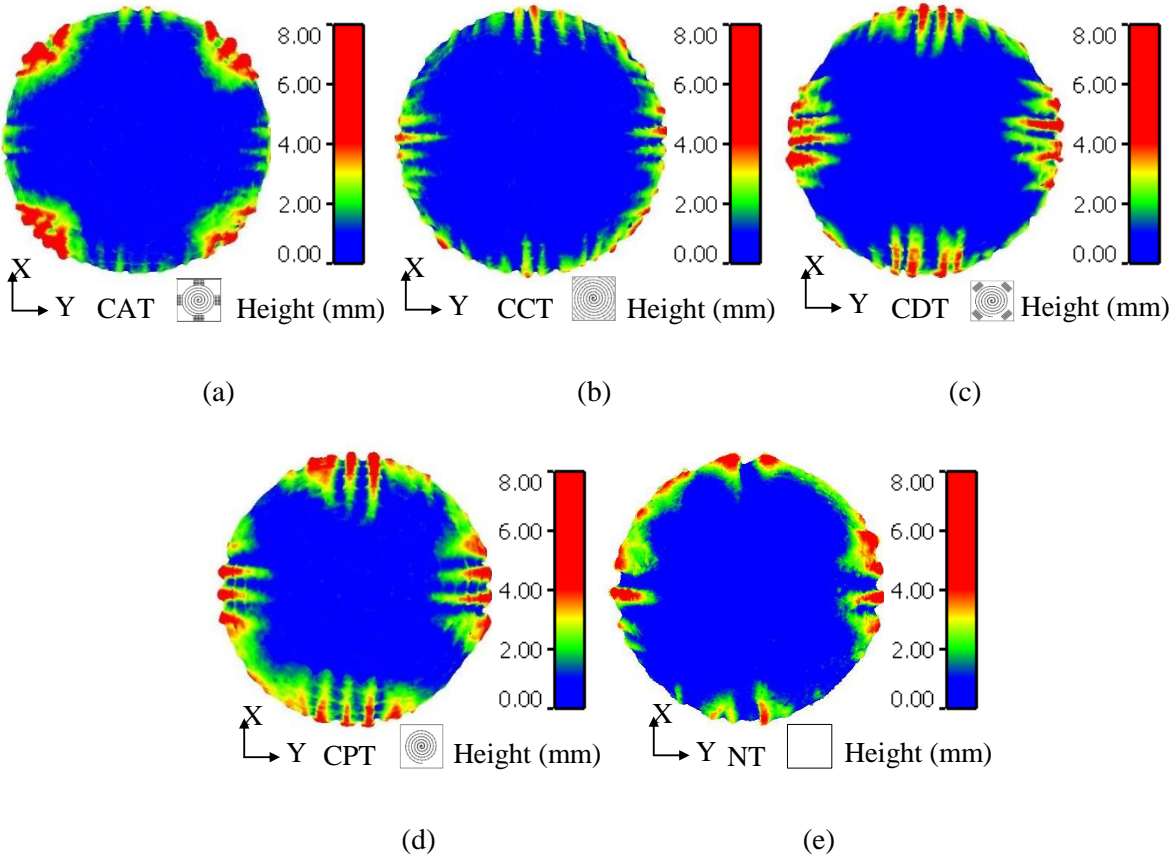


Figure 4.7 Wrinkle patterns for the different test samples in hemispherical forming.

The wrinkle patterns of the five samples in the square-box forming are illustrated in Figs.4.8a-4.8e. As the wrinkles on the four sides cannot be observed from the top view, the projection angle is changed to be on the vertex extension line for the wrinkle pattern plot. The height color scale bars have been adjusted to emphasize the patterns in this forming, where the saturated red color begins from 3 mm and the saturated blue color stops at 1 mm. As a whole, no wrinkles can be observed on the upper surface due to the very weak deformation of fabric in this area. Different large deformation of each layer which cannot be accommodated by the in-plane shearing effects results in a mass of wrinkles occurring on the four lateral surfaces. Meanwhile, some intensive wrinkles with small amplitude appear at the corners, contributing to the strong shearing effects. For homogeneous tufting patterns, shown in Figs. 4.8b and 4.8d, the severe wrinkle zone marked in red colour can be seen both on lateral surfaces and corners. In the case of SAT sample (Fig.4.8a), the wrinkles on the lateral

surfaces are slightly suppressed corresponding to the relatively small red areas, while the wrinkles at the corners still remain severe. On the contrary, it seems that no apparent reduction of wrinkle magnitude at the corners can be observed using the SDT sample. It hints that the tufting location only has a slight effect on wrinkling in square-box forming, as the constraint from tufting is quite small compared to the other membrane stresses in such a deep drawing process. For the non-tufting sample, shown in Fig.4.10e, the size of wrinkles is relatively large on the lateral surfaces, as no restriction from the tufting yarns is imposed through-the-thickness.

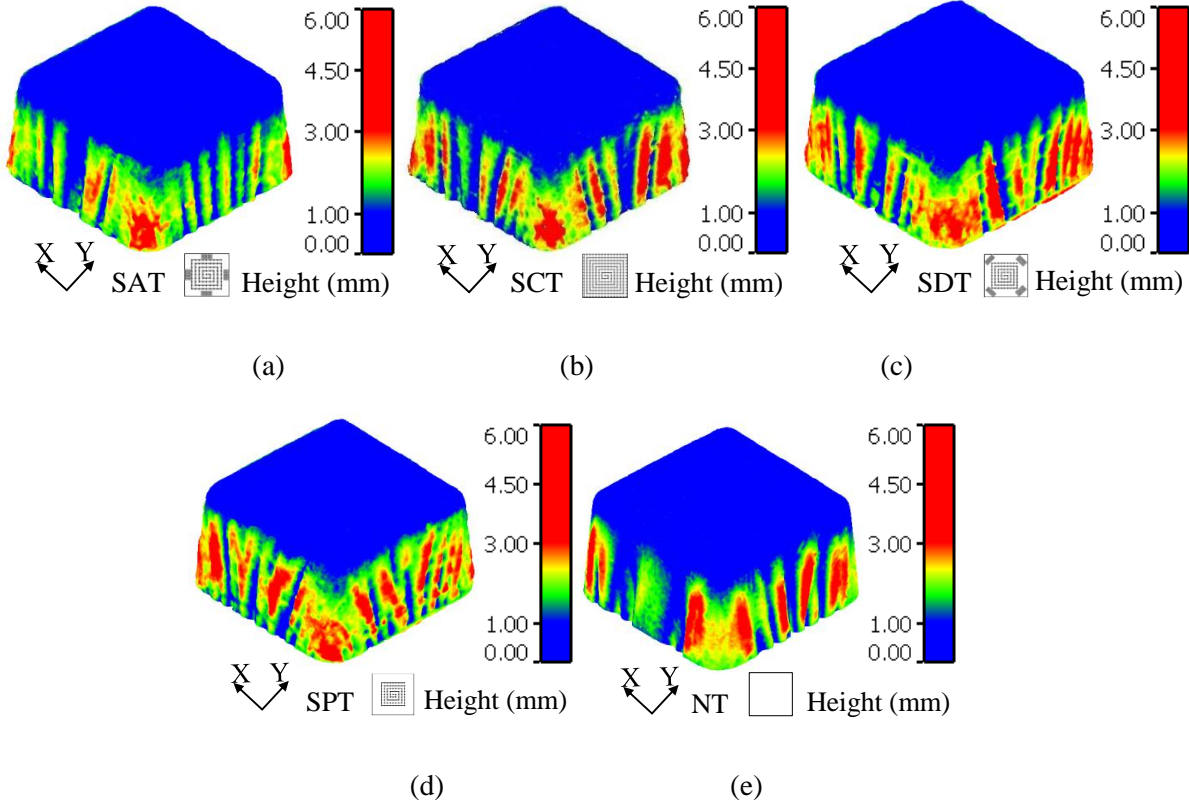


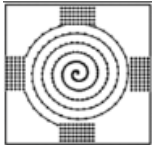
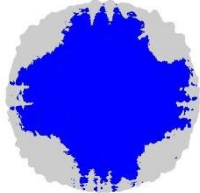
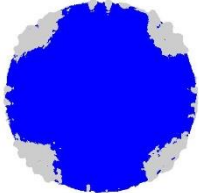
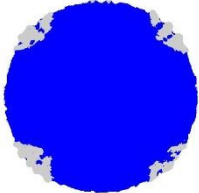
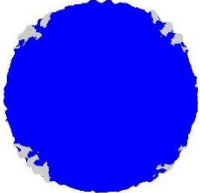
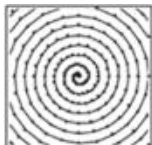
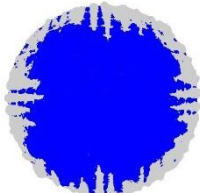
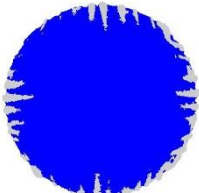
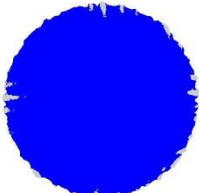
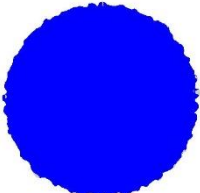
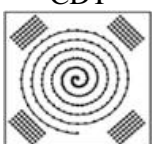
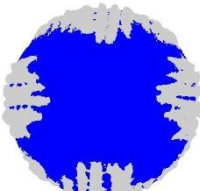
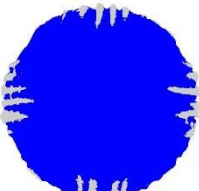
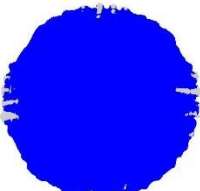
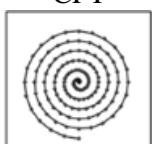
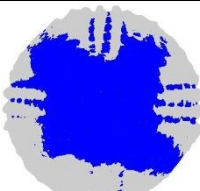
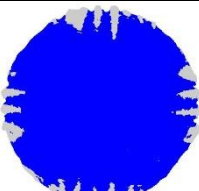
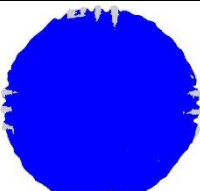
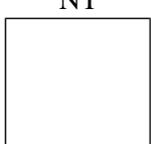
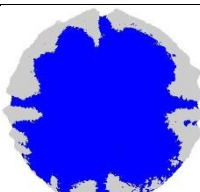
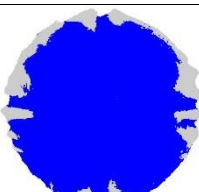
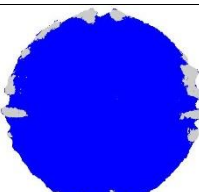
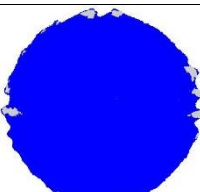
Figure 4.8 Wrinkle patterns for the different test samples in square-box forming.

4.3.2 *Wrinkle ratio*

In order to confirm the observation of the effect of tufting locations on wrinkling inferred above, the wrinkle severity is evaluated by wrinkle ratio. Table 4.3 shows the binary images of wrinkle patterns with the increasing threshold for different samples in hemispherical forming. Meanwhile, the mean wrinkle ratio and the coefficient of variations (CV) of each sample from three repeatability tests are also indicated. The highest variation of wrinkle ratio is seen in the CCT sample with a 4 mm threshold value by 9.8% and the lowest variation is in the CDT sample with a 1 mm threshold value which varies by 4.1%. The variations are considered to be weak, as all the values are under 10%.

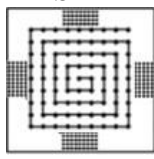
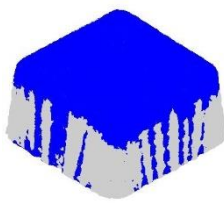
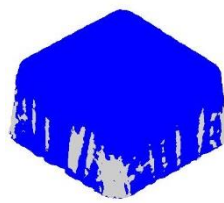
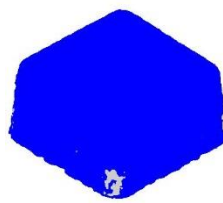
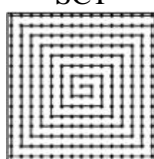
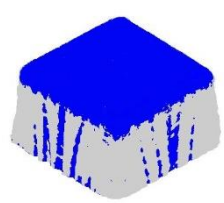
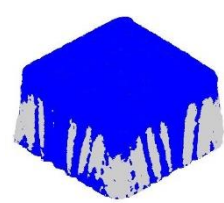
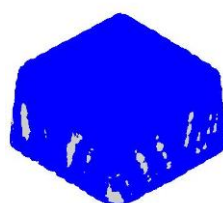
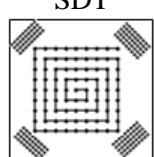
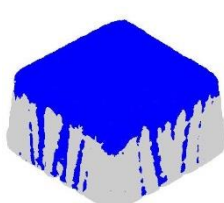
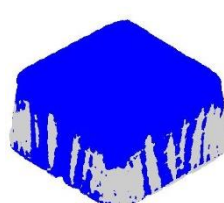
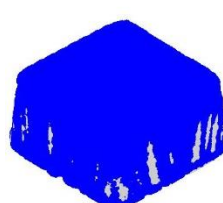
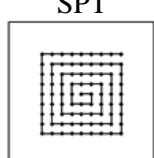
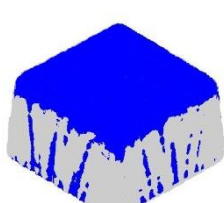
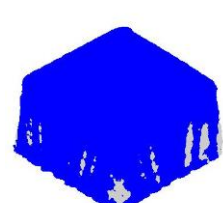
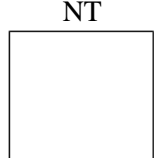
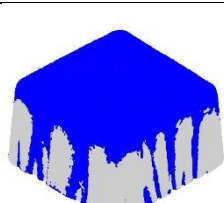
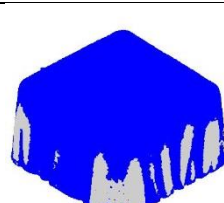
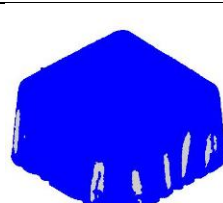
From the observation in the horizontal rows, the wrinkle ratio of each sample always tends to be lower following the rise of the threshold value, as more areas are treated as wrinkle-free areas contributed to the thresholding filtration. On the other hand, in the comparison of the columns, when the threshold value equals to 1 mm, the CCT sample has the smallest wrinkle ratio among the five samples which can be considered to be consistent with the observation mentioned in the previous section. The CPT sample offers the highest wrinkle ratio, caused by the relatively weak tension in the peripheral zone. When the fluctuation of wrinkles passes over 4 mm, these wrinkles are defined as severe wrinkles and their ratio is illustrated in the last column in the Table 4.3. The CCT sample still remains its best ability to control the wrinkling by presenting the lowest values. However, a relatively high value can be seen in the CAT sample, as the wrinkles appearing in diagonal directions derive mainly from the deformation of the inner layers (layers with $\pm 45^\circ$ orientations). At the same time, the NT sample also has a relatively high value compared to others, as there are more voids between layers due to the lack of the through-the-thickness reinforcement in the preform.

Table 4.3 Binary wrinkle images with different thresholds in hemispherical forming (The threshold values are shown in the first row of the table)

	T=1 mm	T=2 mm	T=3 mm	T=4 mm
CAT 				
Wrinkle ratio (%)	25.4	16.4	7.2	3.1
CV (%)	4.5	6.7	8.4	9.1
CCT 				
Wrinkle ratio (%)	20.3	8.5	2.3	0.5
CV (%)	4.3	5.6	5.8	9.8
CDT 				
Wrinkle ratio (%)	32.1	16.3	7.4	2.1
CV (%)	4.1	5.9	6.9	7.4
CPT 				
Wrinkle ratio (%)	37.4	21.3	9.6	2.2
CV (%)	5.6	5.5	6.0	7.3
NT 				
Wrinkle ratio (%)	27.6	15.0	7.1	3.0
CV (%)	5.7	5.5	7.7	8.4

In the square-box forming (Table 4.4), three threshold values are used to illustrate the evolution of wrinkling, as the severe wrinkle height is determined to 3mm. Again, no variations exceed 10% and the maximum value can be seen in the NT sample by 7.8% when the threshold equals to 2 mm. The wrinkle ratio is reduced for each sample following the increasing threshold values. In the first column, the SAT sample is proved to have the most insignificant wrinkling owing to its smallest wrinkle ratio. Moreover, the relatively smooth fluctuation of the fabric caused by the lack of tufting yarns leads to less wrinkle number and larger wrinkle size in the NT sample, having a minor wrinkle ratio. When the threshold grows up to 3mm, the SAT sample, owning some small wrinkle areas at the corners and no wrinkles on the four lateral surfaces, presents a more dominant advantage in terms of the severe wrinkle ratio compared to the others. On the contrary, in the comparison of the NT sample having a relatively slight wrinkling at the corners, the wrinkle magnitude of tufted samples always maintains severe. It can be explained that the surface of the tufted samples is extended away from the reference fabric at the corners owing to a large number of loops of tufting yarns stacked up between the bottom layer of the fabric and the punch.

Table 4.4 Binary wrinkle images with different thresholds in square-box forming (The threshold values are shown in the first row of the table)

	T=1 mm	T=2 mm	T=3 mm
SAT 			
Wrinkle ratio (%)	32.3	11.4	1.5
CV (%)	3.4	4.2	5.4
SCT 			
Wrinkle ratio (%)	42.1	22.8	4.3
CV (%)	2.3	4.1	5.0
SDT 			
Wrinkle ratio (%)	40.9	22.5	5.1
CV (%)	3.1	3.9	4.9
SPT 			
Wrinkle ratio (%)	43.2	24.3	5.4
CV (%)	2.6	4.4	7.3
NT 			
Wrinkle ratio (%)	35.8	16.4	4.4
CoV (%)	6.9	7.8	6.7

4.3.3 Wrinkle-free height and maximum wrinkle amplitude

Another two indicators, identified as wrinkle-free height and maximum wrinkle amplitude, are also used to characterize the wrinkling. The wrinkle-free height representing the size of an effective zone without wrinkles after forming, noted as Δh , is shown in Figs.4.9a and 4.9b. Larger wrinkle-free height value corresponds to smaller wrinkle severity. With the help of the CloudCompare software, the wrinkle-free height value can be measured easily by calculating the coordinate difference in the vertical direction of two selected points in the model. On the other hand, the maximum wrinkle amplitude is extracted on a wrinkle contour obtained in a cross-section with a height of 10 mm from the model bottom, marked by a violet dot line in Figs.4.9a and 4.9b. This height of this cross-section is chosen as typical of the location where significant wrinkling deformation occurs. Figs.4.9c and 4.9d illustrate the top view of the wrinkle contours obtained from the cross-section in hemispherical and square-box forming respectively. The flexural colourful line in the Figs.4.9c and 4.9d is the contour of tufted sample and the inner smooth grey line represents the profile of the wrinkle-free reference sample. Thus, the maximum wrinkle amplitude in hemispherical forming can be considered to be the maximum distance between the peaks of the wrinkles and the profile of the reference sample, highlighted by the dotted line in Fig.4.9c. On the other hand, since the reference fabric cannot totally attach to the lower half of the punch (as illustrated in Fig.4.9b, the gap exists between the reference fabric and the punch), the wrinkled surface of the tufted sample could fluctuate on both sides of the reference surface. The wrinkle amplitude is switched to the maximum peak-to-trough distance of the wrinkles, marked by two-dot lines in Fig.4.9d. Most measurements are taken in $0^\circ/90^\circ/180^\circ/270^\circ$ directions showing significant fluctuations for both forming, except for the CAT sample owning severe wrinkles in $45^\circ/135^\circ/225^\circ/315^\circ$ directions. Finally, the maximum wrinkle amplitude is the mean value of the four directions, due to the quasi-symmetry deformations.

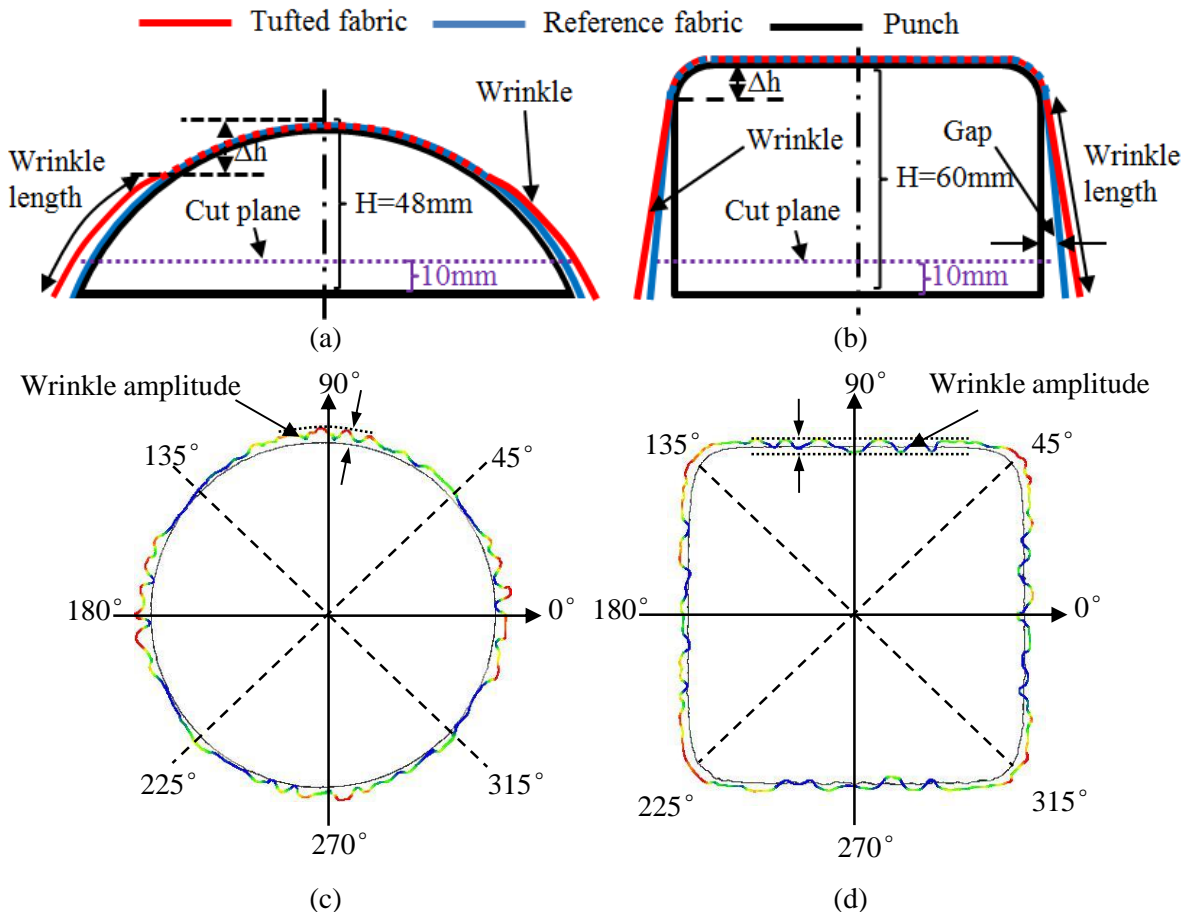


Figure 4.9 Schematic of the measurement position for wrinkle-free height (Δh) and wrinkle amplitude, front section view of hemispherical forming (a), front section view of square-box forming (b), top section view of hemispherical forming (c), top section view of square-box forming (d)

The measurement data of wrinkle-free height for each sample in hemispherical and square-box forming are respectively illustrated in Figs.4.10a and 4.10b. It can be indicated that, in Fig.4.10a, the CDT and CPT samples have relatively small wrinkle-free height values, as the wrinkle length spreading in $0^\circ/90^\circ/180^\circ/270^\circ$ directions can be raised by the inserted tufting yarns. On the other hand, due to the suppression of wrinkle length in $0^\circ/90^\circ/180^\circ/270^\circ$ directions, the CAT and CCT samples show relatively large wrinkle-free height values. In the square-box forming results, shown in Fig.4.10b, all the wrinkle-free height values are close to each other, as the wrinkles of each sample on the four lateral surfaces always spread from the bottom to the top. In both forming, the tufted samples cannot show an apparent advantage in the measurement of wrinkle-free height compared to the NT sample. The results reflect that the inserted tufting yarn can only increase or maintain the wrinkle length during forming.

Figs.4.10c and 4.10d show the comparison of the maximum wrinkle amplitude for each sample in both forming. It can be observed that the CCT and SAT present the smallest wrinkle amplitude, achieving a good relevance to the results of the wrinkle ratio discussed previously. Furthermore, in hemispherical forming, shown in Fig.4.10c, the CAT and CDT samples with the relatively large values are contributed to the forming balance broken by the tufting yarns from the specific directions.

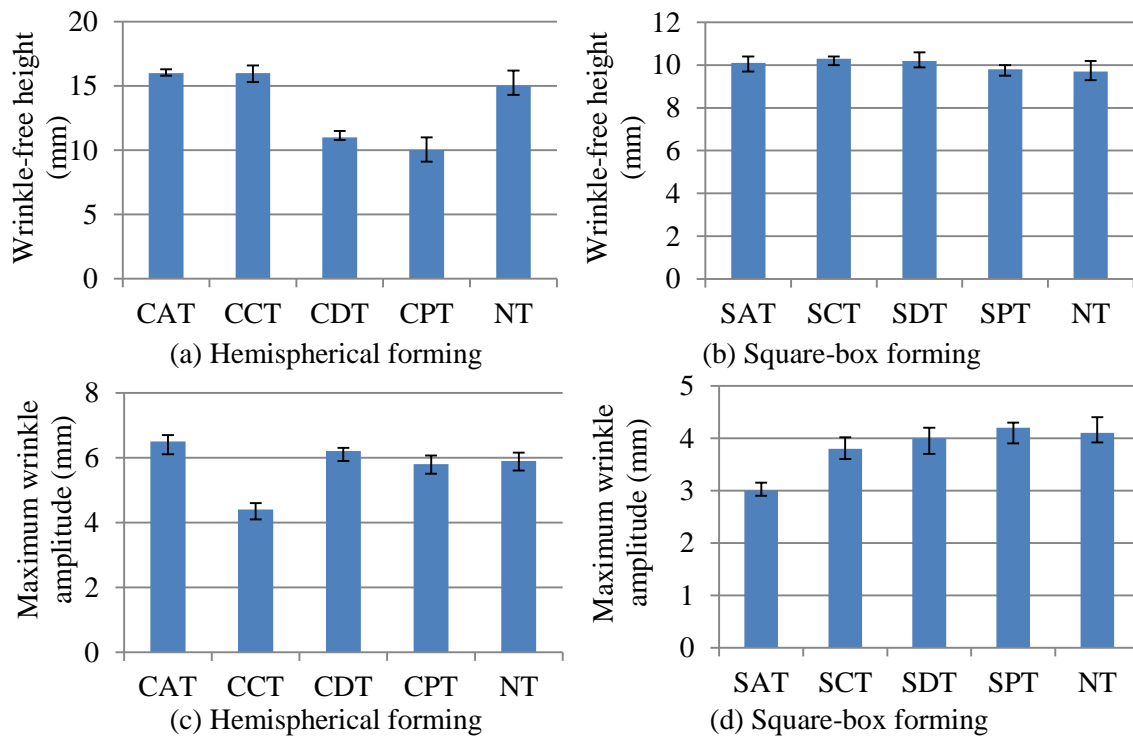


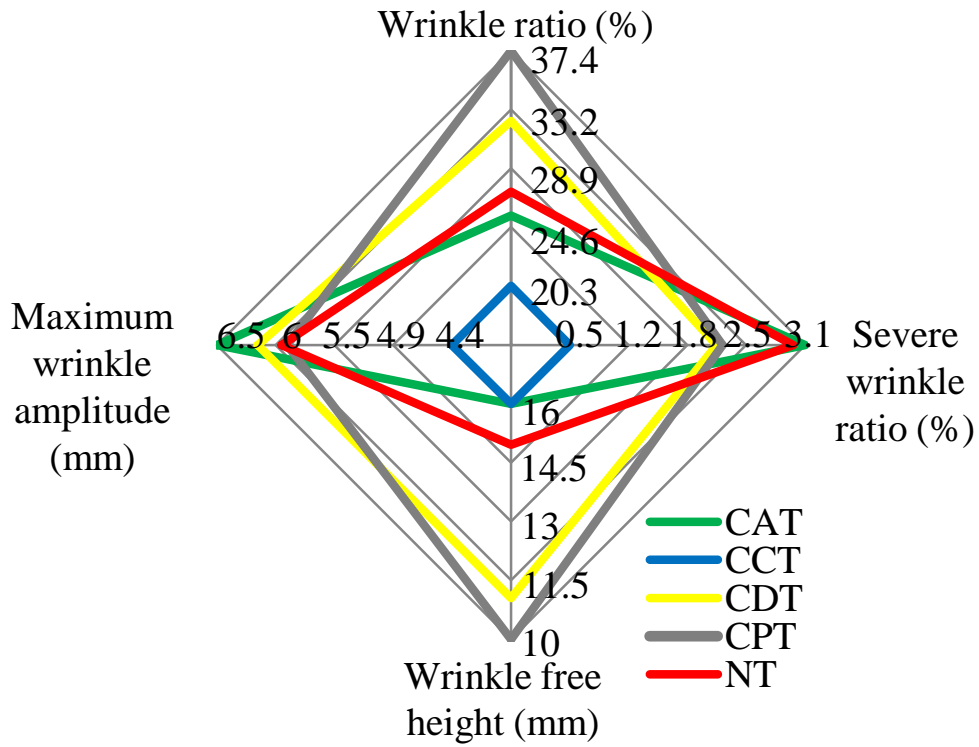
Figure 4.10 Influence of tufting location on the measurements of wrinkle-free height and maximum wrinkle amplitude.

4.3.4 Evaluation of wrinkling

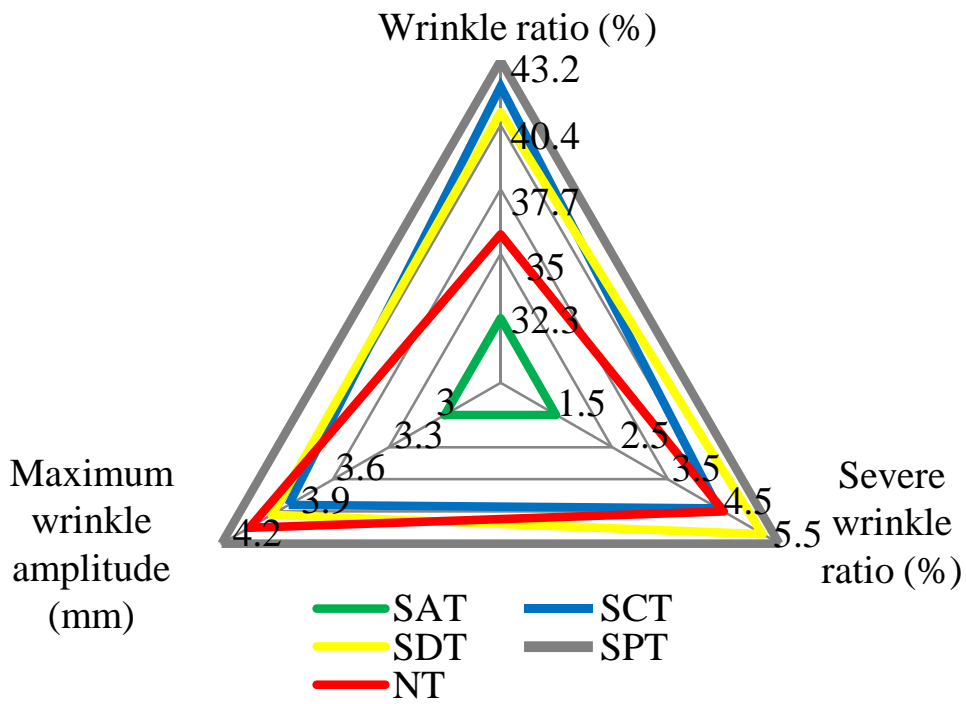
The wrinkling can be characterized by the different indicators as discussed above and there is to some extent consistency among these indicators. On the other hand, some slight deviations can still be seen in the description of wrinkle severity using these different indicators. In order to have a better understanding and a more global characterization of wrinkling, radar charts are plotted to demonstrate the differences between these indicators. In the hemispherical forming, as shown in Fig.4.11a, four main indicators (wrinkle ratio, severe

wrinkle ratio, wrinkle-free height and maximum wrinkle height) have been chosen as the parameters in the plot. However, in the square-box forming, the wrinkle-free height has been removed from the plot, as the value of each sample always maintains similar and the value difference is smaller than the measurement deviation. The axes are aligned with the most beneficial values to the inside of the figure, meaning that smaller swept out areas represent the sample with smaller wrinkle severity.

It can be observed that the CCT (blue line in Fig.4.11a) and SAT (green line in Fig.4.11b) samples cover the smallest areas in hemispherical and square-box forming respectively. A good consistency among different indicators is achieved in the wrinkling evaluation of these two samples. The respective loss in wrinkle severity in two different forming suggests that the tufting location in the peripheral zone should be linked to the punch shape in the way, in which the tufting distribution needs to follow the punch contour. Furthermore, it seems that the CPT and SPT samples marked by grey line sweep relatively large areas in both cases, implying that the way only tufted in center zone is not suitable for eliminating the wrinkling. On the contrary, the tufting yarns appearing in the peripheral zone would promote the friction between the fabric and the tools, so that more tension is introduced and applied during forming leading to minor wrinkling on the surface. The NT samples highlighted by the red line presenting a hybrid area with the others hint that the selection of tufting location is so important that inappropriate tufting pattern would result in a larger wrinkle severity to some extent.



(a)



(b)

Figure 4.11 Summary of different wrinkling indicators, (a) hemispherical forming, (b) square-box forming

4.4. Conclusion

In this chapter, a new numerical method based on SFM technique is applied to characterize and evaluate the wrinkling phenomenon on the surface of a double-curved shape. The relatively stable results demonstrate that the measurements based on this method can be used for the quantitative analyses. The experimental results illustrated that the wrinkling distribution depends critically on the tufting distribution in the peripheral zone. The wrinkling area and amplitude can also be effectively weakened using the appropriate tufting pattern, especially in the hemispherical forming case. By comparing the different wrinkling indicator values, it can be concluded that the tufting distribution following the contour of the punch shape in the peripheral zone can minimize wrinkles in the useful zone, but not be able to eliminate them totally.

For the perspectives, the characterization of wrinkling based on the numerical analysis should be improved further from two aspects: one is to increase the measurement accuracy and the other one is to find more effective evaluation indicators. On the other hand, as the shear deformation plays an important role in the forming process, the investigations about the effect of inserted tufting yarns on the shear property of fabrics are quite necessary and help to establish the numerical modelling/simulation in the future, which is also the work described in the next chapter.

4.5. References

- [1] Lee JS, Hong SJ, Yu W-R, Kang TJ. The effect of blank holder force on the stamp forming behavior of non-crimp fabric with a chain stitch. *Compos Sci Technol* 2007;67:357–66.
- [2] Domskienė J, Strazdienė E, Bekampienė P. Development and optimisation of image analysis technique for fabric buckling evaluation. *Int J Cloth Sci Technol* 2011;23:329–40.
- [3] Christ M, Miene A, Moerschel U. Characterization of the drapability of reinforcement fabrics by means of an automated tester. *Proc. SPE Automot. Compos. Conf. Exhib.*, vol. 12, 2012.
- [4] Arnold SE, Sutcliffe MPF, Oram WLA. Composites: Part A Experimental measurement of wrinkle formation during draping of non-crimp fabric. *Compos PART A* 2016;82:159–69. doi:10.1016/j.compositesa.2015.12.011.
- [5] Wu C. Towards linear-time incremental structure from motion. 2013 *Int. Conf. 3D Vision-3DV 2013*, IEEE; 2013, p. 127–34.
- [6] Wu C, Agarwal S, Curless B, Seitz SM. Multicore bundle adjustment. *CVPR 2011*, IEEE; 2011, p. 3057–64.
- [7] Wu C. A GPU implementation of scale invariant feature transform (SIFT). [Http://www.Cs.Unc.Edu/~Ccwu/siftgpu/](http://www.Cs.Unc.Edu/~Ccwu/siftgpu/) 2007.
- [8] Snavely KN. Scene Reconstruction and Visualization from Internet Photo Collections 2008.
- [9] Lowe DG. Distinctive Image Features from Scale-Invariant Keypoints 2004;60:91–110.
- [10] Murat-błażejewska S. Ground volume assessment using 'Structure from Motion' photogrammetry with a smartphone and a compact camera 2017:281–94. doi:10.1515/geo-2017-0023.
- [11] Westoby MJ, Brasington J, Glasser NF, Hambrey MJ, Reynolds JM. Geomorphology “Structure-from-Motion” photogrammetry: A low-cost, effective tool for geoscience applications 2012;179:300–14. doi:10.1016/j.geomorph.2012.08.021.
- [12] Barazzetti L, Binda L, Scaioni M, Taranto P. Photogrammetric survey of complex geometries with low-cost software: Application to the ‘G1 temple in Myson, Vietnam. *J Cult Herit* 2011;12:253–62. doi:10.1016/j.culher.2010.12.004.
- [13] Kazhdan M, Bolitho M, Hoppe H. Poisson Surface Reconstruction 2006.
- [14] Aspert N, Santa-Cruz D, Ebrahimi T. Mesh: Measuring errors between surfaces using the hausdorff distance. *Proceedings. IEEE Int. Conf. Multimed. Expo*, vol. 1, IEEE; 2002, p. 705–8.
- [15] CloudCompare user manual n.d. *Cloud Compare v2.6.1 - User manual.pdf*.pdf.

5. Experimental analysis on the in-plane shear properties during the forming of the tufted carbon woven fabrics

5.1. Introduction

The effect of tufting on the forming defects, especially on the wrinkling phenomenon, has been presented in the previous chapters. As we known, during the forming process, the woven fabrics made of two initially orthogonal sets of yarns (warp and weft) are deformed to adapt the double-curved surface. The high resistance to extension in yarn directions of woven fabric contributes to a result that the in-plane shear of the textile reinforcement mainly accounts for this spatial deformation. In-plane shear can increase the deformation efficiency, but can also lead to a fiber reorientation[1–4] and a variation of shear angles inside fabrics. The textile reinforcements generally have a limit to the shear angle. If the fabric tows rotate beyond this limit, wrinkling, which significantly degrades the mechanical and aesthetic properties of the final product, will probably occur [5–7]. This limit called ‘locking angle’ is strongly dependent on textile reinforcement structure. At the same time, the variation of shear angles can also influence the fabric permeability during the resin infusion process [8,9]. Several papers have investigated the mechanical performance of the tufted composites, but they are limited to the evaluation of the compression-after-impact (CAI) and in-plane tensile properties of the cured composites [10,11]. There are no published papers relating to the tufting effect on the in-plane shear property of dry fabrics, which is considered to be necessary for the prediction of the tufted fabric forming process.

Picture frame test and Bias-extension test are the two main approaches used to measure shear property for the textile reinforcement. The picture frame test has a uniform shear deformation of the entire specimen, but the test value can be significantly interfered due to the misalignment of tows in the specimen [12–15]. In contrast, the bias-extension test is relatively insensitive to the misalignment of tows, but the non-uniform deformation across the test specimen increases the difficulty to obtain the actual shear behavior from the raw test data. In

this study, the bias-extension test is used, as it is considered to be a relatively simple test without sophisticated instrumental compared to the picture frame test.

The objective of this chapter is to investigate the tufting effects on the in-plane shear property of dry reinforcement through the bias extension test. In particular, the effects of in-plane tufting directions, tufting density and tufting yarn fineness are mainly focused. The deformation mechanisms at the scale of the tufting yarns also have been shown.

5.2. Materials and methods

5.2.1 Materials

The materials used in this study are provided by HexForce® and Tenax®, which specialize in producing a range of globally certified aerospace/industrial products. Further details of the materials present as follows:

- G0926 D 1304 (HexForce®): A carbon 5H satin weave fabric has 375 g/m² area weight (4.6 yarns/cm, 4.6 picks/cm) with a thickness of 0.38 mm.
- HTA40 (Tenax®): A 67 Tex twisted carbon filament yarn with a tensile strength of 4100 MPa is used as a tufting thread.

5.2.2 Bias-extension test

The bias-extension test is a tensile test applied on the rectangular specimen with the warp and weft directions of the tows orientated initially at $\pm 45^\circ$ to the direction of the tensile load. During the preparation of specimens, the fibre yarns should be cut carefully to be oriented $\pm 45^\circ$ to the rectangular edges. Any small misalignment will generate extra tensile or compressive forces in the fibres, which can lead to a large scatter in the force measurement. A rotary cutter was used for cutting the specimens in this study, to avoid the fibre slippage and

local pull-out as much as possible. The length of the specimen (excluding the gripper regions) is typically larger than twice its width to obtain a suitable ‘pure shear’ zone in the centre. At the same time, an appropriate length of fabric should be left for clamping to ensure no slippage between the tows of the specimen and the gripper during the test. A force detector linked to the upper jaw permits to record the force of deformation and a constant displacement is applied on the specimens during the tests. The force-displacement data are collected for post-processing and analysing.

For analyzing the bias extension test results, two important relations are necessary to be established. A kinematic relation is to link the in-plane shear angle to the extension of the specimen[10,12–14] and a mechanical relation relates the shear stress in the fabric to the measured force on the tensile machine[10,12,13,26]. These two relations need three basic assumptions as follows: yarns in the fabric are inextensible; no slippage between warp and weft yarns at the cross-over points occurs; bending stiffness of fabric yarn is neglected [10].

Fig.1a shows the kinematic relation in the fabric, when the specimen is stretched from L to $L + \delta$, the surface of the specimen presents three different shear states, called ‘non-deformed’, ‘half shear’ and ‘pure shear’ respectively. For the ‘non-deformed’ zone, marked as zone A, the warp and weft yarns have both a clamped end impeding their deformation. For the ‘pure shear’ zone, also called zone C, both the warp and weft yarns have free ends. If the sliding of yarns at crossovers is neglected, the pure shear angle γ in zone C can be calculated theoretically using Equation (1) [10,12–14] based on the stretching distance δ and $L=H-W$. H and W represent the original height and width of the specimen, respectively. Furthermore, the zone B (‘half shear’ zone) presents a half shear angle value compared to zone C, as one yarn direction has its clamped end, but the other direction is free.

$$\gamma = \frac{\pi}{2} - 2 \cos^{-1}\left(\frac{L+\delta}{\sqrt{2} \times L}\right) \tag{1}$$

where γ is the shear angle and equals to $\frac{\pi}{2} - \theta$, as shown in Fig.5.1a.

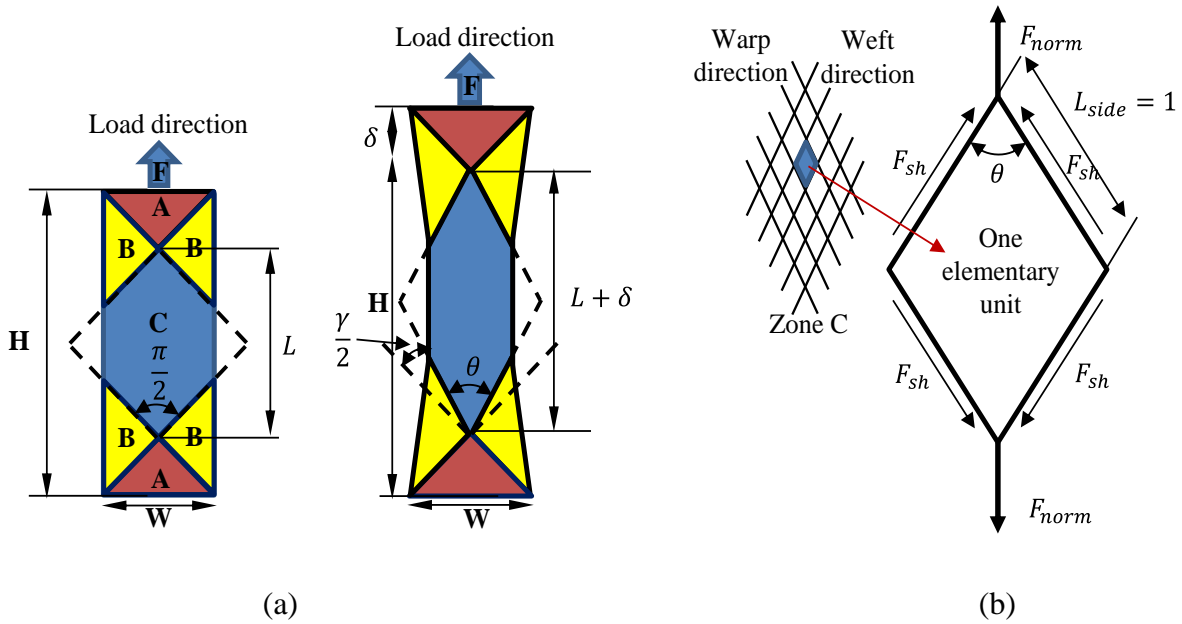


Figure 5.1 Schematic of bias extension test (a) and normalized load/shear load on a rhomboid with the unit side (b).

For the mechanical relation, the load measured on the tensile machine is a global quantity on the specimen in a bias-extension test. To compare the in-plane shear property obtained with different specimens or different devices, the overall load F needs to be transformed into a “normalized load” (F_{norm}), which is independent of the geometry of specimens[10]. In Fig.5.1b, a fabric rhomboid element with unit dimensions is defined as an elementary unit. As the fabric can be seen as a collection of a large number of elementary units, F_{norm} is equivalent to the value of the overall load F dispersed on each elementary unit. Based on the three assumptions, the shear angle in an elementary unit in zone C is thought to be uniform and equal to θ . Furthermore, the shear stress F_{sh} (Fig.5.1b) investigated in several other studies[10,12,13,26,27] is defined as the tangential load along the side of an elementary unit.

As a result, these shear stresses F_{sh} lead to a moment M_s [10,12,13] in an elementary unit, whose side length L_{side} is supposed to be 1:

$$M_s(\gamma) = F_{sh} L_{side} \cos \gamma \quad (2)$$

Then it is assumed that the total power generated by the overall load F is dissipated in these elementary units in zones B and C [10,12,13]:

$$F(\gamma) \cdot \dot{\delta} = M_s(\gamma) S_C \dot{\gamma} + M_s \left(\frac{\gamma}{2} \right) S_B \frac{\dot{\gamma}}{2} \quad (3)$$

where S_B , S_C are the initial areas of zone B and C; $M_s(\gamma) S_C \dot{\gamma}$ and $M_s \left(\frac{\gamma}{2} \right) S_B \frac{\dot{\gamma}}{2}$ are the power of shear in zone C and B.

According to the geometry of the specimen, M_s can be obtained as follows[12,13,26,27]:

$$M_s(\gamma) = \frac{F(\gamma)L}{W(2L-W)} \left(\cos \frac{\gamma}{2} - \sin \frac{\gamma}{2} \right) - \frac{W}{2L-W} M_s \left(\frac{\gamma}{2} \right) \quad (4)$$

Using equation (2), the shear stress can be obtained incrementally:

$$F_{sh}(\gamma) = \frac{F(\gamma)L}{W(2L-W) \cos \gamma} \left(\cos \frac{\gamma}{2} - \sin \frac{\gamma}{2} \right) - \frac{W \cos \frac{\gamma}{2}}{(2L-W) \cos \gamma} F_{sh} \left(\frac{\gamma}{2} \right) \quad (5)$$

5.2.3 Tufting process and test specimens

The tufting technique was developed in the industrial manufacturing procedure for carpet and warm garments. Recently, this technique has become a commercially available method for achieving the through-thickness reinforcement (TTR) in thermosetting polymer matrix composites [28]. As illustrated in Fig.5.2a, an additional yarn can be inserted into the multi-layered dry fabric through-the-thickness by a hollow needle. When the needle retracts, the inserted yarn remains inside the dry fabric or the underlying support (plastic/silicone foam or wooden board), due to the simple friction and form a loop on the opposite surface. The tufting

process presents one-side access property improving significantly the flexibility of application. As the tufting yarns don't generate any tension on the surface, the degradation to the in-plane properties of fabric can be effectively reduced.

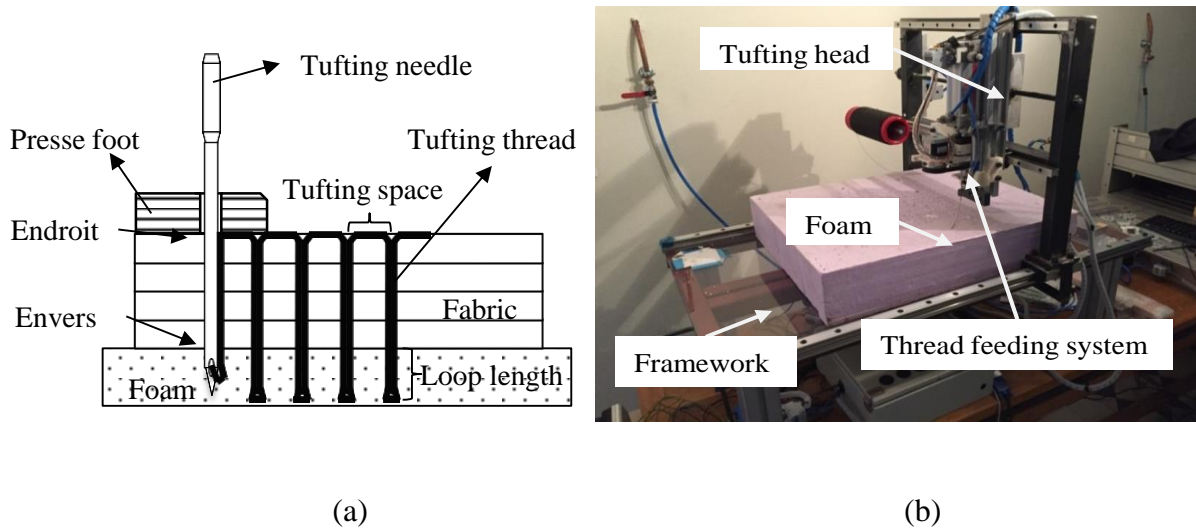


Figure 5.2 Schematic of tufting process (a) and automatic tufting device (b).

In this study, the experiment specimens were manufactured using a programmable tufting machine developed by the laboratory (Fig. 5.2b). The hollow needle is controlled by a pneumatic jack to realize the insertion and retraction movements. A presser foot is used to couple with the movement of tufting needle to provide an appropriate pressure around the tufting node. A reliable feeding system ensures the tufting yarn can be transferred immediately and smoothly. Several other parameters such as tufting density, tufting pattern and tufting position can be modified easily in the computer, according to the requirement.

As illustrated in Fig.5.3, the overall size of the test specimen is 270 mm in length and 70 mm in width. The testing speed for the bias extension tests is defined to 40 mm/min. The tufting yarn is inserted into the fabric with a tufting depth of 30 mm. The tufting zone is identical for every specimen and intentionally set to be $120 \times 60 \text{ mm}^2$, so as not only to cover the whole zone C in the centre but also to be divisible by different tufting space (5/10/15 mm).

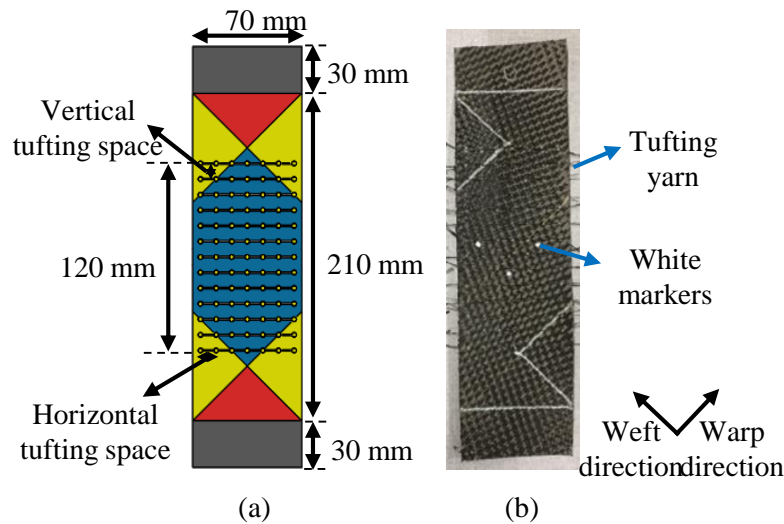
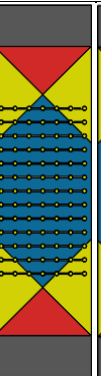
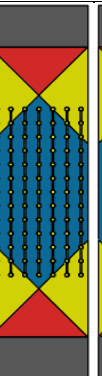
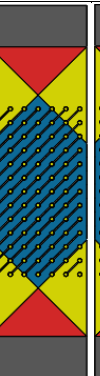
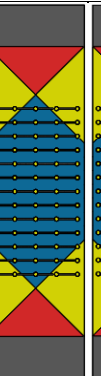
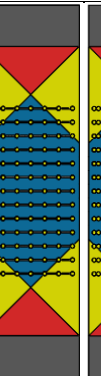
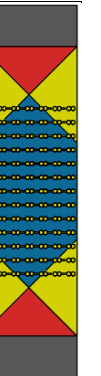


Figure 5.3 Schematic of the H10 tufted specimen (a) and image of the H10 tufted specimen (b).

The investigations of the influences of tufting directions in the plane, tufting density and the width of tufting yarn on the shear properties are executed by examining the overall applied load on the tensile machine. All the test specimens are shown schematically in Table 5.1. The abbreviation system used in this study is described as follows: NT1 denotes single-layered non-tufted specimen and NT2 is the two-layered non-tufted specimen; letters ‘H/V/D’ at the beginning of the abbreviations refer to Horizontal/Vertical/Diagonal tufting directions in the plane, respectively; the name starting with letter ‘TH’ represents that the specimen is composed of two-layered and tufted in the horizontal direction; Arabic number in the abbreviations of the tufted specimens represents the tufting space in the horizontal direction. The researches in this paper mainly focus on the tufted specimens with a single layer, to better understand and characterize the different mechanical behaviour generated by the inserted tufting yarn. V10/H10/D10/NT1 samples account for the investigations of tufting directions, H5/H10/H15/NT1 samples are used for the studies of tufting density and H10/H10D/NT1 samples are to explore the effect of tufting yarn width. The H10D with a horizontal tufting space of 10 mm and double-tufted in one elementary unit is chosen to compare with the specimen H10, which has the same tufting space but is single-tufted in one elementary unit.

The yarn double-tufted in one elementary unit is seen as a wider tufting yarn in comparison to the single-tufted one. Moreover, this effect of tufting yarn width (double-tufted in one elementary unit) has been further confirmed using a group of specimens containing two layers (TH10/TH10D/NT2). The standard deviations associated with the subsequent results for each type of specimen are given by three repeatability tests.

Table 5.1 Main properties of the test specimens.

Sample	NT1	NT2	H10	V10	D10	H5	H15	H10D	TH10	TH10D
Layer number	1	2	1	1	1	1	1	1	2	2
Horizontal tufting space	-	-	10	10	10	5	15	10	10	10
Vertical tufting space	-	-	10	10	10	10	10	10	10	10
The number of tufted elementary units	0	0	91	91	91	169	65	91	91	91
Tufting direction	-	-	0°	90°	45°	0°	0°	0°	0°	0°
Patterns										

5.2.4 Optical measurement based on cross-correlation algorithm

Previous studies [10,11,29] have demonstrated the theoretical value of the shear angle in bias-extension tests based on the PJN approach deviates from the actual shear angles when the shear deformation reaches a certain level. Thus, it is important to take accurate measurements for the actual shear angle during the bias-extension test in the pure shear zone (zone C). In the present study, a spot-detection method based on the Cpcorr function [30] (Tune control point

locations using cross-correlation) in MATLAB is proposed to tack the white dot markers on the fabric surface, regarded as the control points. With this algorithm, every two adjacent images can be selected out as a reference image and a moving image, from a series of consecutive images recorded by a digital camera. It permits the normalized cross-correlation to adjust each pair of control points specified in the two selected images. The coordinates of the adjusted control points in the moving image are returned and transformed for the following iterative process. The number of control points can be set flexibly according to the requirement and any featured fabric texture or artificial markers can be used as control points.

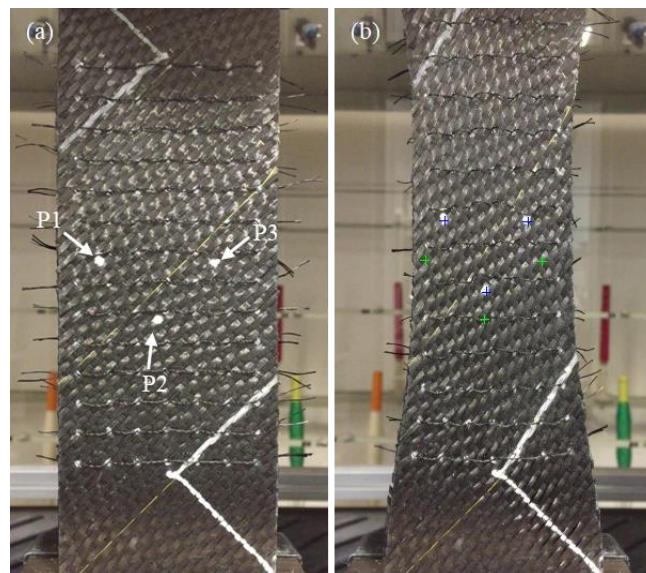


Figure 5.1 Un-deformed specimen (a) and deformed specimen (b).

Therefore, to realize the measurement of actual shear angle during the bias extension test, the movement of three white dot markers (P1, P2, P3) painted on the surface of the carbon fabric along the warp/weft tows in the pure shear zone are tracked, as illustrated in Fig. 5.4a. To increase the accuracy of measurement, the size of the marker should not be larger than the width of tow in the fabric and sufficient distance is necessary between the markers. During the program running, the blue crosses matching the current position of the control points are used to verify the correctness of the tracking process and the green crosses illustrate the initial position of these control points (Fig. 5.4b). Then, the actual shear angle (radian) can be

calculated based on the trigonometric function and the slopes of the linear equation established by control points:

$$\gamma = \frac{\pi}{2} - |\arctan(k1) - \arctan(k2)| \quad (6)$$

where γ is the actual shear angle; $k1$ refers to the slope of the linear equation determined by P1 and P2; $k2$ is the slope of the linear equation determined by P2 and P3.

The actual distance, d , between any two specified control points can be obtained by the following expression:

$$d = f \cdot \sqrt{(\Delta x)^2 + (\Delta y)^2} \quad (7)$$

where Δx and Δy represent the horizontal and vertical pixel differences of the two specified points in the image; f is the conversion ratio between actual distance and pixel difference.

5.3. Results and discussion

5.3.1 *The deformation mechanisms of the tufting yarns*

After the tufting process, the inserted tufting yarn stretches on the front surface of the fabric and forms a loop on the opposite side at each tufting node (Fig. 5.5a). The relative position of these tufting nodes will be changed owing to the extension of fabric during the tests. It is important to establish the links between the extension of fabric and the sliding of the tufting nodes, to further investigate the deformation mechanisms of the tufting yarns. For achieving this purpose, both theoretical analysis and optical measurements are applied to characterize the sliding behaviour of tufting nodes during the bias extension test. As illustrated in Fig. 5.5b, the black lines, referring to the warp and weft tows of fabric, rotate at the crossover points and become more aligned with the load direction during the fabric

extension. The coloured dots, representing the adjacent tufting nodes in different directions, can be classified into three groups by colours. Following the fabric extension, the sliding of tufting nodes in the vertical direction (a pair of blue dots) is positive, leading to an increased distance between the tufting nodes. On the contrary, the sliding of tufting nodes in the horizontal direction (a pair of green dots) is negative, equivalent to a decreased distance. In particular, considering the inextensible property of fabric tows and ignoring the tow slippage behaviour, the sliding of tufting nodes in the diagonal direction (a pair of red dots) can be neglected during the test.

In theoretical analysis, to quantify the sliding of tufting nodes along vertical (d_v) and horizontal (d_h) directions in zone C, two equations based on the theoretical shear angle γ obtained by Eq. (1) are established as follows:

$$d_v = 2 \cdot \frac{S_v}{\sqrt{2}} \cdot \cos\left(\frac{\theta}{2}\right) = \sqrt{2}S_v \cdot \cos\left(\frac{\pi}{4} - \frac{\gamma}{2}\right) = \frac{S_v(L+\delta)}{L} \quad (8)$$

$$d_h = 2 \cdot \frac{S_h}{\sqrt{2}} \cdot \sin\left(\frac{\theta}{2}\right) = \sqrt{2}S_h \cdot \sin\left(\frac{\pi}{4} - \frac{\gamma}{2}\right) = \sqrt{2}S_h \cdot \sin\left(\cos^{-1}\left(\frac{L+\delta}{\sqrt{2}L}\right)\right) \quad (9)$$

where, S_v and S_h (Fig.5.5b) correspond to tufting space in vertical and horizontal directions, respectively.

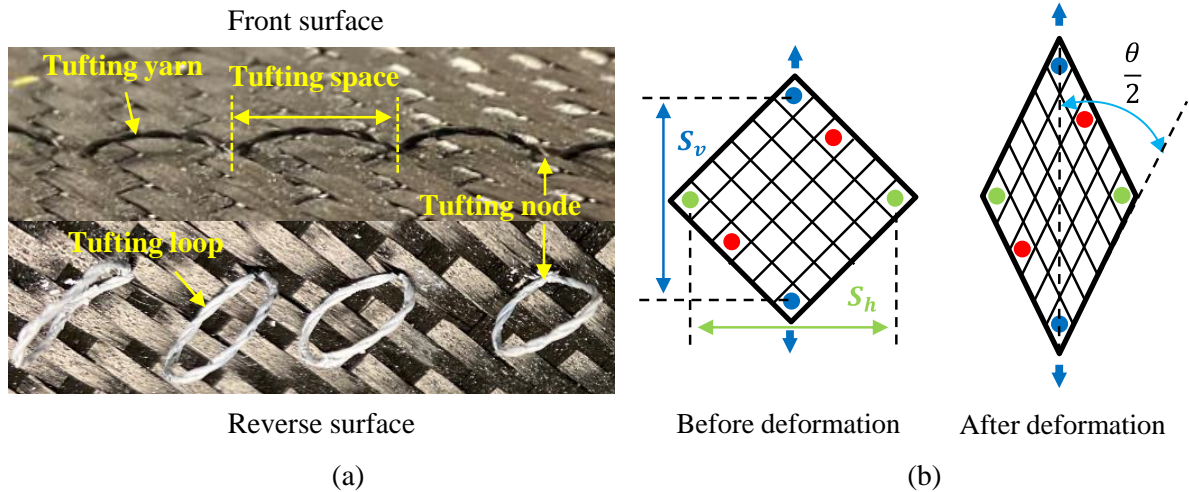


Figure 5.2 The two surfaces of a tufted specimen (a) and the influence of fabric deformation on the position of tufting nodes.

Then, the optical measurement presented previously employed to verify the theoretical equations. Several white markers are painted at the position of the tufting nodes for tracking the sliding of tufting nodes during the test. The comparison of the measured values (solid lines) and the theoretical ones (dash lines) obtained by Eqs. (8) and (9) against fabric extension has been shown in Fig.5.6a. For the fabric extension inferior to about 40 mm, the agreement between the theoretical and measured values in every direction is good. Over this limit, the measured values for the horizontal and vertical directions start to deviate from the theoretical ones. The measured results for the diagonal direction always seem to be invariant and to overlap with the theoretical values during the entire test. Furthermore, Fig. 5.6b shows the measured shear angles as a function of fabric extension. Measured values are compared with the theoretical ones obtained by Eq. (1) for an NT specimen. The theoretical shear angle, represented by the black dotted line, can reflect the real in-plane shear angle until the extension of fabric reaching a value of about 43 mm. Then, for further extension, the slippage of fabric tows occurs and the measured angles become smaller than the theoretical ones. As Eqs. (8) and (9) are derived from Eq.(1), the deviation of the theoretical shear angle eventually leads to the deviation of the theoretical sliding of tufting nodes in vertical and horizontal directions. The slight difference of critical values between the shear angle and sliding of tufting nodes (43 and 40 mm) suggests that the inserted tufting yarns can affect slightly the fabric shear deformation.

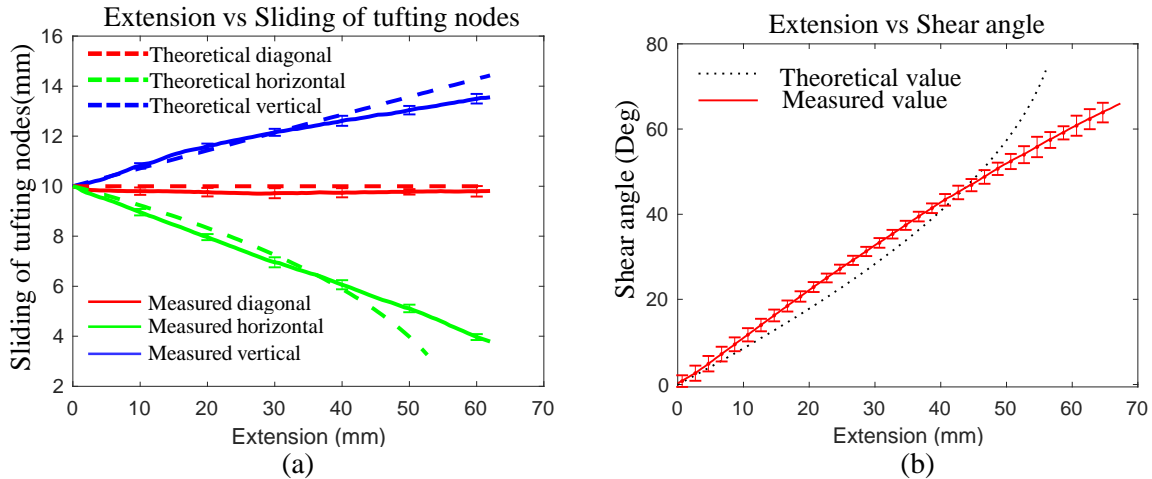


Figure 5.3 Theoretical/measured sliding of tufting nodes in different directions, theoretical values in vertical and horizontal directions are calculated by Eq.(8) and (9) (a); theoretical/measured shear angle for a non-tufted specimen, theoretical values are calculated by Eq.(1) (b) in a bias-extension test.

It has been proved that the sliding of tufting nodes will occur during the fabric extension. Considering the inextensible property of the inserted tufting yarns, the sliding of tufting yarn in the longitudinal direction of yarn leads to a pull-out effect. The tufting loops on the reverse side of the fabric should be pulled out at these tufting nodes to the front surface. To confirm this pull-out behaviour at the scale of tufting yarn, the tufting loops on the reverse side are intentionally dyed into white colour and the tufting yarns on the front side remain uncoloured (Fig. 5.5a). Once the white yarns are observed on the front surface, it suggests that the tufting yarns are pulled out. The length of the white yarns on the front surface can be used to quantify the homogeneity and severity of this pull-out behaviour.

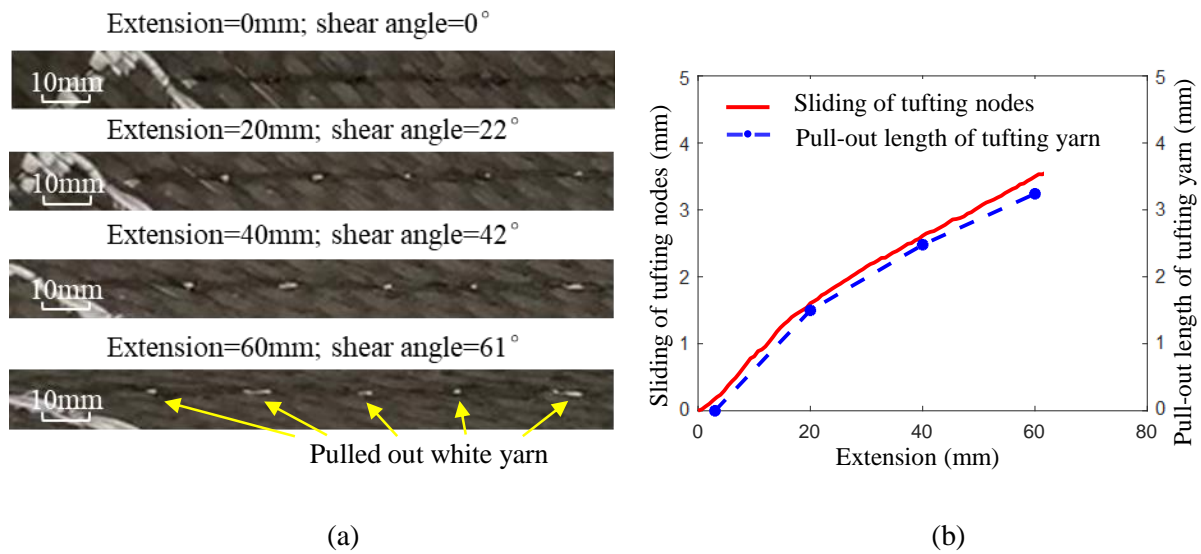
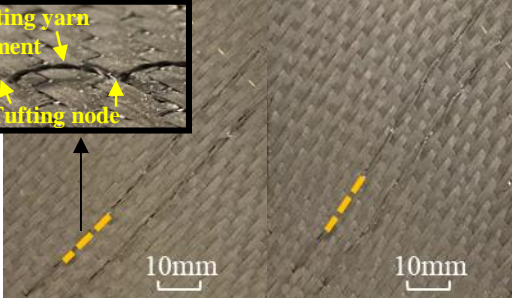


Figure 5.4 For vertical tufting, sliding behavior of tufting yarn at different fabric extension stages (a) and the comparison between the mean sliding distance of tufting yarn and the increase of tufting space (b).

As shown in Fig. 5.7a, it can be observed that the white yarns (pull-out tufting yarn) are increased along with the fabric extension, but their lengths at each tufting node are varying. The inhomogeneity of these pull-out lengths is anticipated owing to the different frictional resistance at each tufting node. As the tufting yarn can be inserted either between the fabric tows or just inside the middle of them, the unstable distributions result in different local yarn compactness and generate variant frictions. Furthermore, the pull-out length of tufting yarn is defined as the mean value of these white line lengths on the front surface, which are measured via ImageJ software at the fabric extension of 20/40/60 mm. Theoretically, the pull-out length of tufting yarn should be identical to the measured sliding of tufting nodes, as the tufting yarn is inextensible. However, as shown in Fig. 5.7b, it can be seen that the pull-out length of tufting yarn (blue dash line) is slightly smaller to the measured sliding of tufting nodes (red solid line). This global reduction is considered to be caused by the initial weak curvature of the tufting yarns stretching on the front surface (Fig. 5.5a) and the thickness of the fabric.

Table 5.2 Deformation behavior of tufting yarn at different fabric extension stages for horizontal and vertical tufting cases. State of tufting yarn at different fabric extension stages for horizontal and diagonal tufting cases. For horizontal tufting, the larger the fabric extension, the more curved the tufting yarns. For diagonal tufting, (the orange dash lines are used to mark one of the tufting yarn segments divided by tufting nodes) although this marked tufting yarn segment rotates following fabric extension, its length is always constant.

Extension (mm)	0	20	40	60
Shear angle (°)	0	22	42	61
H10 (Horizontal)				
D10 (Diagonal)				

In the case of horizontal tufting, an out-of-plane bending phenomenon identified as the buckles of tufting yarns can be observed, owing to the negative sliding of tufting nodes in the horizontal direction, as illustrated in Table 5.2. The larger the fabric extension, the more curved the tufting yarns. The initial straight tufting yarns prefer to be curved rather than to penetrate the fabric by overcoming the friction, as their bending stiffness is thought to be weaker. Furthermore, when the tufting yarns are inserted in the diagonal direction, the same approach used in the vertical tufting case, where the tufting loops on the reverse side are coloured to white, is applied to characterize the sliding behaviour. It has been noted that the tufting yarn on the front surface is discontinued and can be divided into many segments by the tufting nodes. The orange dash lines in Table 5.2 are used to mark one of these tufting yarn segments, so that the different positions of this marked tufting yarn segment at the different fabric extension stages is able to be observed. Although this tufting yarn segment rotates following the fabric extension, its length always keeps constant, suggesting that no sliding or bending at the scale of tufting yarn occurs. Consequently, it is thought that the diagonal

tufting approach is more suitable for eliminating the tufting defects compared to the other two tufting methods.

5.3.2 Influence of in-plane tufting directions on shear deformation

The influence of tufting direction on bias deformation has been illustrated in Fig.5.8a, as overall applied load (N) versus shear angle ($^{\circ}$) measured in the zone C of the specimens. Three tufted specimens (V10, H10, D10) with different in-plane tufting directions, coupled with identical tufting points (91) and tufting density (horizontal and vertical tufting spaces both are 10 mm), are compared to each other. A non-tufted specimen is used as a reference in this study. The error bars on the load curves represent standard deviation on either side of the average. It can be observed that at the early stage, the difference between the curves is quite insignificant and the increase rate for the magnitude of applied load is small. However, when the shear angle exceeds approximately 42° , the curves start to deviate and the increase rate becomes considerable. This critical shear angle corresponds to the so-called ‘locking angle’. It can be also noted that all the tufted specimens present a higher load resistance compared to the non-tufted fabric. The most prominent increase of the applied load can be observed in the case of vertical tufting (V10). In contrast, the curve of diagonal tufting (D10) has the lowest increase rate among the three tufted specimens but is very close to the horizontal tufting (H10). This is very clear when examining the applied load at 55° shear angle, which is regarded as the maximum shear angle value appearing in the deep-drawing process without severe forming defects (Fig.5.8b). The mean value of the applied loads for the V10, H10 and D10 specimens at 55° rises respectively by 41, 22 and 18 % in comparison with the NT fabric. However, as the difference in the applied load between the horizontal and diagonal tufting (about 1N) is inferior to the measurement deviations, the difference between these two tufting methods can be ignored.

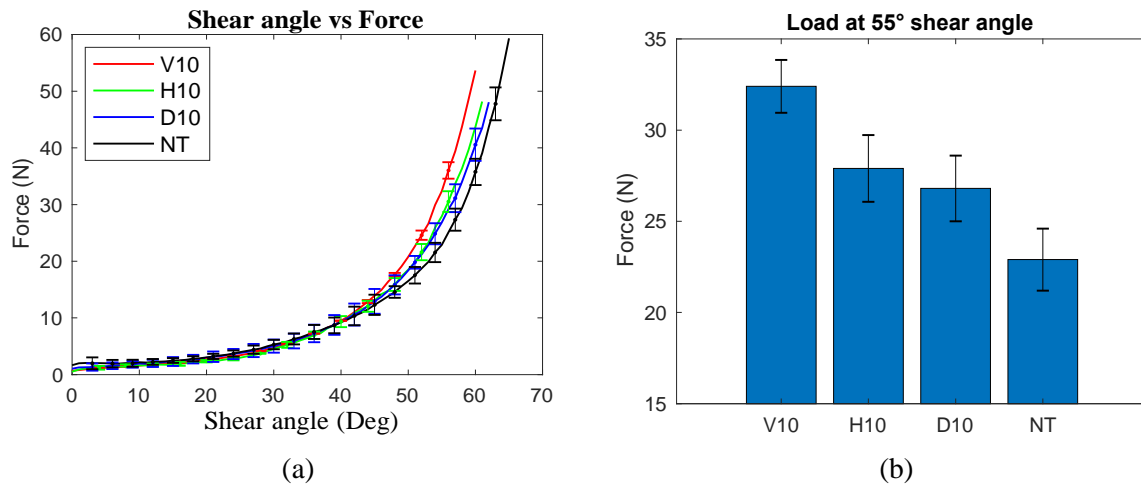


Figure 5.5 Shear load curves for different tufting directions (a) and the applied force measured at a shear angle 55° (b).

In the textile deformability study of Lomov et al.[31], the Digital Image Correlation (DIC) method has been carried out at the fabric tow level to reveal mechanisms during the bias-extension test. By observing the incremental displacements fields at the different stage of the shear load curve, it has been approved that the fabric tow is subjected to a rigid body motion (rotation + translation of the centre) at the early stage (before the ‘locking angle’), where the strain field within the tow is null or very weak. When the shear angle becomes large, especially exceeding the ‘locking angle’, the relative displacement is no longer a simple rotation field but added by a transverse compression field. The fabric tow cannot be regarded as a rigid body motion anymore, due to this compression strain. Similar conclusions have been described in some other studies[7,13,32]. These investigations also demonstrated that, for the early stage, the shear load is mainly caused by friction between the warp and weft tows. When the fabric shears to the ‘locking angle’, from which the geometry of weaving cannot rotate anymore, the fabric tows are subjected to side contacts with each other leading to a transverse compression and the shear load is then thought to be mainly caused by this transverse compression in the tows.

Thus, in the second stage, the local fabric compactness can be further modified due to the insertion of the tufting threads, which is regarded as an in-plane tufting effect. On the other

hand, the bending or sliding of tufting yarns discussed in Section 5.3.1 can be seen as an out-of-plane tufting effect. Both the in-plane and out-of-plane tufting effects account for the load variations between the different specimens.

Several main mechanical mechanisms for the three tufted specimens with different tufting directions are demonstrated schematically in Fig. 5.9. The bias tows of the tufted fabrics need to be more squeezed to achieve the same shear angle (after the ‘locking angle’) compared to the non-tufted fabric, since the tufting yarn is expected to occupy the space in the fabric considering its thickness and stiffness. No matter the tufts are just inserted between tows or pass through the middle of a tow, both cases can bring in a more compact local areal density surrounding the tufting nodes and generate a larger transverse compression, marked as green arrows in Fig. 5.9. As a result, the tufted specimens always need relatively higher loads for the shear deformation compared with the NT specimen, due to the in-plane tufting effect.

Furthermore, the diagonal tufting is considered to have the simplest mechanical mechanism among the three tufted specimens, due to the neglected sliding of tufting nodes during the shear deformation. No obvious deformation or sliding behaviour at the scale of tufting yarn can be observed in this case, so that the out-of-plane tufting effect is neglected, as shown in Fig. 5.9b. On the other hand, the horizontal tufting can generate bending stress (blue arrows in Fig. 5.9a) due to the bending behaviour of the tufting yarns on the front surface, to theoretically resist the contraction of fabric in the width direction to some extent. However, according to the experimental data (Fig. 5.8) and the theoretical bending stiffness of the tufting yarn, this bending stress can be almost ignored. In contrast, for the vertical tufting, an elongation between the tufting nodes leads to a slippage of the tufting yarns through the fabric, which can generate tensile stress (red arrows Fig. 5.9c) in the tufting yarns owing to the friction. This tension stress impedes the extension of the fabric in the length direction and results in a higher load resistance compared to the other two tufted specimens. As illustrated

in Section 5.3.1, the tufting yarn starts to slide almost from the beginning of the test. However, an obvious increase in the load resistance for vertical tufting can be noted only after the ‘locking angle’. It can be explained that the force of friction, caused by the contact between the tufting yarns and fabric tows, can be dramatically reinforced due to the supplementary compressive stress when the fabric tows are locked up.

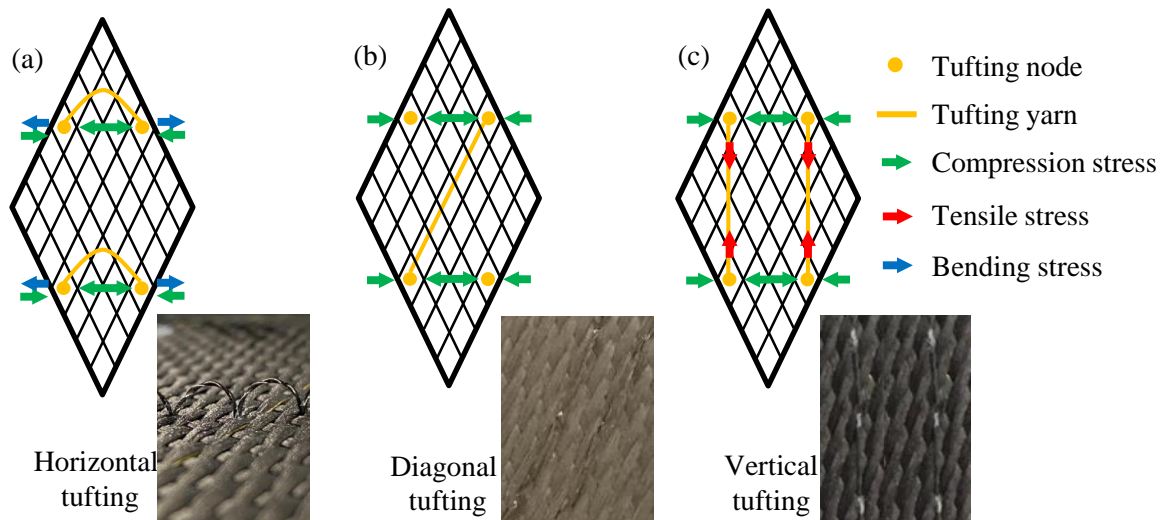


Figure 5.6 Schematic of mechanical mechanisms in tufted fabrics.

5.3.3 Influence of tufting density on shear deformation

Tufting density is another important parameter often studied for tufted fabrics. Fig. 5.10a shows the applied load versus shear angle curves for the three specimens with different horizontal tufting densities. These tufted specimens have the same tufting space in the vertical direction, but their horizontal tufting space is different and set to be 5/10/15 mm, namely H5/H10/H15 respectively. The curve for the non-tufted specimen is still used as a reference. Similarly, in the first stage, no apparent difference can be distinguished among these specimens. Then, after achieving the locking angle, the resistance to the applied load of the tufted specimens is seen to be increased with the tufting density, although the load curves for the H10 specimen are just a little higher than the H15 specimen. Specifically, the difference in the level of the applied load observed at a shear angle of 55° (Fig. 5.10b) confirms the

conclusion for the tufting density. Considering the tufting points per range, 7 for H10 and 5 for H15, the difference of the mean applied load between the H10 and H15 specimens at the 55° shear angle is only 0.5 N (approximately 2% difference), which cannot be distinguished effectively due to the measurement deviation and device accuracy. However, as the tufting points per range go up from 7 to 13, the applied force of H5 rises apparently by 15% of the H10 specimen. It suggests that only when the variation of the tufting points reaches a certain value, the difference in mechanical properties can be reflected out at a macro level. Again, the tufted specimens show a considerable increase in the load resistance compared to the NT specimen, due to the in-plane tufting effect.

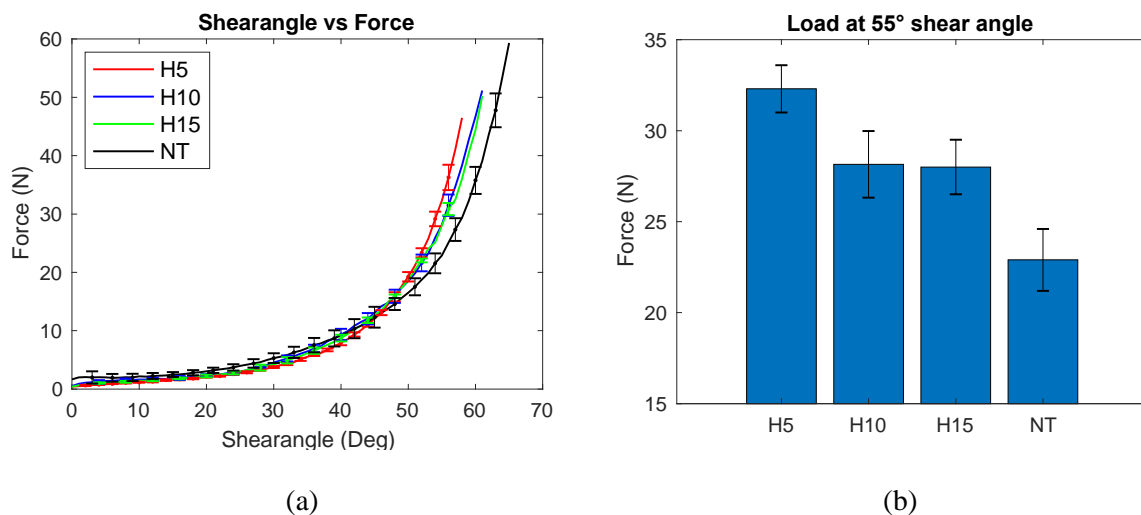


Figure 5.7 Shear load curves for different tufting densities (a) and the applied force measured at a shear angle 55° (b).

5.3.4 Influence of the tufting yarn's fineness on shear deformation

To investigate the effect of tufting yarn's width on the applied loads, a specific tufted specimen, namely H10D, is selected to compare with the H10 specimen. For the H10D specimen, tufting yarns are deliberately tufted two times very closely in an elementary unit cell, and then move horizontally 10 mm to the next elementary unit to repeat the double tufting process. This double-tufted structure bringing more tufting threads into one unit cell

and leading to higher local fabric compactness is considered to be equivalent to the case using a thicker tufting yarn. On the other hand, the H10 specimen maintains the single-tufted approach in each elementary unit. Therefore, the quantity of the tufted units in both cases is identically equal to 91. The comparison results are shown in Fig. 5.11a, it can be noticed that the curve of the H10D specimen rises much faster than the H10 specimen when it exceeds the 'locking angle'. At the shear angle of 55° (Fig. 5.11b), the mean value of the applied loads for H10D specimen demonstrates a considerable increase of 52% to the H10 specimen. This behaviour is anticipated due to the different in-plane tufting effect as the fabric towards the H10D specimen are more squeezed in the tufted elementary units.

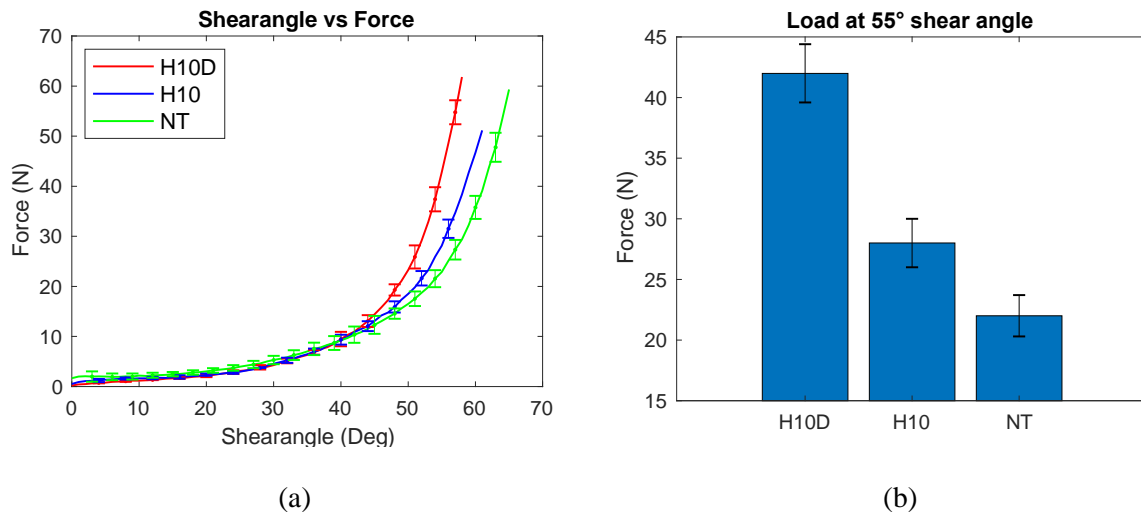


Figure 5.8 The comparison of overall applied loads between H10D and H10 specimens with a single layer (a) and the applied force measured at a shear angle 55° (b).

5.3.5 Comparison with the tufted two layers preforms

Since the tufting technique is generally used for binding multilayer fabrics, an additional set of two-layered specimens with identical layer orientations is tufted in the same way to verify the conclusion obtained in the one-layered cases concerning the effect of tufting yarn's width. The three two-layered specimens, namely TH10D, TH10 and NT2 respectively, are tested, as shown in Fig. 5.12a. Similarly, the double-tufted specimen TH10D has a higher load

resistance to the single-tufted specimen TH10. The non-tufted specimen still presents the lowest load resistance compared to the tufted ones. Fig. 5.12b illustrates that the double-tufted specimen has an increase in the magnitude of the applied load by 63% to the single-tufted specimen at a shear angle of 55° . On the other hand, the standard deviations of these two-layered specimens become much significant, as the interlayered friction can be easily affected by a slight layer misalignment. Regarding Figs. 5.11b and 5.12b, due to the existence of the interlayered friction, the mean load values of these two-layered specimens are always more than twice as large as the one-layered structures. Consequently, the experimental results, based on both the one-layered and two-layered tufted specimens, demonstrate that the tufting yarn's width can significantly influence the load resistance in the bias-extension test.

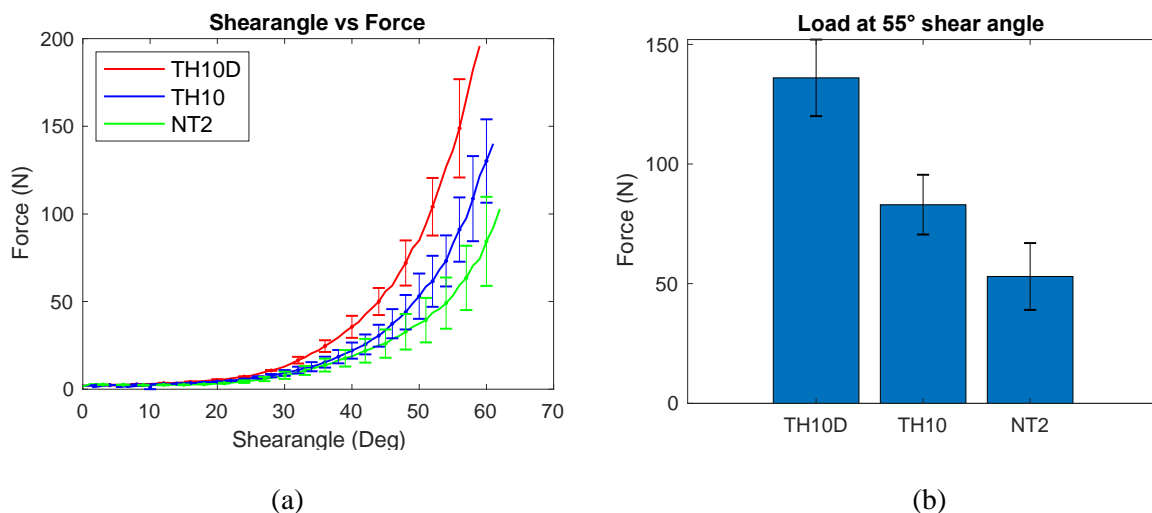


Figure 5.9 The comparison of overall applied loads between H10D and H10 specimens with two layers (a) and the applied force measured at a shear angle 55° (b).

5.3.6 Mechanical analysis of tufting effect on shear deformation

5.3.6.1 In-plane tufting effect

The in-plane mechanical behaviour of textile is thought to be a multi-scale problem. The overall work made by the clamping load is considered to be dissipated in the elementary units located in zones B and C. For a non-tufted fabric, when the fabric is extended to a certain

length, all the non-tufted elementary units in zone C are seen to have the same shear angles. For a tufted fabric, a new assumption based on a heterogeneous model consisting of tufted (yellow rhomboids) and non-tufted (blue rhomboids) elementary units is established as shown in Fig. 5.13a. In this assumption, when the tufted fabric is extended to a length of L_1 , the non-tufted elementary units in zone C are thought to present a shear angle γ_0 (Fig.5.13b). However, the shear angle of the tufted elementary units in zone C is supposed to be changed, as the in-plane tufting effect can increase the local areal compactness, the tows of the fabric in a tufted elementary unit are submitted to a higher deformation leading to this elementary unit having a larger shear angle γ_1 (Fig.5.13c) compared to the non-tufted case, under the hypothesis [31] that the tufting yarn is a rigid body and the tows of the fabric are not rigid any more after the ‘locking angle’ is reached. Furthermore, if the yarn is double-tufted, such elementary unit will present the highest shear angle γ_2 as shown in Fig.5.13d. Known that shear angle equal to $\frac{\pi}{2} - \theta$, it can be concluded that $\gamma_0 < \gamma_1 < \gamma_2$ due to $\theta_0 > \theta_1 > \theta_2$.

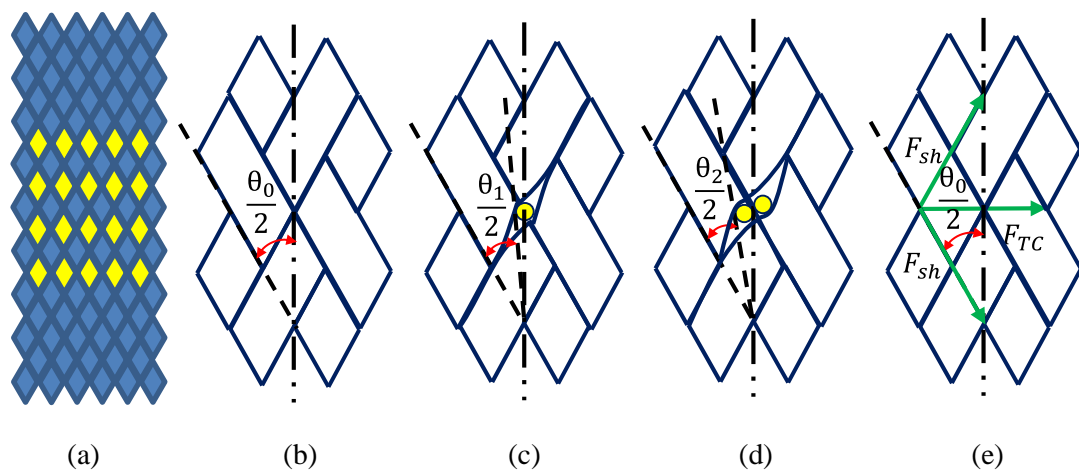


Figure 5.10 Schematic of a tufted fabric with an extension of L_1 is thought to be composed of non-tufted elementary units (blue rhomboids) and tufted elementary units (yellow rhomboids) (a); in this tufted fabric, the non-tufted elementary unit has a shear angle γ_0 (b); the single-tufted elementary unit has a shear angle γ_1 (c); the double-tufted elementary unit has a shear angle γ_2 (d); the horizontal projection of shear force in an elementary unit donates a compression (F_C) (e).

The consumed virtual work in non-tufted (W_{NTunit}), single-tufted (W_{STunit}) and double-tufted (W_{DTunit}) elementary unit is different and can be calculated as follows:

$$W_{NTunit} = M_s(\gamma_0)S_u\gamma_0 \quad (10)$$

$$W_{STunit} = M_s(\gamma_1)S_u\gamma_1 \quad (11)$$

$$W_{DTunit} = M_s(\gamma_2)S_u\gamma_2 \quad (12)$$

where S_u represents the initial area of one elementary unit; $M_s(\gamma_0)/M_s(\gamma_1)/M_s(\gamma_2)$ are the shear moments at the shear angle $\gamma_0/\gamma_1/\gamma_2$ respectively.

Several studies [31,33] have demonstrated that the shear moment M_s , presenting a non-linear increase following the shear angle γ , is low for small shear angles and high for large shear angles. Therefore, the shear angles $\gamma_0 < \gamma_1 < \gamma_2$ contribute to $M_s(\gamma_0) < M_s(\gamma_1) < M_s(\gamma_2)$.

Finally, the relation of virtual work consumed in different elementary units can be regarded as:

$$W_{NTunit} < W_{STunit} < W_{DTunit} \quad (13)$$

As the shear angle in zone B is half of the value in zone C, the elementary unit in zone B is impossible to achieve the ‘locking angle’, also proved by [31]. Thus, the tufted elementary unit in zone B can be seen as a non-tufted elementary unit, as its in-plane tufting effect can be neglected. Therefore, if only the in-plane tufting effect is taken into account, the power equations of the non-tufted fabric ($F(\gamma_0)_{NT} \cdot \delta$), single-tufted fabric ($F(\gamma_0)_{ST} \cdot \delta$) and double-tufted fabric ($F(\gamma_0)_{DT} \cdot \delta$) with an extension of L1 are shown as follows:

$$F(\gamma_0)_{NT} \cdot \dot{\delta} = M_s(\gamma_0)S_C\dot{\gamma}_0 + M_s\left(\frac{\gamma_0}{2}\right)S_B\frac{\dot{\gamma}_0}{2} \quad (14)$$

$$F(\gamma_0)_{ST} \cdot \dot{\delta} = M_s(\gamma_0)(S_C - S_T)\dot{\gamma}_0 + M_s\left(\frac{\gamma_0}{2}\right)S_B\frac{\dot{\gamma}_0}{2} + M_s(\gamma_1)S_T\dot{\gamma}_1 \quad (15)$$

$$F(\gamma_0)_{DT} \cdot \dot{\delta} = M_s(\gamma_0)(S_C - S_T)\dot{\gamma}_0 + M_s\left(\frac{\gamma_0}{2}\right)S_B\frac{\dot{\gamma}_0}{2} + M_s(\gamma_2)S_T\dot{\gamma}_2 \quad (16)$$

where S_T is the initial tufted areas in zone C.

5.3.6.2 Out-of-plane tufting effect

In Section 5.3.2, the sliding or the bending of tufting yarns regarded as the out-of-plane tufting effect can generate some extra efforts on the fabric during the bias-extension test.

For the vertical tufting, owing to the sliding of tufting yarns, more energy is required to overcome the work done by friction. The magnitude of friction caused by relative motions between tufting yarns and fabric tows is correlated to the coefficient of friction and the normal force. In this case, the normal force is thought to be a compressive force, which is caused by the projection of the shear force (F_{sh}) in the horizontal direction in a tufted elementary unit, as shown in Fig.5.13e. Based on Eq.(2), the normal force (F_{norm}) can be defined as:

$$F_{norm}(\gamma) = 2F_{sh}(\gamma) \sin\left(\frac{\theta}{2}\right) = 2 \frac{M_s(\gamma)}{\cos(\gamma)} \sin\left(\frac{\pi}{4} - \frac{\gamma}{2}\right) \quad (17)$$

According to the definition of kinetic friction, the frictional force (F_{fric}) caused by the sliding of tufting yarn can be calculated as:

$$F_{fric}(\gamma) = \mu_k \cdot F_{norm}(\gamma) = 2\mu_k \frac{M_s(\gamma)}{\cos(\gamma)} \sin\left(\frac{\pi}{4} - \frac{\gamma}{2}\right) \quad (18)$$

where μ_k is the coefficient of friction.

Then, the work consumed by frictions (W_F) at each tufting node equals to the product of the frictional force and the sliding distance:

$$W_F(\gamma) = d_s \cdot F_{fric}(\gamma) = 2d_s \mu_k \frac{M_s(\gamma)}{\cos(\gamma)} \sin\left(\frac{\pi}{4} - \frac{\gamma}{2}\right) \quad (19)$$

where d_s represents the sliding distance at each tufting node.

For the horizontal tufting case, the bending stress (Fig.5.9a) can be generated in the horizontal direction owing to the bending of tufting yarn. To simplify the model, the tufting yarn is thought to be a homogeneous beam under pure bending. The work consumed by bending of tufting yarn (W_B) is equivalent to the strain energy (U_B) stored in a curved tufting yarn[34].

$$W_B(\gamma) = U_B(\gamma) = \frac{M_B(\gamma)l}{2\rho(\gamma)} = \frac{M_B(\gamma)^2 l}{2EI} \quad (20)$$

where $M_B(\gamma)$ is the bending moment at a shear angle of γ ; l refers to the length of tufting yarn segment; $\rho(\gamma)$ represents the curvature radius of tufting yarn segment at a shear angle of γ ; E is the Young's modulus and I is the moment of inertia.

5.3.6.3 Mechanical analysis of different samples

The overall consumed energy of a test sample is thought to be a combination of the in-plane and out-of-plane tufting effects. For the group of samples with different tufting directions (as discussed in section 5.3.2), the same tufting density and yarn width lead to an identical in-plane tufting effect in these samples. However, the out-of-plane tufting effect is different, as more energy is needed due to the sliding and bending of tufting yarns in vertical and horizontal tufting cases respectively. Only in the diagonal tufting case, the out-of-plane tufting effect is ignored, as no apparent changes occur at the scale of tufting yarns during the fabric extension. Furthermore, as the shear angle in zone B cannot arrive at the “locking angle” and the number of tufting nodes in zone B is small, both the in-plane and out-of-plane tufting effects in zone B are not taken into account to simplify the mechanical equations. Finally, the power equations for the vertical tufting ($F(\gamma_0)_{V10} \cdot \dot{\delta}$), horizontal tufting ($F(\gamma_0)_{H10} \cdot \dot{\delta}$) and diagonal tufting ($F(\gamma_0)_{D10} \cdot \dot{\delta}$) at a fabric extension of $L1$ are shown as follows:

$$F(\gamma_0)_{V10} \cdot \dot{\delta} = M_s(\gamma_0)(S_C - S_{T10})\dot{\gamma}_0 + M_s\left(\frac{\gamma_0}{2}\right)S_B\frac{\dot{\gamma}_0}{2} + M_s(\gamma_1)S_{T10}\dot{\gamma}_1 + \frac{2n_{c10}d_s\mu_k M_s(\gamma_1)\sin\left(\frac{\pi}{4}\frac{\gamma_1}{2}\right)}{\cos(\gamma_1)} \quad (21)$$

$$F(\gamma_0)_{H10} \cdot \dot{\delta} = M_s(\gamma_0)(S_C - S_{T10})\dot{\gamma}_0 + M_s\left(\frac{\gamma_0}{2}\right)S_B\frac{\dot{\gamma}_0}{2} + M_s(\gamma_1)S_{T10}\dot{\gamma}_1 + \frac{n_{c10}M_B(\gamma_0)^2 l}{4EI} \quad (22)$$

$$F(\gamma_0)_{D10} \cdot \dot{\delta} = M_s(\gamma_0)(S_C - S_{T10})\dot{\gamma}_0 + M_s\left(\frac{\gamma_0}{2}\right)S_B\frac{\dot{\gamma}_0}{2} + M_s(\gamma_1)S_{T10}\dot{\gamma}_1 \quad (23)$$

where S_{T10} represents the initial tufted areas in zone C of a sample with a tufting space of 10 mm; n_{c10} refers to the number of tufting nodes located in zone C.

For the three samples with different tufting densities discussed in section 5.3.3, all the tufting yarns are subject to bending, owing to the horizontal tufting direction. The difference between these samples is the number of tufting nodes. Thus, the power equations for high tufting density ($F(\gamma_0)_{H05} \cdot \dot{\delta}$), middle tufting density ($F(\gamma_0)_{H10} \cdot \dot{\delta}$) has been shown in Eq. (22) and low tufting density ($F(\gamma_0)_{H15} \cdot \dot{\delta}$) samples at a fabric extension of L1 are shown as follows:

$$F(\gamma_0)_{H05} \cdot \dot{\delta} = M_s(\gamma_0)(S_C - S_{T05})\dot{\gamma}_0 + M_s\left(\frac{\gamma_0}{2}\right)S_B\frac{\dot{\gamma}_0}{2} + M_s(\gamma_1)S_{T05}\dot{\gamma}_1 + \frac{n_{c05}M_B(\gamma_0)^2l}{4EI} \quad (24)$$

$$F(\gamma_0)_{H15} \cdot \dot{\delta} = M_s(\gamma_0)(S_C - S_{T15})\dot{\gamma}_0 + M_s\left(\frac{\gamma_0}{2}\right)S_B\frac{\dot{\gamma}_0}{2} + M_s(\gamma_1)S_{T15}\dot{\gamma}_1 + \frac{n_{c15}M_B(\gamma_0)^2l}{4EI} \quad (25)$$

where S_{T05} and S_{T15} represent the initial tufted areas in zone C of a sample with a tufting space of 5 mm and 15mm respectively; known that $S_{T05} > S_{T10} > S_{T15}$; n_{c05} and n_{c15} refer to the number of tufting nodes located in zone C of a sample with a tufting space of 5 mm and 15mm respectively; known that $n_{c05} > n_{c10} > n_{c15}$.

In the investigation of tufting yarn width (section 5.3.4), the non-tufted, single-tufted and double-tufted samples are compared to each other. Again, due to the horizontal tufting direction, only the bending of tufting effect accounts for the out-of-plane tufting effect. The power equations for non-tufted ($F(\gamma_0)_{NT} \cdot \dot{\delta}$), single-tufted ($F(\gamma_0)_{H10} \cdot \dot{\delta}$) has been shown in Eq.22) and double-tufted ($F(\gamma_0)_{H10D} \cdot \dot{\delta}$) samples are illustrated as below:

$$F(\gamma_0)_{NT} \cdot \dot{\delta} = M_s(\gamma_0)S_C\dot{\gamma}_0 + M_s\left(\frac{\gamma_0}{2}\right)S_B\frac{\dot{\gamma}_0}{2} \quad (26)$$

$$F(\gamma_0)_{H10D} \cdot \dot{\delta} = M_s(\gamma_0)(S_C - S_{T10})\dot{\gamma}_0 + M_s\left(\frac{\gamma_0}{2}\right)S_B\frac{\dot{\gamma}_0}{2} + M_s(\gamma_2)S_{T10}\dot{\gamma}_2 + \frac{n_{c10}M_B(\gamma_0)^2l}{4EI} \quad (27)$$

5.4. Conclusion

The present study has shown that the deformation mechanisms at the scale of tufting yarn and the tufting effect on in-plane shear deformation during the bias-extension test. It is found that a higher shearing load is obtained when the fabric is tufted vertically (in the same

direction of the tensile displacement). The same phenomenon can be observed when a higher tufting density or a wider tufting yarn (double-tufted in one elementary unit) is used. Moreover, a bigger shearing load is considered to not only allow a reduction of the maximum shear angle in the fabric but also can degrade the fabric deformability. It hints that, in the case of the low curvature forming, the tufts can be applied at the highly deformable and predefined zones to reduce local fabric shearing or to transfer the shear forces into the un-sheared zones. In contrast, it may not be suitable for the high curvature forming, as the reduction of shear angle may further provoke the wrinkling defects in the highly deformable zones. Therefore, an appropriate choice and combination of these tufting parameters should be well considered prior to the tufting process for optimizing the forming process and the quality of the final products. Based on the experimental results and the mechanical analysis for different specimens, a database is collected and may be used for further investigations including an adaptable finite element simulation.

5.5. Reference

- [1] Wakeman MD, Rudd CD, Cain TA, Brooks R, Long AC. Compression moulding of glass and polypropylene composites for optimised macro-and micro-mechanical properties. 4: Technology demonstrator—a door cassette structure. *Compos Sci Technol* 2000;60:1901–18.
- [2] Trudel-Boucher D, Fisa B, Denault J, Gagnon P. Experimental investigation of stamp forming of unconsolidated commingled E-glass/polypropylene fabrics. *Compos Sci Technol* 2006;66:555–70.
- [3] Long AC. *Composites forming technologies*. Elsevier; 2014.
- [4] Wang Y, Chea MK, Belnoue JP-H, Kratz J, Ivanov DS, Hallett SR. Experimental characterisation of the in-plane shear behaviour of UD thermoset prepregs under processing conditions. *Compos Part A Appl Sci Manuf* 2020:105865.
- [5] Prodromou AG, Chen J. On the relationship between shear angle and wrinkling of textile composite preforms. *Compos Part A Appl Sci Manuf* 1997;28:491–503.
- [6] Skordos AA, Aceves CM, Sutcliffe MPF. A simplified rate dependent model of forming and wrinkling of pre-impregnated woven composites. *Compos Part A Appl Sci Manuf* 2007;38:1318–30.

- [7] Boisse P, Hamila N, Vidal-Sallé E, Dumont F. Simulation of wrinkling during textile composite reinforcement forming. Influence of tensile, in-plane shear and bending stiffnesses. *Compos Sci Technol* 2011;71:683–92. doi:10.1016/j.compscitech.2011.01.011.
- [8] Šimáček P, Advani SG. Desirable features in mold filling simulations for liquid composite molding processes. *Polym Compos* 2004;25:355–67. doi:10.1002/pc.20029.
- [9] Verleye B, Croce R, Griebel M, Klitz M, Lomov SV, Morren G, et al. Permeability of textile reinforcements: Simulation, influence of shear and validation. *Compos Sci Technol* 2008;68:2804–10.
- [10] Cartié DDR, Dell’Anno G, Poulin E, Partridge IK. 3D reinforcement of stiffener-to-skin T-joints by Z-pinning and tufting. *Eng Fract Mech* 2006;73:2532–40. doi:10.1016/j.engfracmech.2006.06.012.
- [11] Dell’Anno G, Cartié DD, Partridge IK, Rezai A. Exploring mechanical property balance in tufted carbon fabric/epoxy composites. *Compos Part A Appl Sci Manuf* 2007;38:2366–73.
- [12] Pasco C, Khan M, Kendall K. A novel discrete method of shear angle measurement for in-plane shear properties of thermoset prepreg using a point-tracking algorithm. *J Compos Mater* 2019;53:2001–13.
- [13] Cao J, Akkerman R, Boisse P, Chen J, Cheng HS, De Graaf EF, et al. Characterization of mechanical behavior of woven fabrics: experimental methods and benchmark results. *Compos Part A Appl Sci Manuf* 2008;39:1037–53.
- [14] Launay J, Hivet G, Duong A V, Boisse P. Experimental analysis of the influence of tensions on in plane shear behaviour of woven composite reinforcements. *Compos Sci Technol* 2008;68:506–15.
- [15] Lebrun G, Bureau MN, Denault J. Evaluation of bias-extension and picture-frame test methods for the measurement of intraply shear properties of PP/glass commingled fabrics. *Compos Struct* 2003;61:341–52.
- [1] Wakeman MD, Rudd CD, Cain TA, Brooks R, Long AC. Compression moulding of glass and polypropylene composites for optimised macro-and micro-mechanical properties. 4: Technology demonstrator—a door cassette structure. *Compos Sci Technol* 2000;60:1901–18.
- [2] Trudel-Boucher D, Fisa B, Denault J, Gagnon P. Experimental investigation of stamp forming of unconsolidated commingled E-glass/polypropylene fabrics. *Compos Sci Technol* 2006;66:555–70.
- [3] Long AC. *Composites forming technologies*. Elsevier; 2014.
- [4] Wang Y, Chea MK, Belnoue JP-H, Kratz J, Ivanov DS, Hallett SR. Experimental characterisation of the in-plane shear behaviour of UD thermoset prepreps under processing conditions. *Compos Part A Appl Sci Manuf* 2020:105865.
- [5] Prodromou AG, Chen J. On the relationship between shear angle and wrinkling of textile composite preforms. *Compos Part A Appl Sci Manuf* 1997;28:491–503.

- [6] Skordos AA, Aceves CM, Sutcliffe MPF. A simplified rate dependent model of forming and wrinkling of pre-impregnated woven composites. *Compos Part A Appl Sci Manuf* 2007;38:1318–30.
- [7] Boisse P, Hamila N, Vidal-Sallé E, Dumont F. Simulation of wrinkling during textile composite reinforcement forming. Influence of tensile, in-plane shear and bending stiffnesses. *Compos Sci Technol* 2011;71:683–92. doi:10.1016/j.compscitech.2011.01.011.
- [8] Šimáček P, Advani SG. Desirable features in mold filling simulations for liquid composite molding processes. *Polym Compos* 2004;25:355–67. doi:10.1002/pc.20029.
- [9] Verleye B, Croce R, Griebel M, Klitz M, Lomov SV, Morren G, et al. Permeability of textile reinforcements: Simulation, influence of shear and validation. *Compos Sci Technol* 2008;68:2804–10.
- [10] Boisse P, Hamila N, Guzman-Maldonado E, Madeo A, Hivet G, Dell’Isola F. The bias-extension test for the analysis of in-plane shear properties of textile composite reinforcements and prepregs: a review. *Int J Mater Form* 2017;10:473–92.
- [11] Pasco C, Khan M, Kendall K. A novel discrete method of shear angle measurement for in-plane shear properties of thermoset prepreg using a point-tracking algorithm. *J Compos Mater* 2019;53:2001–13.
- [12] Cao J, Akkerman R, Boisse P, Chen J, Cheng HS, De Graaf EF, et al. Characterization of mechanical behavior of woven fabrics: experimental methods and benchmark results. *Compos Part A Appl Sci Manuf* 2008;39:1037–53.
- [13] Launay J, Hivet G, Duong A V, Boisse P. Experimental analysis of the influence of tensions on in plane shear behaviour of woven composite reinforcements. *Compos Sci Technol* 2008;68:506–15.
- [14] Lebrun G, Bureau MN, Denault J. Evaluation of bias-extension and picture-frame test methods for the measurement of intraply shear properties of PP/glass commingled fabrics. *Compos Struct* 2003;61:341–52.
- [15] Wang J, Page JR, Paton R. Experimental investigation of the draping properties of reinforcement fabrics. *Compos Sci Technol* 1998;58:229–37.
- [16] Pérès P, Desmars B, Léard JP. Composite behavior of assemblies with AEROTISS® 03S technology. 16th Int. Conf. Compos. Mater., 2007.
- [17] Sickinger C, Herrmann A. Structural stitching as a method to design high-performance composites in future. *Proc. TechTextil Symp.*, vol. 2001, 2001.
- [18] Cartié DDR, Dell’Anno G, Poulin E, Partridge IK. 3D reinforcement of stiffener-to-skin T-joints by Z-pinning and tufting. *Eng Fract Mech* 2006;73:2532–40. doi:10.1016/j.engfracmech.2006.06.012.
- [19] Wittig J. Recent development in the robotic stitching technology for textile structural composites. *Int. Sampe Tech. Conf.*, vol. 33, 2001, p. 540–50.

- [20] Gnaba I, Legrand X, Wang P, Soulat D. Literature review of tufted reinforcement for composite structures. *IOP Conf Ser Mater Sci Eng* 2017;254. doi:10.1088/1757-899X/254/4/042011.
- [21] Liu LS, Zhang T, Wang P, Legrand X, Soulat D. Influence of the tufting yarns on formability of tufted 3-Dimensional composite reinforcement. *Compos Part A Appl Sci Manuf* 2015;78:403–11. doi:10.1016/j.compositesa.2015.07.014.
- [22] Shen H, Wang P, Legrand X, Liu L, Soulat D. Influence of the tufting pattern on the formability of tufted multi-layered preforms. *Compos Struct* 2019;228:111356.
- [23] Shen H, Wang P, Legrand X, Liu L. Characterisation and optimisation of wrinkling during the forming of tufted three-dimensional composite preforms 2019.
- [24] Dell'Anno G, Cartié DD, Partridge IK, Rezai A. Exploring mechanical property balance in tufted carbon fabric/epoxy composites. *Compos Part A Appl Sci Manuf* 2007;38:2366–73. doi:10.1016/j.compositesa.2007.06.004.
- [25] Molnar P, Ogale A, Lahr R, Mitschang P. Influence of drapability by using stitching technology to reduce fabric deformation and shear during thermoforming. *Compos Sci Technol* 2007;67:3386–93.
- [26] Harrison P, Clifford MJ, Long AC. Shear characterisation of viscous woven textile composites: a comparison between picture frame and bias extension experiments. *Compos Sci Technol* 2004;64:1453–65.
- [27] Harrison P, Wiggers J, Long AC. Normalization of shear test data for rate-independent compressible fabrics. *J Compos Mater* 2008;42:2315–44.
- [28] Dell'Anno G, Cartié DD, Partridge IK, Rezai A. Exploring mechanical property balance in tufted carbon fabric/epoxy composites. *Compos Part A Appl Sci Manuf* 2007;38:2366–73.
- [29] Lee W, Padvoiskis J, Cao J, de Luycker E, Boisse P, Morestin F, et al. Bias-extension of woven composite fabrics. *Int J Mater Form* 2008;1:895–8.
- [30] CPCORR n.d.
https://www.mathworks.com/help/images/ref/cpcorr.html?s_tid=srchtitle.
- [31] Lomov S V, Boisse P, Deluycker E, Morestin F, Vanclooster K, Vandepitte D, et al. Full-field strain measurements in textile deformability studies. *Compos Part A Appl Sci Manuf* 2008;39:1232–44.
- [32] Zouari B, Daniel J-L, Boisse P. A woven reinforcement forming simulation method. Influence of the shear stiffness. *Comput Struct* 2006;84:351–63.
- [33] Boisse P, Hamila N, Vidal-Sallé E, Dumont F. Simulation of wrinkling during textile composite reinforcement forming. Influence of tensile, in-plane shear and bending stiffnesses. *Compos Sci Technol* 2011;71:683–92. doi:10.1016/j.compscitech.2011.01.011.
- [34] Energy ES. 8.2 Elastic Strain Energy n.d.:242–55.

General conclusion

The investigations concerning forming behaviour of textile composite materials to optimize their final part quality are the fundamental subjects in this thesis, as the forming process is generally an unavoidable step in the manufacture of both thermoset and thermoplastic composite parts with complex shapes. The characterization of forming defects, the knowledge of deformation mechanisms and the understanding of processing parameters are mainly focused. The current studies on these aspects permit to find the most suitable forming conditions for the textile reinforcements to minimize the composite manufacturing defects. Although many researches have been done on the forming behaviours of textile composites, the various structures of composite materials lead to a large amount of works needed to be done. In this thesis, the thermoplastic composites with commingled yarns are attempted to be investigated, so that at first an experimental thermoforming machine is designed and developed with desired processing parameters. On the other hand, at the dry fabric scale, the forming behaviours of tufted multi-layered reinforcements, regarded as an advanced composite structure, are presented in details.

Temperature and pressure are considered to be the important parameters in thermoforming process, as they can significantly influence the formability behaviours. Therefore, in the conception of the experimental thermoforming machine, the preheating temperature, transferring velocity, blank-holder pressure and punch pressure need to be taken into account. The cooperation between three independent systems, i.e. the heating, transferring and forming system, realizes the complete thermoforming process. The punches with different shapes have been fabricated to investigate the forming behaviours with different deformations.

Tufting, as a relatively novel technology, is recently used in reinforcing the multi-layered composites through-the-thickness. In present research work, the influences of tufting density, tufting pattern and tufting location on the formability behaviours are mainly discussed. By the characterization of material draw-in, inter-layer sliding, wrinkling and out-of-plane buckling

phenomenon through the optical or numerical methods, it can be concluded that the presence of tufting threads can obviously modify the forming behaviours and forming defects. A high tufting density contributes to a small material draw-in and interlayer sliding. At the same time, the decreasing of tufting space can weaken the wrinkling and out-of-plane buckling phenomenon. The consistency study between tufting pattern and punch shape demonstrates that there is no necessity to use similar tufting pattern to the punch shape when only the wrinkling is under consideration. However, the tufting pattern still has some effects in the elimination of the out-of-plane buckling phenomenon, as the circle spiral pattern can introduce significant buckles at the scale of tufting yarns in the square-box forming case. Furthermore, based on the numerical analysis of the wrinkling phenomenon, it has found that the wrinkling distribution and amplitude are critically dependent on the tufting location in the zone underlying the blank-holders. By a good choice of tufting location/pattern, the wrinkles appearing in the central useful zone also can be weakened, but not able to be eliminated completely.

In addition, as the in-plane shear property is one of the most important mechanical properties during the forming process, it has been characterized via bias-extension test to reveal the influence of inserted tufting yarn in this thesis. It has been illustrated that the in-plane shear stress can be modified by the tufting density, tufting direction and the fineness of tufting yarn. As the high in-plane shear stress can reduce the maximum shear angle in the fabric, the resin infusion quality may be enhanced by increasing the overall homogeneity of the yarn network. On the other hand, the decrease of maximum shear angle can also introduce wrinkling phenomenon in some high deformed areas. Therefore, the experimental results hints that the tufting parameters including the density, direction and yarn fineness should be well considered in the design of tufted composites.

Perspective

At last, for the future work, the experimental thermoforming machine still needs to be modified and tested to ensure its stability during the operations. Relying on this machine, the forming behaviours of the thermoplastic composites with commingled yarns, as one of the main research directions, will be able to be investigated. Moreover, for the tufted composite structure, although the effects of some basic tufting parameters, such as tufting density, tufting pattern, tufting direction and so on, on the formability behaviours have been studied in this thesis, the research work concerning the tufting technique is still not enough. A further optimization of tufting pattern and the influence of some other tufting parameters (tufting deepness, tufting angle, the type of tufting yarn...) on the forming behaviours need to be carried out in the future. In this paper, a new numerical method is applied to characterize the wrinkling by a distance calculation from the target model to the reference model. However, the wrinkling indicators based on this technique still have many limitations; especially some of them lack a statistical analysis. More efforts are required in the development of the characterization of the wrinkling phenomenon.

Abstract

Forming process plays an important role in both Liquid composite moulding (LCM) and thermoforming methods to fabricate the advanced textile composite parts. The deformation of the fabric is complex and hard to be controlled during the forming, leading to the undesired defects. Once the forming defects are generated, it is difficult to be removed in the subsequent manufacturing steps and consequently remains in the final composite part. In order to improve the quality of the textile composites, whether they are thermoset or thermoplastic, the study of forming process is unavoidable. Therefore, the work in this thesis can be divided briefly into two aspects. An experimental thermoforming machine is designed and assembled to account for the investigations of forming behaviours of thermoplastic composites. On the other hand, the influences of various tufting parameters on the forming behaviours and forming defects have been deeply studied at the dry fabric scale, which is considered to be the first step in the LCM process. Furthermore, the in-plane shear property of tufted reinforcements is determined and estimated based on the bias-extension test. Based on these studies concerning the tufting technique, some suggestions have been given to optimize the manufacturing process for the tufted composite parts.

Résumé

Le processus de formage joue un rôle important dans les méthodes de LCM (Liquid composite moulding) et de thermoformage pour fabriquer les pièces composites avec hautes performances. La déformation du tissu est complexe et difficile à contrôler lors du formage, conduisant à des défauts indésirables. Une fois les défauts de formage sont générés, ils sont difficile de les éliminer dans les suivantes étapes de fabrication et par conséquent restent dans la pièce composite finale. Afin d'améliorer la qualité des composites textiles, qu'ils soient thermodurcissables ou thermoplastiques, l'étude du processus de formage est incontournable. Donc, le travail de cette thèse peut être divisé brièvement en deux aspects. Une machine de thermoformage expérimentale est conçue et assemblée pour les recherches relatives aux comportements de formage des composites thermoplastiques. D'autre part, les influences de divers paramètres de piquages sur les comportements de formage et les défauts de formage ont été étudiées en profondeur à l'échelle du tissu sec, qui est considéré comme la première étape du processus LCM. En outre, la propriété de cisaillement des renforts des piquages est déterminée et estimée sur la base du test de cisaillement. En fonction des investigations concernant la technique du piquage, quelques suggestions ont été faites pour optimiser le processus de fabrication des pièces composites des piquages.